

# Thesis

Design and Testing of a Low-Budget 2-in-1 Star Tracker and Sun Sensor for CubeSats

Master Thesis Aerospace Engineering

C. Handgraaf



# Thesis

## Design and Testing of a Low-Budget 2-in-1 Star Tracker and Sun Sensor for CubeSats

by

C. Handgraaf

to obtain the degree of Master of Science

at the Delft University of Technology,

to be defended publicly on Tuesday January 28, 2025 at 9:00 AM.

Student number: 4794214  
Project duration: April 22, 2024 – January 28, 2025  
Thesis committee: Dr. ir. J. Bouwmeester, TU Delft, supervisor  
Dr. S. Speretta, TU Delft, chair  
Dr.ir. E. van Kampen, TU Delft, examiner

Cover: <https://www.arducam.com/product/mini-ov9281-mono-global-shutter-for-pi/>  
Style: TU Delft Report Style, with modifications

# Preface

*Not every thesis ends up working as intended. Especially not when one designs an experimental satellite component from start to finish. But when I began investigating the possibilities for a more versatile attitude sensor, I could not foresee that we would end up creating a 2-in-1 attitude sensor that en passant is one of the world's smallest star trackers. Throughout the thesis, I gradually started to believe more and more in the project as the test results came in.*

*Seeing the first stars appear in the sensor's images and the algorithm correctly finding the coordinates was a magical moment. We, that being my supervisor Jasper Bouwmeester and I, were initially sceptical regarding the ability of a commercial-off-the-shelves Raspberry Pi camera to pick up faint stars. Had this not worked, the rest of the thesis would have been spent looking for different CMOS modules and theorising about what could be possible. But from that moment, I knew that the concept might actually work in practice and I happily spent the next months refreshing weather websites for a break in the clouds, so that I could test the sensor at night in freezing temperatures.*

*I would like to thank Jasper Bouwmeester for his knowledge, insight and feedback throughout the thesis. For every question I asked, you returned ten points I should address, which I frantically, but happily, tried to solve before our next meeting. Special thanks to Fabien Schmutz for letting me use the Optics Lab at AE. I think we exchanged around a hundred emails about lab equipment and lab availability. Then, a special thanks to the volunteers at Sterrenwacht Copernicus, for letting me use your site to perform the star tracker tests and for letting me see the rings of Saturn through your telescope. My roommates, for listening patiently to my daily thesis updates. And to Cas, for inspiring me to become an engineer.*

*At last, I would like to thank my parents and sister. Mom, thank you for always being available for a chat, a hug and for bringing a smile to my face every time I see you. Dad, thank you for all your questions and interest you showed in my thesis, and for helping me during testing and pushing me to continue testing despite my freezing toes. And thank you, Sis, for your daily updates on our bunny and giving me moments of rest during the last seven months.*

*C. Handgraaf  
Delft, January 2025*

# Summary

With satellites becoming smaller and smaller, their attitude sensors also need to scale down accordingly. Their technical budgets, most notably size and power consumption, need to be reduced, but a combination of several sensors is required for 3-axis attitude determination. The availability of these sensors is mostly dependent on the lighting conditions and slew rate of the spacecraft, which causes sensors to be under-utilised. Without significantly increasing the versatility of attitude sensors or reducing the number of sensors required for a mission, development of small satellites will slow down.

This thesis explored different approaches to increasing the versatility of attitude sensors, while lowering technical budgets and maintaining performance. It was chosen to pursue the development of a prototype 2-in-1 star tracker and Sun sensor using the same CMOS optical module, as this would allow for a sensor capable of operating in both sunlight and eclipse conditions, while offering high performance when stable and medium performance when tumbling. The number of sensors that need to be installed on a spacecraft can be significantly reduced. A set of requirements were generated for a flight-ready sensor and a prototype. These requirements were chosen in a way to make the accuracy and technical budgets competitive in relation to a combination of currently available commercial-off-the-shelves attitude sensors. The prototype aimed for a star tracker 1-sigma accuracy of  $2.0^\circ$  and a Sun sensor 1-sigma accuracy of  $5.0^\circ$ .

A suitable CMOS chip was searched among COTS optical modules compatible with Raspberry Pi or Arduino. The OV9281 from Arducam was considered to be the best candidate. This is a monochrome,  $1280 \times 800$  resolution camera module with a fixed FOV of  $89.5^\circ$  and total module size of  $25 \times 24 \times 6$  [mm]. Its power consumption is 156 [mW] when operating at 120 [Hz]. It has a small aperture, which reduces the risk of burn-in by sunlight, but decreases the ability to see faint stars. In the design phase, it was estimated how many stars the sensor could see, what the effects of stray light will be and which sensor modes should be selected to reduce the power consumption. Using a Raspberry Pi and Python, a script was created that controls the sensor during operation in both sensor modes.

The sensor modes were tested for both functionality and performance. The star tracker was tested by pointing it to the night sky at an observatory in the Netherlands. Here, it was determined which sensor settings would yield the highest success rate for determining the coordinates of the images and at which update rate this was done. Once this setting was found, an accuracy test was performed, where the accuracy of the star tracker mode was determined. For the Sun sensor mode a test setup in a lab was created where the Sun was simulated using a bright LED and a lens. First, it was investigated whether the sensor could successfully determine the Sun vector at the desired update frequency. Then, the accuracy across the FOV of the sensor was investigated.

The results of the tests show that the combined sensor has a 1-sigma accuracy of  $0.051^\circ$  with a margin of error of  $0.025^\circ$  in the star tracker mode. For the Sun sensor mode, the 1-sigma accuracy was determined to be better than  $3.0^\circ$  with a margin of error of  $0.1^\circ$ . The star tracker accuracy is comparable to that of the smallest available COTS star trackers, such as the CubeSpace CubeStar ( $0.02^\circ$ ). The Sun sensor accuracy of the prototype is an order of magnitude worse than its COTS competitors. The CMOS chip alone consumed 70 [mW], excluding the power required for analysing the images. While this might be an improvement over other attitude sensors, the power consumption is higher than what was targeted for a competitive sensor design and the update rate of the star tracker mode was insufficient. It is unlikely that a redesign of the optical module and the inclusion of a dedicated microcontroller will reduce the power consumption to below 70 [mW], without selecting a different CMOS chip and making use of improvements in microcontroller technology. However, the sensor might benefit from performing image analysis by a central computing unit on a satellite, if available.

Several areas of this thesis can be improved. Better sensor algorithms can improve the accuracy and update rate of the sensor modes. The test setup and conditions were not ideal, as light pollution played a negative

role in the star tracker tests and the Sun was not properly simulated for the Sun sensor tests. Then, the sensor has not been tested for the risk of burn-in when directly exposed to the Sun, and neither has it been tested for vacuum and radiation.

To conclude, this thesis has shown that potentially a 2-in-1 star tracker and Sun sensor can be created that use the same CMOS chip, while achieving performance between that of a star tracker and Sun sensor for reduced technical budgets compared to COTS attitude sensors. This new sensor has a higher availability, can be used for stable pointing and tumbling and takes up less volume on a satellite. For the design to outperform existing sensors, the solving times and power consumption need to be decreased. This can be done through reducing the computational load of the algorithms and manufacturing a dedicated microcontroller. Alternatively, a different CMOS chip or using a satellite's central computing unit needs to be considered.

# Contents

<b>Preface</b>	<b>i</b>
<b>Summary</b>	<b>ii</b>
<b>Nomenclature</b>	<b>viii</b>
<b>1 Introduction</b>	<b>1</b>
<b>2 Problem Investigation</b>	<b>2</b>
2.1 Need for a versatile optical sensor . . . . .	2
2.2 Sun sensor technology . . . . .	3
2.3 Star tracker technology . . . . .	10
2.4 Attitude determination techniques . . . . .	13
2.5 Knowledge gap . . . . .	14
2.6 Potential research areas . . . . .	16
<b>3 Research Plan</b>	<b>18</b>
3.1 Research question and hypothesis . . . . .	18
3.2 Methodology . . . . .	19
3.3 Anticipated challenges . . . . .	20
3.4 Planning . . . . .	20
<b>4 Preliminary Design Phase</b>	<b>22</b>
4.1 Design concept . . . . .	22
4.2 Requirements . . . . .	23
4.3 CMOS sensor selection . . . . .	27
4.4 Preliminary design . . . . .	31
<b>5 Detailed Prototype Design</b>	<b>39</b>
5.1 Baffle design . . . . .	39
5.2 Sensor operational modes . . . . .	40
5.3 Star tracker algorithm . . . . .	41
5.4 Sun sensor algorithm . . . . .	43
<b>6 Testing</b>	<b>46</b>
6.1 Experimental setup . . . . .	46
6.2 Results . . . . .	54
<b>7 Discussion</b>	<b>62</b>
7.1 Discussion of results . . . . .	62
7.2 Discussion of methodology . . . . .	64
7.3 Unexplored areas . . . . .	64
<b>8 Conclusion</b>	<b>66</b>
<b>References</b>	<b>67</b>
<b>A Gantt chart</b>	<b>70</b>
<b>B Test plans</b>	<b>71</b>
<b>C Sensor Code</b>	<b>77</b>

# List of Figures

2.1	A schematic overview of the mask and CMOS surface. Where the light ray falls on the CMOS is dependent on the angle of the Sun to the mask [12]. . . . .	3
2.2	Three different sun sensor types: a) collimating sensor, b) Sun-pointing sensor and c) tilted-mount sensor [15]. . . . .	4
2.3	Three-dimensional and contour plot of the resolution of the CMOS sensor from Antonello et al. [12]. . . . .	5
2.4	A schematic cross-section of a star tracker [24]. . . . .	11
2.5	Solar irradiance curve for both direct sunlight and albedo [15]. . . . .	16
3.1	A road map of the different design phases in this thesis. . . . .	19
4.1	Placement and viewing angles of three combined sensors on a 3U CubeSat. . . . .	23
4.2	Technical drawing of a 1U CubeSat with details on the rail system [32]. . . . .	25
4.3	The three best scoring optical modules from the trade off. . . . .	31
4.4	A 3D model of the OV9281's lens, active pixel sensor and outer structure. . . . .	34
4.5	Cross-section of the OV9281, including the angles for FOV ( $\theta$ ) and stray light ( $\zeta$ ). . . . .	34
4.6	Schematic view of an extended baffle with an height $v$ and a width $x$ . The lens of the optical module is given with the curved dotted lines. . . . .	35
4.7	Impact of different baffle lengths on stray light angle. The dotted line is the maximum allowed baffle length. . . . .	36
4.8	Power consumption of sensor against frame rate and different capture settings. . . . .	38
5.1	3D model of the 4 [mm] baffle created for the OV9281 sensor module. . . . .	40
5.2	The baffle placed over the OV9281 sensor module. Imperfections are visible on the top edge and inside the cone. . . . .	40
5.3	Schematic view of the prototype star tracker mode activity flow used in testing. . . . .	41
5.4	An example geometric hash code from stars A, B, C and D. The coordinates of these stars form the has code $(x_C, y_C, x_D, y_D)$ [36]. . . . .	42
5.5	A grid of hash codes applied to an image. These can be compared to a database to find the location of the image in the night sky [36]. . . . .	42
5.6	Schematic view of the prototype Sun sensor mode activity flow used in testing. . . . .	44
5.7	A raw test image to investigate and tune the algorithm of the Sun sensor mode. . . . .	45
5.8	A processed test image through a Gaussian filter. The white circle is positioned on the coordinates of the brightest pixel. . . . .	45
6.1	The sensor module is placed on a platform that can be levelled, so that it points accurately towards zenith. . . . .	49
6.2	Overview of test setup elements for the Sun sensor tests. . . . .	51
6.3	Schematic overview of LED light collimated through a lens. . . . .	52
6.4	Sun sensor success rate for different analogue gain and exposure time settings. . . . .	55
6.5	Sun sensor solving times for different analogue gain and exposure time settings. . . . .	56
6.6	De-noised and post-processed image of the stars with 0.500 [s] exposure time and analogue gain of 12.0. The Cassiopeia constellation is visible just right of the centre. . . . .	57
6.7	Zoomed-in image of the 3 Persei - HIP 9222 star and its surrounding stars and constellations. Cassiopeia and part of Andromeda have been drawn out, together with the names of their brightest stars. . . . .	57
6.8	The right ascension and declination found by the star tracker mode, compared to the actual position of Zenith at that time of day. . . . .	58
6.9	An oval-shaped Sun-spot is present at large azimuth and elevation angles. . . . .	60

---

6.10 Angular error of the Sun sensor in relation to azimuth and elevation angles. . . . .	61
A.1 Gantt chart of the planning of the thesis. . . . .	70
C.1 QR-code to GitHub repository. . . . .	77

# List of Tables

2.1	A selection of state-of-the-art Sun sensors [17] [18]. . . . .	6
2.2	An overview of currently available COTS Sun sensors for CubeSats and PocketQubes. . . . .	8
2.3	Star trackers that are currently available on the market. . . . .	12
3.1	Time allocated for different thesis phases. . . . .	21
4.1	Requirement list for the flight-ready combined versatile attitude sensor. . . . .	24
4.2	Requirement list for the prototype combined versatile attitude sensor. . . . .	26
4.3	Requirement list for the commercial-off-the-shelves optical module. . . . .	27
4.4	Specifications of commercial-off-the-shelf optical modules and their trade off results. (1/2) . . . . .	29
4.5	Specifications of commercial-off-the-shelf optical modules and their trade off results. (2/2) . . . . .	30
4.6	Detailed specifications of the OV9281-A optical module [34]. . . . .	32
4.7	The number of stars and their luminosity for different apparent magnitudes [35]. . . . .	34
4.8	Approximated power consumption of different sensor resolution modes. . . . .	36
4.9	The predicted effects of a reduced update rate on power consumption for different sensor modes. . . . .	37
5.1	Settings and predicted power consumption of combined sensor prototype modes. . . . .	41
6.1	Overview of the tests performed and their locations in this document. . . . .	46
6.2	Intensity and incidence angle calculations for two different light source setups. . . . .	53
6.3	Results of the star tracker functionality test using different exposure and analogue gain settings. . . . .	54
6.4	Accuracy results of the star tracker performance test. The error values contain both the mean error and the 1-sigma standard deviation. . . . .	58
6.5	Results of the Sun sensor functionality test. . . . .	59

# Nomenclature

## Abbreviations

Abbreviation	Definition
ADCS	Attitude Determination and Control System
AG	Analogue Gain
CMOS	Complementary Metal Oxide Semiconductor
COTS	Commercial-Off-The-Shelf
CPU	Central Processing Unit
CSS	Coarse Sun Sensor
CVAS	Combined Versatile Attitude Sensor
DSS	Digital Sun Sensor
EKF	Extended Kalman Filter
FLR	Flight-Ready Combined Sensor
FOV	Field Of View
GEO	Geosynchronous Equatorial Orbit
IR	Infrared
LCD	Liquid Crystal Display
LED	Light-emitting Diode
LEO	Low Earth Orbit
MP	Megapixel
PCB	Printed Circuit Board
PROTO	Prototype Combined Sensor
RTSF	Real-Time Sequential Filters
S/N	Signal-to-Noise Ratio

## Symbols

Symbol	Definition	Unit
$D$	Aperture diameter	[m]
$E$	Luminosity	[ $W/m^2$ ]
$U$	Voltage	[V]
$V$	Apparent visual magnitude	[-]
$\theta$	Sun azimuth angle	[°]
$\lambda$	Wavelength	[nm]
$\phi$	Sun elevation angle	[°]

# Introduction

There is a need for an optical attitude sensor for small satellite platforms that is more versatile and less intensive on technical budgets than currently available sensors. New developments in the space industry have led to satellites becoming smaller and smaller [1]. The technology on these small satellite platforms, such as CubeSats, needs to decrease in size and power consumption in order to fit on the satellites as well. However, the attitude determination subsystem often consists of several sensors that work together to determine the correct attitude [2]. Moreover, the availability of these sensors is limited by the rotational speed of the spacecraft, the presence or absence of sunlight and the viewing direction of the sensor, which leads to sensors being under-utilised and taking up vital volume throughout a mission [2] [3]. In addition, engineers would like to improve the pointing accuracy of their spacecraft, but accurate star trackers often consume too much power for small satellites [4].

The aim of this thesis is to design and test a new attitude sensor for CubeSats and PocketQubes that improves the versatility and technical budgets of existing COTS sensors, while offering performance that is adequate for most CubeSat and PocketQube missions. A multitude of attitude sensors were analysed and potential research areas were identified. Researchers already explored combining a Sun and Earth horizon sensor onto a single PCB, with the idea that the sensor can be used in both eclipse and sunlight. This sensor would operate in the IR spectrum, making it less sensitive to albedo effects. However, the Earth horizon sensor mode struggled to achieve the desired accuracy [5]. Another ongoing research is the use of optical filters to block albedo from Sun sensors. Specific light spectrum bands can be blocked, so that the effect of albedo on the accuracy of the sensor is mitigated. However, the impact of such a filter appears to be limited and other methods to block the albedo are more promising. An entirely different concept for a more versatile attitude sensor is to combine a star tracker and Sun sensor into a single sensor. Both sensors can operate using the same imaging sensor, which would allow for a sensor that can function in sunlight, eclipse and while tumbling, while providing medium to high accuracy. As a consequence, the number of sensors required on a satellite can be reduced. However, creating such a sensor could be difficult, since these two techniques require vastly different sensor configurations. Still, considering the possibility for a significant improvement in versatility and technical budgets, it was decided to pursue the design of a 2-in-1 star tracker and Sun sensor.

This thesis document is structured in the following way: first, the problem is investigated and different attitude determination techniques are discussed in chapter 2. Thereafter, chapter 3 presents the research question, hypothesis and methodology used in this thesis. Then, the preliminary design phase is explained in chapter 4, where requirements are generated and a COTS CMOS sensor is selected. The design is worked out in more detail in chapter 5, before the test setups and results are presented in chapter 6. These results are discussed in chapter 7. Finally, conclusions and recommendations are given in chapter 8. Additional information can be found in the appendices.

# Problem Investigation

At the beginning of this thesis a literature study is performed on Sun sensors, star trackers and other ADCS systems in order to identify the current state of their technologies. These sensor types have several challenges that need to be overcome in order to achieve good accuracy. Also, they must be compatible with the CubeSats and PocketQubes form factors, mostly in size and power consumption. These challenges are explained in this literature study, as well as a discussion on the sensor's areas that have not seen much research yet. Subsequently, this literature study is used in the creation of a research question.

This chapter first explains why a versatile optical attitude sensor is needed in section 2.1. Then, a detailed explanation of Sun sensor and star trackers is given in section 2.2 and section 2.3. Here, their most important design factors are presented, as well as an overview of their limitations. Furthermore, an overview of currently available COTS sensors is provided. Then, several other ADCS systems are explored in section 2.4. Finally, section 2.5 elaborates on what has not been researched yet regarding Sun sensors and what might be worth investigating in the future.

## 2.1. Need for a versatile optical sensor

Lately, the space industry has seen the emergence of private companies entering the market. Satellite components can be bought from manufacturers and space on launch vehicles can be ordered as well. The focus of these private companies is to develop low-cost technology for space, which makes space more accessible to a wider public [1]. With low-costs in mind, several small satellite platforms have been created, such as CubeSats and PocketQubes. These platforms have a standardised form factor, which makes development and launch vehicle integration easier.

The rise of CubeSats and similar small satellites also means a rise in the miniaturization of spacecraft systems. Attitude determination systems need to be made smaller and less power consuming, since volume and electrical power are severely limited on small satellites. At the same time, the performance of these systems must be preserved. However, the miniaturization of sensors can lead to performance losses and therefore the requirements for attitude determination are often relaxed. Still, some space missions require strict pointing accuracies for their payloads, but current attitude sensors cannot provide this in a package suited for CubeSats or smaller.

Furthermore, spacecraft often require a combination of several sensor types, because not every sensor can be used in each flight condition. For instance, star trackers need to block out the Sun and Earth from their measurements and cannot operate in dynamic conditions, such as tumbling. Using a combination of sensors means that more volume and a higher power consumption is used on the spacecraft, which hinders the capabilities of the overall design.

Therefore, there is a need for a versatile optical attitude sensor that improves the performance of existing designs and that fits onto small satellite platforms, such as CubeSats and PocketQubes. With versatile it is meant that the sensor should be capable of operating in a wide variety of conditions, such as in direct sunlight, eclipse or while tumbling. In addition, the sensor should be designed to deliver high performance for CubeSats and medium performance for PocketQubes. This should enable more advanced payloads to be installed in future missions.

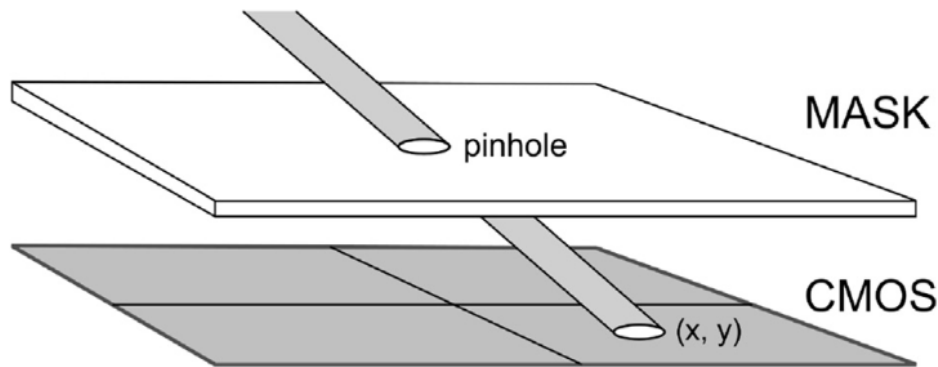


**Figure 2.1:** A schematic overview of the mask and CMOS surface. Where the light ray falls on the CMOS is dependent on the angle of the Sun to the mask [12].

## 2.2. Sun sensor technology

Sun sensors constitute of multiple photosensitive elements placed on the surface of a satellite that measure the direction of the incident sunlight. The position of the Sun is derived, often in 2-axis, from which the attitude of the spacecraft is can be determined [2]. Potentially, Doppler shift techniques can be used to derive the attitude in 3-axis [6] [7]. A common measurement principle is that sunlight enters the sensor through a slit or hole, after which it hits photosensitive elements that are closely set off from each other. The incident angle of the sunlight can be calculated this way [6]. With these fine measurement techniques, digital Sun sensors (DSS) can often get an accuracy of around  $0.1-1.0^\circ$  [8]. Some spacecraft make use of the power generated by their solar cells to determine the solar position, but these methods are often regarded as coarse Sun sensors (CSS) due to their lower accuracy [9] [10]. For this thesis, only DSS will be considered.

A requirement for Sun sensors to work is that the Sun is visible. This means that spacecraft with long eclipse times call for complementary sensors, which is especially true for spacecraft in LEO. In addition, spacecraft close to the Earth also suffer from the Earth's albedo effect. This means that part of the light collected by the photosensitive elements is light reflected from Earth, which lowers the sensor's accuracy by  $1-10^\circ$ , depending on the method and strength of the albedo effect [2] [11]. Luckily, several filtering techniques have been created that aim to reduce the impact of albedo on the accuracy of the Sun sensor.

The following sections will go into more detail regarding their designs, what the limitations of the system are and how they can be reduced. Finally, an overview of the currently available COTS Sun sensors will be presented.

### 2.2.1. Physical design

The most common Sun sensor methods use a small diaphragm that lets a narrow collimated ray of sunlight through onto photosensitive elements. These elements are most commonly a  $2 \times 2$  patch of photodiodes, called a quadrant detector, or an active pixel sensor, like the technology found on a CMOS camera. The diaphragm is often called a mask. Figure 2.1 presents a simplified overview of light passing through the mask onto a CMOS surface. Which photosensitive elements are illuminated depends on the angle of the Sun to the sensor mask. The Sun vector can be determined from the coordinates of these elements, which is often done using trigonometry [12]. This principle also holds for quadrant detectors, but not for cosine detectors, which utilize the current of photocells to derive the angle of the Sun vector.

Determining the center of the Sun spot, called the centroid, is often difficult because the spot itself is not always a perfect circle. Some of the factors that present challenges to the Sun sensor have been highlighted in subsection 2.2.3.

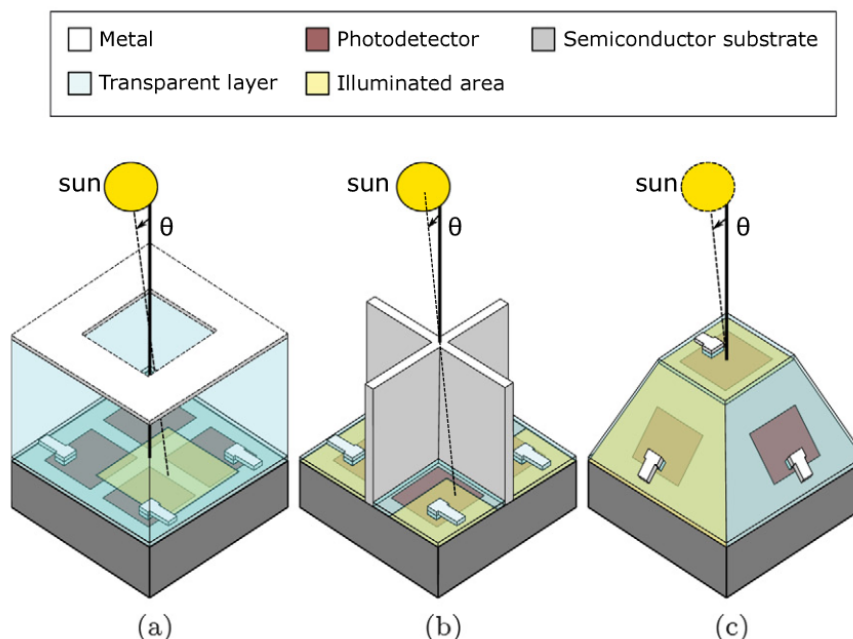


**Figure 2.2:** Three different sun sensor types: a) collimating sensor, b) Sun-pointing sensor and c) tilted-mount sensor [15].

### 2.2.2. Sensor layouts

There are different sensor layouts that can be used with the pin-hole principle. The aforementioned method is often called four-quadrant detection in the case of a 2x2 array of photodiodes and a digital Sun sensor when a larger array is used [13]. Another pin-hole method is single detection, where only a single photosensitive element is used. This method is simpler and can be as accurate as a four-quadrant sensor through the use of error models, but its FOV is often limited [14]. Hence, the single detection method is not widely used in space and will therefore not be investigated in this thesis. These collimating sensors can be seen in Figure 2.2 a).

Another different Sun sensor approach is the Sun-pointing sensor, which is visualized in Figure 2.2 b). Here, panels surround multiple photodiodes such that light and shadows are cast on them, depending on the angle of the Sun. The current over the photodiodes is then compared to derive the Sun's position [15] [14]. Again, this method is simpler than a collimating sensor, as it does not require a complex control algorithm. On the other hand, its performance is slightly worse and the sensor is taller because of the panels that create a shade.

The tilted-mount sensor in Figure 2.2 c) has been used in spacecraft for several decades. Often, the sensor has the shape of a pyramid with photodetectors on its sides. The photodetector with the highest current is facing the side where the Sun comes from. This method benefits from a wide FOV, high sensitivity and simple design. However, the system takes up a lot of volume and is therefore not suited for NanoSats [14]. This method is also the least accurate of the methods mentioned here, although it is still good enough for most space missions.

### 2.2.3. Factors impacting performance

The following section applies to the performance of a collimating Sun sensor with an active pixel sensor. The accuracy of the Sun sensor is mostly dependent on the number of pixels on the CMOS surface, the size of the light ray and the thickness of the mask. A higher number of pixels and more densely packed pixels mean that the position of the incidence ray can be determined more accurately. Then, the smaller the size of the light ray, the fewer the amount of pixels that are illuminated. This also reduces the effects of stray light entering the sensor and causing inaccuracies. In order to achieve this, the mask hole size should be kept as small as

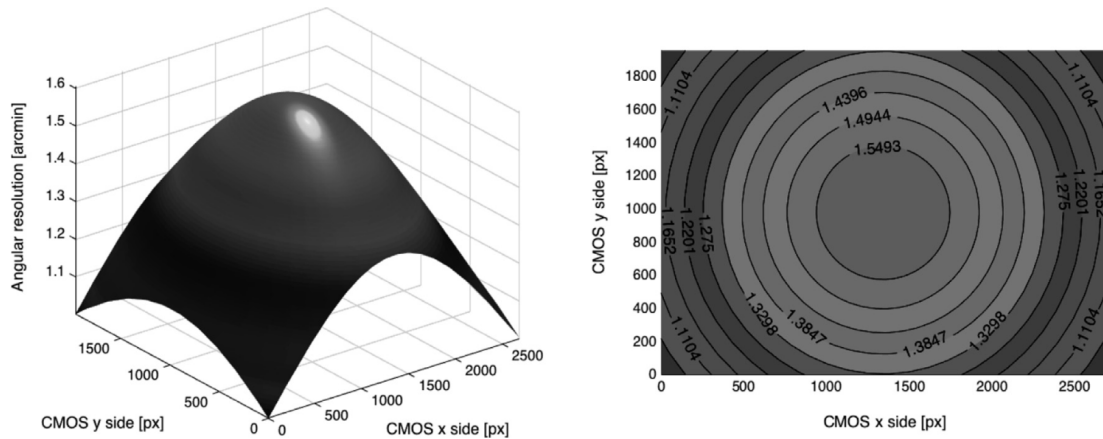


**Figure 2.3:** Three-dimensional and contour plot of the resolution of the CMOS sensor from Antonello et al. [12].

possible and with as little defects as possible. Finally, the mask itself should be kept as thin as possible, as the mask can cast a shade on the CMOS layer, which disturbs the shape of the light spot. Pelemeshko et al. noted that a conical pin hole would reduce this effect substantially compared to a cylindrical pin hole [16]. Not only would it allow for a wide field of view, but the conical shape allows for a thicker mask, which results in an easier to manufacture and stronger mask. The latter is of interest regarding the presence of micro-asteroids and micro-debris in LEO and GEO.

Other factors on the accuracy are the angular diameter of the light source and the coordinates of the illuminated CMOS pixels. The angular diameter of the Sun has an impact on the accuracy, since it creates light rays that are not fully parallel to each other. This makes the light spot on the CMOS surface less sharp and causes more pixels to be active, which reduces accuracy. For orbits close to Earth the angle of the non-parallel light rays can be modelled to  $0.5^\circ$  [12]. The exact angle for albedo rays is unknown, but it can be assumed that those rays are scattered and therefore cause an unclear image on the sensor. With regards to the coordinates of the illuminated CMOS pixels, Antonello et al. showed that for low elevations the sensor has a lower resolution. This is linked to cosine of the incidence angle, which causes small changes in incidence angle to have a smaller effect at low elevations compared to high elevations. This effect is described by Equation 2.1, where  $h$  is the distance between CMOS and mask,  $r$  is the distance of the sun spot to the center of the CMOS,  $t$  is the thickness of the mask and  $px$  is the size of a pixel. The resulting sensor resolution can be seen in Figure 2.3 [12].

$$a(r) = \tan^{-1}\left(\frac{r}{t+h}\right) - \tan^{-1}\left(\frac{r-px}{t+h}\right) \quad (2.1)$$

Another important parameter of each Sun sensor is its FOV. This indicates how wide the sensor is looking for the Sun. A wide FOV is often required for a satellite, since the collection of Sun sensors should cover all angles into space for attitude determination. Typical values in current COTS sensors are around  $100^\circ$  [8]. The FOV is dictated by the size of the CMOS surface and the distance between the mask and the CMOS surface. Decreasing the distance between the two surfaces can greatly improve the FOV of the sensor, but this can increase inaccuracies caused by the pin hole and mask thickness [16]. Therefore, designing a Sun sensor requires a compromise between these two.

#### 2.2.4. Impact of Earth albedo

A spacecraft in orbit around Earth experiences directly sunlight and sunlight that is reflected from the Earth. This indirect sunlight is called albedo and its magnitude is highly dependent on the spacecraft's orbit, weather and seasonal changes [11]. Strong reflective surfaces and regions, such as ice at the poles, will result in a stronger albedo than a less reflective region, like rainforests. Zhang and Zhang noted that the albedo at the

Spring Equinox is at maximum 25% of the solar constant, while around the Summer Solstice this can be 40% [9]. This poses a problem for Sun sensors, as this albedo light can interfere with attitude determination. This is because albedo is diffused light from multiple directions and it does not have a constant intensity either [9]. Therefore, it will enter the Sun sensor under a different angle than the direct Sun ray. This stray light decreases the accuracy of quadrant sensors and photocells substantially, since they cannot distinguish between sunlight and albedo light. Active pixel sensors are less affected by this, since they can apply filtering techniques during post-processing.

It is possible to remove some of the albedo effects on photocells by using albedo models that predict the albedo intensity. These models divide the Earth up into small sections of roughly  $1^\circ \times 1^\circ$  and determine their albedo coefficients based on the time of year [10]. Then, the sun sensor can predict the albedo effect based on the position of the satellite, and remove it.

Digital Sun sensors (DSS), like the mask-CMOS design presented in subsection 2.2.1, can make use of post-processing algorithms to remove albedo [12] [15]. Still, Romijn et al. suggests that sun sensors can be made that are inherently insensitive to albedo. There exist bands in the IR spectrum of albedo light that has been absorbed by the Earth's atmosphere. A spectral filter can be installed that selectively lets sunlight through at specific wavelengths, but not albedo light. Or, a sensor can be configured for such a band so that only direct sunlight is picked up by the sensor. Romijn et al. made a sensor using a silicon carbide integrated chip that only picks up light in the UV range. These wavelengths have considerably less albedo and therefore this sensor is less affected by it. The design was made on a wafer, enabling a very small sensor design of only  $10 \times 10 \times 1$  [mm]. An accuracy of  $5.7^\circ$  was obtained with a FOV of  $\pm 37^\circ$  [15]. There is room for improvement in this design, as it was a proof-of-concept.

## 2.2.5. State-of-the-art Sun sensors

As mentioned in subsection 2.2.1 and subsection 2.2.2, a wide variety of Sun sensors has been designed in the past. Moreover, plenty of studies have been conducted to improve the performance of Sun sensors throughout the years. Table 2.1 presents a selection of state-of-the-art Sun sensors and their specifications.

**Table 2.1:** A selection of state-of-the-art Sun sensors [17] [18].

Sun sensor manufacturer	Galileo ESA	Xie and Theuwissen	Leñero-Bardallo et al.	Gomez-Merchan et al.	Gomez-Merchan et al.
Type	APS Digital Sensor	APS Digital Sensor	Event Based Luminance Sensor	Event Based Luminance Sensor	Continuous Mode Luminance Sensor
Special features	Aquisition-tracking modes, designed for radiation hardness	A very small prototype sun sensor from 2012	Information-centric sensor	Information-centric sensor	Information-centric sensor
FOV [deg]	128	94	146	88.67	88.67
Resolution [deg]	0.005	0.004	0.03	0.0048	1.23
Accuracy [deg]	0.024	0.01	0.013-0.05	0.012-0.043	2.37-5.82
Avg. Power Consumption [mW]	327	21	52	1.07	0.063
Update Rate [Hz]	10	10	200	1000	5000
Operating Temperature	-40 to +70 degC	-40 to +80 degC	N/a	N/a	N/a
Radiation Hardening	30 krad	30 krad	N/a	N/a	N/a
Chip dimensions (LxWxH)	11x11 mm	5x5 mm	4.120x3.315 mm	1.318x1.318 mm	1.516x1.516 mm

Of the sensors stated in Table 2.1, the Galileo APS Digital Sensor has seen operation in space. It was used to provide attitude determination for the Galileo satellites. This sensor has a very wide FOV of  $128^\circ$ , a resolution, which is the smallest observable change in angle, of  $0.005^\circ$  and an accuracy of  $0.024^\circ$  [17]. The main limitation of this system is that it consumed on average 327 [mW] of power, which is too much for NanoSats. This design has been surpassed in terms of power consumption by the four other Sun sensors, while they are still able to achieve similar accuracy, if not better.

Leñero-Bardallo et al. managed to reduce the data produced and power consumed by Sun sensors by switching to an information-centric sensor, compared to a data-centric sensor. Instead of processing raw data of all pixels, only data of pixels that were illuminated by the Sun would be processed. This method allowed the sensor to achieve higher update rates as well [18]. While the resolution of Leñero-Bardallo et al. is six times worse, its accuracy was on par with the sensor from Galileo. In addition, the update rate was increased from 10 [Hz] to 200 [Hz], which makes the sensor better suited for fast-tumbling scenario's and it can filter out false readings more easily [17].

Gomez-Merchan et al. improved the Event Based Luminance Sensor concept by switching the pixels from a photoconductive mode to a photovoltaic mode. Instead of measuring the current through a pixel, the pixel now acts as a binary device that outputs a high voltage when it is illuminated. This method consumes no power while operating continuously. Furthermore, the centroid of the Sun spot on the sensor is computed on-chip, which further decreases power consumption and data rates. This design brought the power consumption down to 0.063 [mW] and increased the update rate to 5000 [Hz], but at the cost of a resolution and accuracy above  $1^\circ$  [18]. However, Gomez-Merchan et al. created an Event Based Luminance Sensor with similar principles that achieved performance comparable to Galileo, but with a power consumption of only 1.07 [mW]. The impact of this algorithm on the power requirements of a spacecraft are significant and is worth investigating further.

### 2.2.6. Current COTS market

Demand for small, low power and effective Sun sensors has increased with the rise of small satellites. Several companies offer Sun sensor solutions for CubeSats and PocketQubes that are space-ready. Table 2.2 presents an overview of COTS Sun sensors and their most important specifications. The overview consists of popular optical sensors and optical sensors that, albeit less popular, come in an extremely compact form-factor. The symbol  $N/a$  has been used wherever a value was not provided by the company.

A number of conclusions can be drawn from Table 2.2. First, there exists a wide variety of Sun sensors designed for space that are lightweight, low in power consumption and are radiation hardened. The difference between the available Sun sensors lies mostly in their performance and special features. Some sensors, like the CubeSense Sun, have been designed for CubeSats specifically, which gives them more room in their design than those designed for PocketQubes or similar. This allows them to include more features to enhance the performance, like an optical filter, but they increase power consumption. On the other hand, a sensor like the Needronix Eagle was designed for a smaller form-factor, which requires it to be less power consuming. The accuracy between these two sensors appears to be similar, but the Needronix Eagle is sensitive to albedo, which lowers its accuracy in real space applications.

Furthermore, it appears that an 1-sigma accuracy of around  $0.1^\circ$  or better is feasible with current technologies. This should be sufficiently accurate for most CubeSat and PocketQube missions. However, the companies do not state how good their sensors perform when under the effects of albedo. As mentioned in section 2.2, albedo can decrease the accuracy of Sun sensors easily to  $1-10^\circ$  if no mitigation strategies have been applied. Therefore, new Sun sensor designs should not focus on improving the outright accuracy of the sensor, but should focus on reducing the sensitivity to albedo. Ideally, this is done without increasing the power consumption.

Needronix is marketing another feature on their Sun sensors, which is that they fit in between the body-mounted solar panels on an 1U CubeSat [8]. The length and width of the sensors are chosen such that they can be positioned in a place that otherwise would see little use on a spacecraft. It is unsure whether this space is available on each CubeSat, but it could be worth to design a new sensor around the possibility of placing it in a particularly convenient area of the satellite. For instance, body-mounted solar panels often have a triangular cut out in their top corners, which could provide enough space for a Sun sensor.

**Table 2.2:** An overview of currently available COTS Sun sensors for CubeSats and PocketQubes.

COTS Sun sensor	CubeSense Sun	AQUILA-D02 Sun Sensor	SSOC - A60	SS200	NanoSense FSS	NXSS3V10 Eagle	NXSS3V50 Eagle Plus
Company	CubeSpace	NewSpace Systems	Solar MEMS	AAC Clyde Space	GomSpace	Needronix	Needronix
Special features	Albedo immunity, wide FOV	Optical filter	-	-	Fits between CubeSat solar panels	Fits between CubeSat solar panels	Fits between CubeSat solar panels
FOV [deg]	166	140	60	110	120	110	110
Accuracy [deg]	0.2 (2 sigma)	0.2 (RMS)	0.3 (3 sigma)	0.3 (1 sigma)	2.0 (3 sigma)	0.09 (1 sigma)	0.0015 (1 sigma)
Avg. Power Consumption [mW]	100	150	125	1.5	11.6	7	15
Peak Power Consumption [mW]	174	150	125	40	N/a	7	15
Update Rate [Hz]	2	5	N/a	up to 10 Hz	Up to 100 Hz	60	166
Temperature	-20 to 80 degC	-25 to 70 degC	-45 to +85 degC	-45 to +85 degC	-40 to +100 degC	-45 to +85 degC	-45 to +85 degC
Radiation Hardening	24 krad	20 krad	100 krad	36 krad	N/a	N/a	20 krad
Dimensions (LxWxH)	35x22x24 mm	34x40x20 mm	40x30x12 mm	15x24.7x3.5 mm	22x11x5 mm	15x15.5x4.6 mm	29.5x11.5x6.5 mm
Mass [g]	15	37	25	3	2.2	3	5

### 2.2.7. Sun sensor limitations

Some deficiencies in the design of Sun sensors have already been mentioned in the previous sections. For instance, most sensors are sensitive to albedo and therefore need to make use of filtering algorithms or albedo models to improve accuracy. This section will detail further areas of the design that can be improved in the future.

#### 2.2.7.1 Physical dimensions

Currently, there is a strong focus on miniaturization in space flight. Satellites are becoming smaller, which means there is a need for smaller Sun sensors. Unfortunately, reducing the size of a Sun sensor often reduces the performance of the system, since a smaller camera or sensor surface has to be used. This leads to decreasing accuracy. On the other hand, it can be argued that this is a hurdle the space industry must take by momentarily relaxing the performance requirements of their missions. New sensors are already showing that sufficient performance can be reached with very small sensors.

The major benefit of smaller sensors is that they can be placed on smaller satellites, like NanoSats. This would allow a vast number of new missions to have reliable and accurate attitude determination with little resource costs. As mentioned in subsection 2.2.6, smaller sensors could be placed in spots on the spacecraft that currently serve no function. Moreover, smaller sensors also mean that the power consumption is likely to be reduced, which makes the sensors even more suitable for small satellites.

Right now, the smallest COTS Sun sensors have an area of around 15x15 [mm]. New manufacturing techniques, such as the integrated chips from Romijn et al., can make significant improvements in decreasing the sensor's surface area. New techniques in CMOS surface and optics can also help to reduce the surface area. With developments like these, COTS sun sensors of 10x10 [mm] might be possible in the near future.

#### 2.2.7.2 Eclipse performance

Another limitation of Sun sensors is that they cannot operate in eclipse conditions. This follows from the fact that they require direct sunlight for operation. Considering that most small satellites operate in LEO, where eclipse periods can last around 35 [min], this makes Sun sensors not a viable attitude sensor without help from another sensor type [19]. It appears this limitation cannot be resolved in a simplistic way, since it is a problem inherent to the Sun sensor method.

However, it might be possible to integrate different sensor types into one, which would reduce the total sensor volume budget and would potentially lower the power consumption of the overall spacecraft. For instance, Pelemeshko et al. created a Sun sensor coupled with an infrared Earth horizon sensor [16]. This system was only 42.5x17.5x11 [mm] in size and made positioning the sensors on the spacecraft easier.

Still, this form of sensor integration can be taken a step further. A completely new Sun sensor could be developed that works as regular Sun sensor and Earth horizon sensor at the same time. As explained in subsection 2.2.4, several bands exist in the IR spectrum of albedo that are absorbed by the atmosphere and therefore do not reach the Sun sensor. Romijn et al. showed that an albedo insensitive sensor can be made by utilizing these wavelength bands. An Earth horizon sensor detects the IR emitted by the Earth to find its center. Therefore, the sensor also works in eclipse. Perhaps a sensor can be made that combines these two methods into one. For this to work, the FOV of the sensor designed by Romijn et al. needs to be increased, as well as its accuracy under direct sunlight.

Meanwhile, Kapás et al. is in the process of designing 2-in-1 Sun sensor and Earth horizon sensor using thermal imaging sensors. Their solution will utilize a COTS IR sensor with a wide FOV in order to achieve a thermal image of space in  $4\pi$  steradian. The sensor will be suited for nano-satellites and will provide sub-degree accuracy [5]. Kapás et al. showed that the prototype is already able to determine the Sun vector, but Earth horizon detection testing has not been carried out yet. However, a test with high-altitude balloons will be completed so that the system can be validated. A follow up paper from Takátsy et al. performed simulations

of the sensor and found that the sensor did not perform as good as a typical Earth horizon sensor in eclipse. An attitude determination error of  $25^\circ$  was detected in the simulations, which is quite high. It could be that this was due to the simulated gyroscope drift [20]. It is recommended that this sensor is tested in a high altitude experiment to properly validate its accuracy.

### 2.2.7.3 Two-axis measurements

In general, a Sun sensor only provides attitude determination in 2-axis. It is able to provide the satellite with information on the azimuth and elevation of the Sun, but not the satellites rotation with respect to the Sun. Since for full attitude determination all three axis need to be known, spacecraft often use additional attitude sensors to establish the roll angle [2]. Designing a 3-axis Sun sensor removes this dependency and could significantly decrease the size and mass of the entire ADCS system of a spacecraft.

Liebe et al. has investigated a method where the roll angle can be determined through Doppler shift on the solar spectrum. Since the Sun rotates at around 2 [km/s] at its equator, the difference in speed between one end and the other will cause a shift in the wavelength of the solar spectrum. A camera pointed to the Sun can detect these shifts and can determine the Sun's roll angle from it. Subsequently, this is used to achieve 3-axis attitude determination for the spacecraft [7]. Liebe et al. proved the concept can work, but it needs to be miniaturized before it can be installed on small satellites. Miniaturizing the system will be out of the scope of the thesis, since the system weighs currently 1.5 [kg] and consumes 3 [W] of power, which cannot easily be downsized to CubeSat-level.

## 2.3. Star tracker technology

Star trackers take pictures of the universe surrounding the spacecraft and compare those pictures with a database of the night sky. An algorithm tries to identify star constellations and, since the position of stars appear to be fixed, determines the orientation of the spacecraft from this [2]. This can be done in 3-axis accurately to at least  $0.1^\circ$  by systems designed for small satellites [21]. New data processing algorithms, like one proposed by Jiang et al., have improved the speed of the trackers up to 10 [Hz] [2] [22]. This makes star trackers good candidates for missions with strict attitude determination requirements.

However, star trackers suffer from several major drawbacks that require them to be used in conjunction with other ADCS systems. Most notably, the system struggles in tumbling situations, since this motion will result in a blurred image, which is difficult for the algorithm to process [2]. Some star trackers utilize de-blurring techniques on its images to improve performance while tumbling, but these increase the strain on data processing and increase power consumption. Still, star trackers can be deemed inaccurate beyond a slew rate of 2-3 [ $^\circ$ /s], although recent technological improvements could have raised this limit by 1-2 $^\circ$  [3] [23]. Furthermore, star trackers are susceptible to temperature effects and stray sunlight entering the camera. Baffles are used for the latter, but these make the sensors increase in size and limit their field of view (FOV) [23]. CubeSats and smaller satellites often do not have enough space available for these systems and therefore choose to lower their ADCS requirements so that simpler attitude sensors can be used. However, since a few years some companies offer star trackers designed for CubeSats, so these are becoming more and more common. For instance, research is being done into deployable baffles to keep the system's size small.

This section will explain in more detail how star trackers work, give several examples of currently available commercial-off-the-shelf trackers and their limitations will be discussed.

### 2.3.1. Star tracker design

Star trackers are essentially cameras that take pictures of the stars. A schematic of a star tracker has been presented in Figure 2.4. Typically, the tracker consists of a lens and imaging detector at the core, with a baffle in front of it to prevent stray light from entering the camera. The detector is connected to a PCB, which

processes the images [23]. Often, these components together can take up a large amount of volume, which leaves little space left for other instruments on CubeSats and PocketQubes. Therefore, one of the focus points in new star trackers is to reduce their size, as will be explained in subsection 2.3.3.

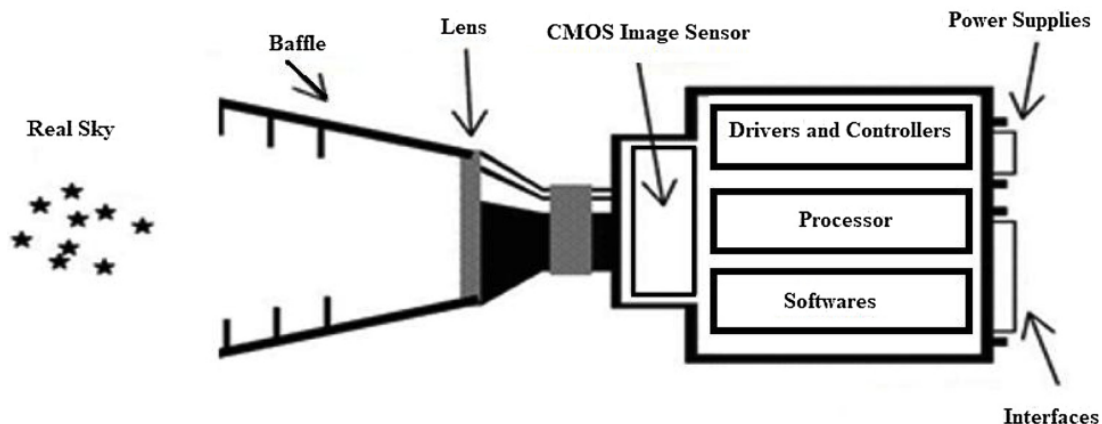


Figure 2.4: A schematic cross-section of a star tracker [24].

First light travels through the baffle towards the lens. Stray light, such as sunlight and albedo, should be blocked out as much as possible, since it can create an overexposure of the imaging sensor. This makes identifying the centroid of a star more difficult and reduces the accuracy of the sensor. A longer and narrower baffle is more effective at preventing stray light from entering the aperture and generally improves the performance of the tracker. However, a longer baffle also means that the FOV of the sensor is reduced, which limits the amount of stars that can be identified in a single image [23]. Still, designers try to maximize the size of the baffle within the constraints of the spacecraft's design for performance.

Once the light has travelled through the baffle, it gets redirected onto an imaging sensor using a lens. This is often a CMOS sensor and produces an image of the stars in view. Since stars are faint objects, an image sensor has to either increase its aperture or its exposure time. Both increase the total amount of energy hitting the sensor in a single image. However, increasing the aperture makes the star tracker bigger, while increasing the exposure time makes the system susceptible to high angular velocities that cause blurred images [23]. Longer exposure times can also lead to a decrease in time available for analysing the images. Therefore, these two design parameters need to be balanced.

Once the light has been collected by the imaging sensor, an algorithm is applied to determine the attitude of the spacecraft. This is done in three steps [2].

First, the centroid of each star in the image is calculated. A star appears as a collection of illuminated pixels on the image, for which an algorithm analyses and calculates the centroid. The goal of the algorithm is to perform this step as efficient as possible so that the update rate and power consumption of the star tracker is kept to a minimum [24]. Jiang et al. explored three centroid determination algorithms that improved the tracking speed and the update rate of a star tracker [22]. Second, the position of the stars is compared to a database in order to identify which stars are in the sensor's FOV. Similar to the centroid determination, this step should be done as efficiently as possible. A large amount of storage on the sensor's electronic systems is required for the database and searching through it makes up the greatest portion of the tracker's power consumption. Some star trackers group stars together and form geometrical patterns between them, so that they can be more easily compared to the database [24]. Third, the attitude of the spacecraft is determined. If multiple star trackers are installed on the spacecraft, then their results can be combined to achieve more accurate results. Most star trackers have a lost-in-space mode and a tracking mode. Initial attitude determination is done using the lost-in-space mode, which last a couple of seconds [22] [24]. Then, the tracking mode is used to maintain the correct orientation for the spacecraft. This entire process is done at around 10 [Hz] for trackers currently available and sensors regularly use previous images to improve their accuracy [24].

### 2.3.2. Current COTS market

**Table 2.3:** Star trackers that are currently available on the market.

Name	CubeStar	ST200	Twinkle	VST-41M	CT-2020
Company	CubeSpace	AAC Clyde Space	Arcsec	Vectronic Aerospace	Ball Aerospace
FOV [deg]	42	N/a	10.6	14	30
Accuracy [deg]	0.02 / 0.06 (cross-axis/roll, 3 sigma)	0.0083 / 0.0556 (pitch-roll/yaw, 3 sigma)	0.0083 / 0.05 (pitch-roll/yaw, 3 sigma)	0.005 / 0.0339 (pitch-roll/yaw, 2 sigma)	0.000417 (3 sigma)
Avg. Power Consumption [mW]	165	700	600	N/a	8000
Peak Power Consumption [mW]	271	1000	N/a	2500	12000
Update Rate [Hz]	1	5	10	4	100
Temperature	-20 to +80 degC	-20 to +40 degC	N/a	-20 to +65 degC	N/a
Radiation Hardening	24 krad	9 krad	Radiation shielded and tested	20 krad	Radiation Hardened
Dimensions (LxWxH)	35x49x24 mm	29x29x38.1 mm	20x20x40 mm	80x100x180 mm	145x145x305 mm
Mass [g]	47	42	35	800	3000

Although star trackers are large and consume a fair amount of power, commercial-off-the-shelf star trackers for small spacecraft have been designed and used over the last two decades. A selection of COTS star trackers that are currently available can be seen in Table 2.3 [13]. These five star trackers were chosen based on popularity and performance. For instance, the CT-2020 by Ball Aerospace is likely not suited for CubeSats because of its size, weight and power consumption, but it was included on the grounds of its excellent accuracy.

Several key differences between star trackers and Sun sensors can be identified by comparing Table 2.3 with Table 2.2. Star trackers have a narrower FOV, higher power consumption, larger physical dimensions and larger mass. Their update rate is comparable, although this depends on the algorithm and processing unit used in the star tracker. On the contrary, star trackers have a better accuracy that is almost an order of magnitude better than the best performing Sun sensors.

CubeSpace, AAC Clyde Space and Arcsec have managed to design a star tracker that appears sufficiently small to fit onto a CubeSat. These sensors take up a volume that is only a couple of cubic centimetres and have a mass below 50 [gr]. This is promising for future CubeSats as this leaves a substantial amount of room left for other subsystems. Still, it is likely that spacecraft require two star trackers for attitude determination, while also requiring other sensors such as Earth horizon sensors or magnetometers for when the spacecraft has a high slew rate.

As mentioned in subsection 2.3.1, a larger star tracker design leads to a better performing sensor. Ball Aerospace's CT-2020 confirms this as it is by far the largest and most power consuming star tracker on the list. Its larger size allows for a larger baffle to block out more stray light and allows for a larger aperture and imaging sensor for more precise measurements. The 3-sigma accuracy of the CT-2020 is 1.5", which is an accuracy that current CubeSat mission are not necessarily aiming for. Dedicated CubeSat star trackers, such as the CubeStar from CubeSpace, show that miniaturizing the system still provides enough accuracy for CubeSat missions with high accuracy requirements. Therefore, the accuracy of a star tracker is not likely to be the most limiting factor of the design.

### 2.3.3. Limitations

While star trackers offer the best performance out of the currently available attitude determination sensors, they have several limitations that make them less suitable for CubeSats or PocketQubes. The limitations mentioned in this section need to be improved in order to make star trackers a viable choice for upcoming missions.

### 2.3.3.1 Power consumption

The main priority for new CubeSats star tracker designs would be to reduce their power consumption. Even some of the smallest and most efficient star trackers currently available consumes more than 250 [mW] at its peak. Considering that the total power consumption of a 1U CubeSat is around 1-2.5 [W] and 7-20 [W] for a 3U CubeSat, this makes star trackers take up a lot of the power budget [4]. Additionally, some satellites require the use of multiple star trackers for accurate attitude determination.

Most power is consumed in the processing of images. Performing the algorithms to extract attitude information from the images is an intensive process that requires a fair amount of computational power. New algorithms that are more efficient can reduce the power consumption drastically and improve the speed of the star tracker. Next to these improvements, the space industry is getting access to more powerful and more efficient hardware that would make image processing easier in the future. New star tracker designs could utilize these techniques in order to make them better suited for CubeSat and potentially PocketQube missions.

### 2.3.3.2 Size and baffle dimensions

Although the size of star trackers has reduced in recent times, they still take up too much space to be installed on PocketQubes. It is possible to install star trackers onto a larger CubeSat of several units, but there will be little volume left for other subsystems. Therefore, the size of star trackers needs to be reduced further, but without compromising their performance.

Unfortunately, the performance of star trackers is directly linked to its size. This has been explained in detail in subsection 2.3.1. Liu et al. developed a new PCB layout that surrounds the imaging sensor, which allowed for a more compact design. Then, they used a deployable baffle to maintain high performance in orbit, while keeping the size of the star tracker small during launch. These two improvements can be incorporated in future star tracker designs, although it is uncertain whether a deployable baffle is required for the accuracy requirements of CubeSat and PocketQube missions.

### 2.3.3.3 Tumbling performance

Finally, another drawback of star trackers is that they lose accuracy or, in the worst case, become inoperable when the spacecraft is tumbling. The rotational motion of the spacecraft makes the images blurry, which makes it difficult for the algorithms to identify stars and star patterns. This makes that star trackers cannot be used independently on spacecraft, so they are used in combination with other ADCS technologies.

Researchers have tried to tackle this issue by placing the star tracker on a stabilized platform. While this gives an improvement, these designs are often complex, heavy and large, which makes this solution unsuitable for CubeSats or smaller satellites [25]. Several filtering techniques have been applied, such as an EKF by Xing et al. [2]. One of the most promising software techniques was the use of attitude-correlated frames by Ma et al. [25]. The more frames are used in the algorithm, the more noise can be filtered out and the accuracy can be increased. Such software implementations can improve the performance of a small star tracker in dynamic conditions substantially, provided that enough computational power and electric power is available.

## 2.4. Attitude determination techniques

Over the course of more than sixty years of spaceflight, several technologies and techniques have been derived to accurately determine the attitude of spacecraft. Sun sensors and star trackers have already been explained in section 2.2 and section 2.3. Among other sensors are Earth horizon sensors, magnetometers and gyroscopes. Each of these has their own method, advantages and drawbacks, which will be presented in the underlying sections.

### 2.4.1. Earth horizon sensors

Satellite missions close to Earth can utilise Earth horizon sensors. These sensors try to find the centre of the Earth by observing its infrared radiation (IR). The sensor can identify the curvature of the Earth against the cold background of space, from which the centre of the Earth can be approximated [26]. The spacecraft then uses this information to derive its pointing direction [27]. The accuracy of these sensors is typically below  $0.1^\circ$  and they work best when in a circular orbit around the Earth and when the spacecraft has to monitor the Earth directly [2]. This, together with the low costs, low complexity and small size, has made Earth horizon sensors a popular choice for small spacecraft missions in LEO and GEO.

But these sensors have their limitations. They are only able to provide attitude determination in the pitch- and roll-axis, which means that they have to be used in combination with other sensor types to obtain the yaw-axis [26]. Then, the accuracy of the sensors improve with an increasing orbital altitude. The difference in accuracy between LEO and GEO is a whole order of magnitude [2]. In addition, non-circular orbits will lower the sensor's performance. Similarly, extra inaccuracies are introduced by the Earth itself, which is not perfectly round either [2]. These drawbacks limit the versatility of the Earth horizon sensor to specific orbits.

### 2.4.2. Magnetometers

Magnetometers make use of the Earth magnetic field to determine the pointing direction of a spacecraft. Accurate models of the Earth magnetic field are readily available and with them an estimation of the magnitude and direction of the local field can be constructed [2]. The magnetometers onboard the spacecraft compare their measurements with these models to define its orientation. Typically, these sensors are able to provide information of the spacecraft in 2-axis, but post-processing of sensor data using Extended Kalman Filters (EKF) or Real-Time Sequential Filters (RTSF) can unlock 3-axis attitude determination [28].

Generally, magnetometers tend to be accurate in the order of  $1\text{-}5^\circ$ . When spacecraft do not require advanced ADCS, magnetometers are a good choice. But as soon as a mission requires attitude requirements of  $\leq 1^\circ$ , more accurate sensors need to be selected. They also suffer from magnetic interference of metal components in the spacecraft structure, which disturb the magnetic field [29]. Still, magnetometers remain effective even when tumbling, so they are frequently used in support of more precise systems like star trackers [28].

### 2.4.3. Gyroscopes

Another method of monitoring a spacecraft's orientation and angular velocity is through the use of gyroscopes. These wheels or disks are free to rotate independently from the rest of the spacecraft, which can be used to derive the current orientation or rotation rates. Gyroscopes have been proven to be exceptionally useful in eclipse and tumbling situations, for instance after separation of the spacecraft with the launch vehicle [2].

A major drawback of gyroscopes is that without proper calibration, the sensors will start to experience drift over the course of the mission [30]. Therefore, gyroscopes are seldom used individually on spacecraft and instead are used in conjunction with other attitude determination techniques. Furthermore, with spacecraft becoming smaller and smaller, it is being investigated whether gyroscopes can be removed from CubeSats and similar missions to save space and power [31].

## 2.5. Knowledge gap

The previous sections have shown how mature attitude determination technology is. However, the rise of small satellites asks for further improvements into the miniaturization of sensors. This section will highlight aspects of sensor designs that could be worth investigating.

### 2.5.1. Combined star tracker and Sun sensor

Both a star tracker and a Sun sensor can utilize a CMOS imaging sensor. This means that there is a possibility to use the same imaging sensor as a star tracker and a Sun sensor in the same design. This would make the sensor multi-functional and allows for operation under a variety of conditions. The star tracker can be used in eclipse conditions and provide high accuracy, while the Sun sensor can work in daylight conditions with medium accuracy. If there can be easily switched between operational modes, depending on the conditions, then the sensor could take up less volume than a combination of stand-alone Sun sensors and star trackers with the same capabilities. This could be a promising development for small satellites.

Designing such a sensor would result in a compromised sensor that fits in between a star tracker and a Sun sensor. Star trackers often offer high accuracy, while Sun sensors provide medium accuracy. Star trackers often have a narrow FOV, while Sun sensors have a wide FOV. Therefore, in a potential sensor design the star tracker mode is likely to suffer from stray light entering the sensor, while the Sun sensor mode is suffering from a reduced FOV. Designing a sensor with a variable diaphragm could be a solution, but adjustable parts in space will add design complexity and decrease reliability. Any misalignments in the diaphragm could result in a reduction of the sensor's accuracy. It should be investigated whether a compromised design with a fixed diaphragm or aperture can work as 2-in-1 attitude sensor. Moreover, it is unknown whether such a combined design could decrease the power consumption of the attitude determination system, since CMOS sensors tend to consume a significant amount of power.

### 2.5.2. Combined Sun and Earth horizon sensor

Section 2.2.7 mentioned that a major limitation of Sun sensors is that they cannot operate in eclipse conditions, as the Sun needs to be in view. Kapás et al. made a prototype sensor that works both as a Sun sensor and as an Earth horizon sensor using thermal imaging sensors, so that the sensor can be used during eclipse. Such a sensor could greatly benefit small satellites as potentially no additional sensors need to be installed to achieve attitude determination throughout the orbit.

However, Takátsky et al. performed simulations on this sensor and discovered that the eclipse performance was not as accurate as desired. Due to gyroscope drift, the error of the sensor was estimated to be as high as  $25^\circ$ . It should be investigated whether this error also exist when a different sensor type is used for cross-calibration, or perhaps none at all. Also, no experimental data of the Earth horizon sensor performance has been created, so a high-altitude balloon flight proposed by Kapás et al. should be carried out to properly validate its design. If the eclipse performance turns out to be significantly more accurate than initially thought, then the 2-in-1 Sun and Earth horizon sensor is a potential candidate for future space missions.

A modification can be made to the design of the combined sensor that makes the sensor operate in a specific IR band. Romijn et al. made a specific sensor that utilizes a chip that picks up UV signals. This way the albedo effect is reduced. However, making such a chip for the IR spectrum has not been explored yet. Still, Romijn et al. suggests that changing the properties of the chip and basing it on silicon could make a chip albedo insensitive. Unfortunately, it is likely that the design of such a chip is beyond the scope of this thesis.

### 2.5.3. Albedo-insensitive Sun sensor

The specific sunlight and albedo IR bands Romijn et al. showed in Figure 2.5 also bring up the idea of using optical filters. An optical filter can be installed in front of a Sun sensor that only lets through light in a specific IR band where albedo is non-existent. This would give better performance when the Earth is in view without consuming additional power. Therefore, this idea can benefit small Sun sensor types.

There are multiple IR bands where albedo does not exist and these should be identified. Then, it should be researched whether an optical filter can be made with the properties to only let through light of that specific wavelength band. A multitude of filters can be used to block wavelengths outside the desired band. However,

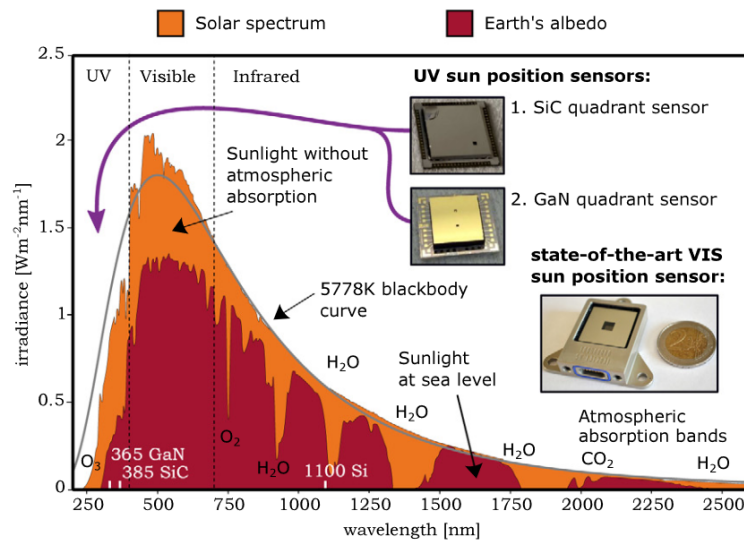


Figure 2.5: Solar irradiance curve for both direct sunlight and albedo [15].

adding optical filters alters the path of the incident sunlight according to Snell's law. A new sensor design should take this into account.

Another type of optical filters are polarizing filters, which are used in sunglasses for instance. These filter unpolarized light and make them polarized light of a particular orientation, which helps to reduce glare from reflections. Potentially, this could be used to reduce the albedo effect in LEO, as the filter could block reflected light from entering the sensor. However, this filter only works in specific orientations and using multiple filters to block out all orientations also blocks out unpolarized light, which would render the sensor useless.

## 2.6. Potential research areas

The problem investigation and literature study have led to three potential research areas. These include using optical filters to eliminate albedo, a combined Sun and Earth horizon sensor and a combined star tracker and Sun sensor. The rationale behind selecting one of these topics over the others will be presented in this section.

First of all, the use of optical filters to eliminate albedo effects in Sun sensors was considered. The idea is to use a COTS Sun sensor and install an optical filter in front of it. This passive system could improve the accuracy of the Sun sensor when it is subjected to albedo without consuming additional power. Such a system can be tested with a simple setup and is achievable in the time frame of the thesis. However, it is unknown what the potential of such a filter actually is. It could make the sensor better resistant to albedo, but there exist other hardware and software solutions that already do this. A filter would not make the sensor much more versatile compared to currently available sensors, and increasing the versatility was the main goal of the thesis. Therefore, it was decided not to proceed with researching optical filters.

The two research areas left were the following: to investigate whether a star tracker and Sun sensor can be combined into one sensor, or to investigate whether a Sun sensor and an Earth horizon sensor can be combined. Both topics are complex and require the development and testing of two sensors in one, which makes for longer development times. The end product in both researches would be to design a proof-of-concept that shows that a combined sensor is possible on small satellites. A test setup needs to be created to test all sensor modes and this should be possible for the Sun sensor using the available resources. However, testing the Earth horizon sensor either requires a high altitude balloon test, or a dedicated test setup that mimics the IR radiation of the Earth. Such a setup was under construction at the Delft University of Technology, but it has not been completed yet. Similarly, the star tracker requires a test under a night sky for validation, but Delft likely has too much light pollution to see enough stars. As a solution, the sensor can be tested in

a different part of The Netherlands where more stars are visible. Else, a dedicated test setup can be made where a night sky is simulated using sharp LCD panels.

Both sensors would be more versatile than existing sensors, as in both cases the sensors can be used in eclipse and in direct sunlight. Earth horizon sensors and star trackers can be used when the Sun is not in view. This also means that the sensors that have the Sun in view can use the Sun sensor mode, while those in shadow can switch to the other mode. Potentially, these measurements can be combined to achieve an even better attitude accuracy, or the total amount of sensors can be reduced. Moreover, a 2-in-1 sensor improves the tumbling accuracy of the attitude determination system compared to a star tracker-only system. However, the performance of Earth horizon sensors is dependent on the orbit, which ideally is circular and in a high orbit, as stated in subsection 2.4.1. Star trackers lack this dependency and are more accurate. Furthermore, star trackers operate in the visual light spectrum and can be configured to use AI models for attitude determination based on geo-detection. This would make it a 3-in-1 sensor, but this reserved for future research. All in all, the 2-in-1 star tracker and Sun sensor has more potential in terms of performance and applicability than the Sun sensor and Earth horizon sensor.

The higher potential, increase in versatility and relative ease of testing has led to the selection of the combined star tracker and Sun sensor and for the research topic of this thesis. A detailed research question and research plan will be explained in chapter 3.

# Research Plan

In the previous chapter the problem was investigated and several research areas were identified. There is a need to design an optical attitude sensor that is more versatile than current designs fit for small satellite platforms, like CubeSats. It was decided to investigate whether combining a star tracker and Sun sensor into one sensor would improve the versatility of attitude sensors. This chapter presents a research plan in order to effectively investigate that option.

This chapter is structured in the following way: First, the research question is presented in section 3.1, together with a motivation behind this question. Second, section 3.2 will explain the research steps that will be taken throughout the thesis. Third, potential roadblocks in the research methodology will be discussed and solutions to them will be given in section 3.3. Finally, a planning for the next phases of the thesis will be presented in section 3.4.

## 3.1. Research question and hypothesis

Combining a Sun sensor and star tracker into one has multiple benefits. The total amount of attitude determination sensors on the spacecraft can be reduced, which lowers the volume required and power consumed. Also, the sensor becomes operational in both sunlight and eclipse by switching between modes. A 2-in-1 sensor is likely to have a compromised design with less performance than two individual sensors. However, if a design can be made that fits onto small satellites, such as CubeSats and PocketQubes, with performance that competes with high quality Sun sensors, then this design has the potential to improve the overall capabilities of these spacecraft. The reason being that the spacecraft would require fewer sensors to achieve the same attitude determination performance. Therefore, the research question was formulated in the following way:

**Research question:** *How do the performance and technical budgets of a combined star tracker and Sun sensor for small satellite form factors compare to a typical combination of individual star trackers and Sun sensors on a system level?*

As mentioned in section 2.5, some types of Sun sensors use CMOS imaging sensors just like star trackers. Finding a suitable commercial-off-the-shelves CMOS camera and turning it into a star tracker and Sun sensor could be a way to make a combined sensor design that is equal in performance, but has a smaller technical budget than a combination of multiple sensors. This would be a versatile attitude sensor that can be used on small satellite space missions. Therefore, the hypothesis can be described as:

**Hypothesis:** *A single COTS CMOS imaging sensor can function as both a star tracker and Sun sensor; compared with the currently employed combinations of sensors used in three-axis attitude determination, this new configuration could achieve a similar target performance and smaller technical budgets on a system level.*

## 3.2. Methodology

Figure 3.1 shows the activities that will be carried out in this thesis. These activities are focused on the design and testing of the combined attitude sensor. Analysis and reporting of the tests is done after these stages. Each activity is explained in the following paragraphs.

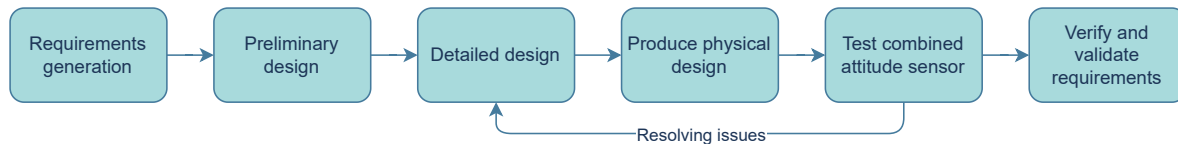


**Figure 3.1:** A road map of the different design phases in this thesis.

The first step is to define a set of requirements to which the final combined sensor design needs to adhere. These requirements will be about the technical parameters of the design that are most critical when the sensor will be used on CubeSats and PocketQubes. Some of these parameters are its size, power consumption and accuracy in both modes. In parallel to this, it should be decided which design philosophy will be selected: whether to focus on high accuracy, small form factor or something else. Of course, this design philosophy must be realistic and achievable in the time frame of the thesis.

With the requirements set, a preliminary design of the combined attitude sensor can be created. This means that an active pixel sensor should be acquired that is suitable to use as a star tracker and Sun sensor and fits onto CubeSats and PocketQubes. For example, it should have a size that is below the maximum allowed sensor size from the requirements. Furthermore, the sensor should have a low power consumption. However, since the design created in this thesis will be a prototype, the sensor does not necessarily need to meet the hard power consumption requirement immediately. Therefore, the requirements will be split up into requirements for an flight-ready design and requirements for a prototype. Once the prototype shows that a combined sensor is feasible, then the power consumption of the flight-ready sensor is likely to be reduced through more dedicated PCB's and software algorithms. Moreover, technological developments in the electronics sector will improve the efficiency of sensors, microprocessors and other electronics in the upcoming decade. Thus, if current technology is not powerful enough to make the combined sensor compete with individual sensors, then new technologies could make a difference in the future.

When the exact specifications of the sensor module are known, the hardware can be analysed and its performance can be predicted. Software settings can be investigated so that the most performance can be extracted from the sensor. Doing the performance calculations will provide predictions on the sensor's FOV, accuracy and power consumption. The impact of an extra baffle will also be calculated. All these calculations will be linked together in Excel, which allows for quick design iterations in a complex design problem. Once the preliminary design has been created, a more detailed design can be constructed. Here, sensor modes can be selected that will be used in testing and a baffle can be designed using CAD modelling software.

The next step would be to realise the design into a prototype. This is mostly the creation of software to control the sensor during testing. Since this attitude sensor is a combined design, the sensor should be able to operate in both sensing modes. Thus, the sensor requires software for both. Due to time constraints, switching between modes will be done manually between tests. The sensor can be linked to a compatible circuit board using a breadboard and cables. Other hardware components can be 3D printed if they are just supporting structure. If more precise components need to be manufactured, then this can be done from other materials, such as aluminium. Creating these should be possible at the TU Delft.

Once the design is complete, the prototype will undergo tests to validate its performance as a Sun sensor and star tracker. It can be placed in a test setup where sunlight is simulated using a laser or a powerful lamp [17]. In this setup, the incidence angle of the light can be selected such that the performance of the Sun sensor across its FOV can be determined. Such a setup can be created in a small room with inexpensive materials. Testing the star tracker mode might be more complex. The sensor can be brought to a place where there is little light pollution and monitor the stars at night. However, this is impractical, since The Netherlands generally has severe light pollution. Furthermore, being far away from Delft without the proper tools makes

troubleshooting more difficult. Luckily, some researchers are trying to replicate the night sky using LED or LCD panels. It should be researched if this is a valid method for validating a star tracker's design, but if it is, it could be a good alternative for this thesis.

After the testing phase, the final steps are to compare the design and performance of the sensor to the requirements set at the start. Ideally, all requirements are met at the end of the thesis. Recommendations for future research and designs need to be explored. If time allows it, another design iteration can be made to improve the combined attitude sensor.

### 3.3. Anticipated challenges

This thesis aims to solve a complex design problem that will bring forth challenges in the design and testing of the sensor. Identifying these challenges early allows for the creation of mitigation strategies to limit their impact on the thesis. This section will explain the most important challenges.

First, the design of a 2-in-1 sensor is in itself complex. Whereas typical studies only develop part of a sensor type, this thesis aims to develop two at the same time. A combined design will be made and each sensor mode needs to be tested individually. Obviously, this is going to impact the duration of the study if not managed correctly. But since this thesis aims to develop a prototype combined sensor, the performance and resource budgets do not need to be on the same level as those from direct competitors yet. Then, future studies can improve the design further once the combined sensor concept has been proven to work. The focus on proof of concept will make it easier to achieve a satisfactory design in a limited time frame.

Second, the design will likely not incorporate advanced post-processing techniques that reduce the sensor's power consumption. For instance, some star trackers use filtering techniques to efficiently search through their star database. These techniques are too advanced for this prototype, given the amount of time available and the scope of the thesis, but can be added in future studies. The focus of this thesis is mostly on confirming if the design concept is feasible and little on creating smart sensor algorithms. It does mean that it is likely that the prototype will be less refined than its competitors and that some requirements are more difficult to be met. Therefore, as mentioned in section 3.2, the requirement for power consumption, will be relaxed. Once the prototype has been constructed and it offers great potential for the small satellite market, then the software can be increased to achieve an even more competitive design.

Third, both sensor modes ideally have their own hardware layout. A Sun sensor works best with a narrow pin hole above its CMOS chip, while a star tracker often requires a wider aperture. Interchanging the hardware while in space and thereby introducing moving parts to the design has been proven to be difficult in the past. Such mechanical systems are more prone to failures and the system needs to be extremely precise in order to maintain good optical accuracy on the sensor. Part of the preliminary design phase should be spend investigating whether such a system is necessary, feasible and if it offers the desired performance. Another option would be to have a fixed aperture design, but this would mean the overall performance of the sensor modes will be compromised.

### 3.4. Planning

A planning was created to act as a guideline during this thesis. The thesis topic is complex and requires two sensors to be designed at the same time. An overview of the time allocated per thesis phase can be seen in Table 3.1. Furthermore, the planning was turned into a Gantt chart, which can be seen in Figure A.1 in Appendix A.

Initially, the thesis began with literature study and research plan, which lasted 4 weeks and 3 weeks respectively. Then, 2 weeks will be spend on generating requirements for the design of the combined sensor. Completing these marks the end of the starting phase of the thesis, and the design of the sensor will start.

**Table 3.1:** Time allocated for different thesis phases.

Phase	Time allocated
Literature Study	4 weeks
Research Plan	3 weeks
Requirements Generation	2 weeks
Preliminary Design	4 weeks
Detailed Design	4 weeks
Manufacturing	9 weeks
Testing	6 weeks
Verification and Validation	1 week
Analysis, Comparison and Conclusions	2 weeks
Finalizing Thesis	2 weeks

The preliminary design phase lasts around 4 weeks. Here, a suitable CMOS sensor will be selected and ordered, if required. The delivery time is not taken into account in the planning, but the sensor should be available before the start of the manufacturing phase. Once the sensor has been selected, other design parameters can be defined, such as the baffle size. At the same time, a testing location should be found, together with the equipment required for the sensor. Near the end of the preliminary design phase the detailed design will start and it will last another 4 weeks. In this phase, the preliminary design is further explored and a more complete sensor design is created. In case it is required, 3D drawings of individual parts will be generated in this phase.

Then, the sensor is manufactured over the course of 9 weeks. First, the active pixel sensor will be linked to a controller board, such as a Raspberry Pi, and initial testing starts. This provides insight into how the sensor should be configured and that helps in creating the sensor's software. The software for the Sun sensor will be created first, as this is in theory simpler. The knowledge gained here will help in creating the star tracker's software. Both of these software programs should be created in 4 weeks each, of which one week overlaps. The final week is spend integrating the software and hardware together into a test setup.

The testing phase will be 6 weeks long with each individual sensor mode being tested for 3 weeks. This should be sufficient time to test the sensors accuracy, performance across its FOV and other characteristics. Thereafter, 1 week will be spend on verification and validation checks on the design. Two more weeks will be dedicated to analysing the results, comparing the design to individual sensors and writing down conclusions. Although, part of these tasks will already start during the testing phase. The last 2 weeks are for finalizing the thesis.

# Preliminary Design Phase

Now that the research plan has been created, the next step is to make requirements for the combined sensor and start with the preliminary design. For this, the use case of the sensor needs to be explored first, so that it is understood how the sensor can be used effectively in space. In this use case, deficiencies and advantages of the sensor can be identified, which can be used to narrow down the requirements. Once the requirements have been defined, the preliminary design of the sensor can start.

This chapter starts by explaining the design concept of the combined sensor and how it will be implemented in a satellite. This will be covered in section 4.1. Subsequently, the requirements for the overall sensor design are presented in section 4.2. Then, a CMOS sensor is selected that fits the requirements and can be used in the prototype. The selection of this sensor will be explained in section 4.3. Finally, the performance of the chosen CMOS sensor is predicted in terms of star visibility, stray light impact and power consumption. This can be read in section 4.4.

## 4.1. Design concept

Before the requirements are presented, the design concept will be explained in more detail. The idea is that a total of three combined sensors will substitute for two star trackers and four to six Sun sensors. This has implications on the size and power budgets, but also in terms of performance and viewing angles. An overview of a configuration of combined sensors on a 3U CubeSat is displayed in Figure 4.1.

Three combined sensors are installed. One is placed at the very top of the CubeSat, where often payload instruments are positioned as well. The small size of the combined sensor should allow it to be placed next to payload instruments on that surface. The other two sensors are placed on the sides, if possible between solar panels. Again, the size of the sensor should be small enough that it is versatile in its placement and that it can be installed in the empty space between solar panels, as is being done with several Sun sensors currently. However, only three viewing directions are covered out of the six, whereas six Sun sensors are able to cover all six viewing directions. Also, the FOV of the combined sensor is likely to be less than typical Sun sensors, which means that the total coverage in the sky is limited. Therefore, using just three combined sensors will cause blind spots in the sky where none of the sensors can see the Sun.

Those blind spots have serious implications on the usability of the sensors. When the spacecraft is slewing fast the star tracker mode is not accurate any more, so the Sun sensor mode needs to provide the attitude. However, if the Sun is in one of the blind spots, then the combined sensor cannot determine the current attitude of the spacecraft. It would have to wait for the Sun to arrive back in view, but based on the rotation of the spacecraft, and whether the spacecraft is in eclipse or not, it can take minutes, if not hours, for these 'lucky-shots' to arrive.

One solution to this is to increase the number of combined sensors installed on the spacecraft. However, this would defeat the purpose of this sensor, which was to reduce the number of sensors installed on a spacecraft. When the amount of combined sensors is increased it becomes more beneficial from a technical budget to use separate Sun sensors and star trackers and place them in all viewing directions. The individual Sun sensors also have a higher FOV than the combined sensor, which ensures that they can see almost a full 360° view of the sky. Another solution would be to use a different sensor that reduces the tumbling and brings the Sun

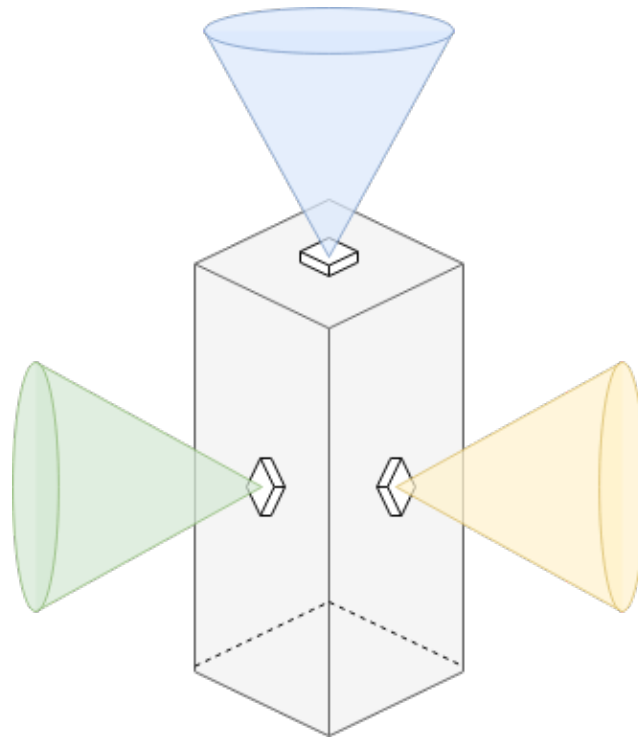


**Figure 4.1:** Placement and viewing angles of three combined sensors on a 3U CubeSat.

in view, after which the combined sensor can take over. Potential candidates are coarse magnetometers or gyroscopes that are very small in their design and act as backup sensors. Still, the final selection depends on the overall design of the spacecraft and the available budgets. A third solution is to aim for a relatively wide combined sensor FOV to reduce the size of the blind spots. But, this might reduce the accuracy of the star tracker mode. Luckily, the blind spots are less of a problem when the spacecraft is not rotating, since then there should be at least one sensor looking at the stars or at the Sun.

## 4.2. Requirements

The hypothesis of this thesis is that a COTS CMOS sensor can combine the function of a star tracker and Sun sensor in one design, while having smaller technical budgets but similar performance on a system level than that of a typical combination of attitude sensors. A combined sensor design leads to a reduction of the number of sensor modules that need to be installed on a spacecraft. Therefore, the focus of the design lies on reducing the technical budgets of the sensor, rather than improving the performance. This is reflected in the requirements, which are stronger on size and power consumption than on accuracy.

Moreover, the requirements were split up in those for a flight-ready sensor design and those for the prototype. The prototype will be less refined in several aspects as components like PCBs have not been created for this purpose in particular. Therefore, the requirements for the prototype are relaxed.

### 4.2.1. Flight-ready design

Table 4.1 shows the requirements for the flight-ready design. This design should compete with a combination of star trackers and Sun sensors on a system level. The requirements have been given the codes *CVAS-FLR-XX*. Here, *CVAS* stands for Combined Versatile Attitude Sensor. *FLR* is a tag to indicate that this is a requirement corresponding to the flight-ready sensor design and it is followed by *XX*, which represents the requirement number.

**Table 4.1:** Requirement list for the flight-ready combined versatile attitude sensor.

Requirement code	Description
CVAS-FLR-01	The combined versatile attitude sensor shall be able to determine the position vector of the Sun.
CVAS-FLR-02	The combined versatile attitude sensor shall be able to identify star patterns.
CVAS-FLR-03	The combined versatile attitude sensor shall be able to switch between Sun sensor and star tracker mode.
CVAS-FLR-04	The combined versatile attitude sensor shall provide 1.0 degree accuracy during slew manoeuvres above 0.2 degree/s.
CVAS-FLR-05	The combined versatile attitude sensor shall provide 0.2 degree accuracy when stable pointing and during slew manoeuvres below 0.2 degree/s.
CVAS-FLR-06	The combined versatile attitude sensor shall have a Sun sensor accuracy of at least 1.0 degree with 1-sigma confidence.
CVAS-FLR-07	The combined versatile attitude sensor shall have a star tracker accuracy of at least 0.2 degree with 1-sigma confidence.
CVAS-FLR-08	The combined versatile attitude sensor shall have a maximum size of 20x20x10 mm.
CVAS-FLR-09	The combined versatile attitude sensor shall have an average power consumption below 70 mW.
CVAS-FLR-10	The combined versatile attitude sensor shall have an update rate of at least 10 Hz in slew manoeuvres above 0.2 degree/s.
CVAS-FLR-11	The combined versatile attitude sensor shall have an update rate of at least 2 Hz in stable pointing and slew manoeuvres below 0.2 degree/s.

First, requirement *CVAS-FLR-01* was defined to indicate that the sensor should function as a Sun sensor. Determining the position vector of the Sun is what allows a Sun sensor to derive the attitude of the spacecraft. Similarly, requirement *CVAS-FLR-02* describes that the sensor should be able to function as a star tracker. The sensor should identify star patterns so that these can be compared to a star database. The onboard computer can then identify the orientation of the satellite from the matching stars. Then, requirement *CVAS-FLR-03* follows from the concept of the combined sensor. The sensor should be able to switch to the mode that is ideal for the current light conditions. If the sensor is in sunlight, then stars are not visible, so the sensor needs to select the Sun sensor mode. And vice versa in case the Sun is not in view. While the sensor needs to be able to switch sensor modes, it is not necessary to have an automatic system in place for this prototype. It suffices if the sensor mode is selected manually in between tests. Future designs must incorporate a mode selection algorithm for it to be used in an actual space mission.

The accuracy requirements were split up into two pointing modes. *CVAS-FLR-04* states that the combined sensor should have an accuracy of  $1.0^\circ$  while performing slew manoeuvres below  $0.2^\circ/\text{s}$ . Requirement *CVAS-FLR-05* explains the accuracy when stable pointing or during a slew manoeuvre below  $0.2^\circ/\text{s}$ , which shall be  $0.2^\circ$ . Sun sensors and star trackers can be more accurate, but the performance of the combined sensor will be sacrificed for better technical budgets. Still, with these accuracy requirements the system should be capable of offering performance on-par with high accuracy Sun sensors, while also providing three-axis attitude determination. In addition, the combined sensor can function in both sunlight and eclipse.

The accuracy requirements of the individual sensor modes were established from the previous two requirements. Slew manoeuvres and coarse pointing will be done by the Sun sensor mode, while maintaining stability and stable pointing will be done by the star tracker. Hence, *CVAS-FLR-06* states that the Sun sensor mode shall have a 1-sigma accuracy of  $1.0^\circ$ , while *CVAS-FLR-07* states the star tracker mode shall have a 1-sigma accuracy of  $0.2^\circ$ .

Then, a number of requirements follow that highlight the technical budget of the sensor. Again, the sensor should compete with star trackers and Sun sensors, so its size and power budget lie between typical values for these sensors. *CVAS-FLR-08* states that the sensor shall have a maximum size of 20x20x10 [mm]. In terms of the length and width, this lies between the size of a high quality Sun sensor, such as the Needronix Eagle of 15x15x5 [mm], and the smallest star trackers, which are around 25x25x40 [mm]. The maximum height

of 10 [mm] was determined in a different way. In order to make the combined sensor attractive for small satellites platforms, it should be kept thin enough to fit between a CubeSat's outer wall and inner components. CubeSats feature a rail on their edges which provides structural integrity and allows for easy integration with a deployment mechanism [32]. These rails can be seen in Figure 4.2 and they create a space of 8.5 [mm] that can be utilized by sensors, which the Needronix Eagle already does. If the CVAS is also thin, then it can fit in this space and it would make the sensor highly versatile in terms of placement. Due to margins in the internal layout of the satellite, the height available is close to 10 [mm].

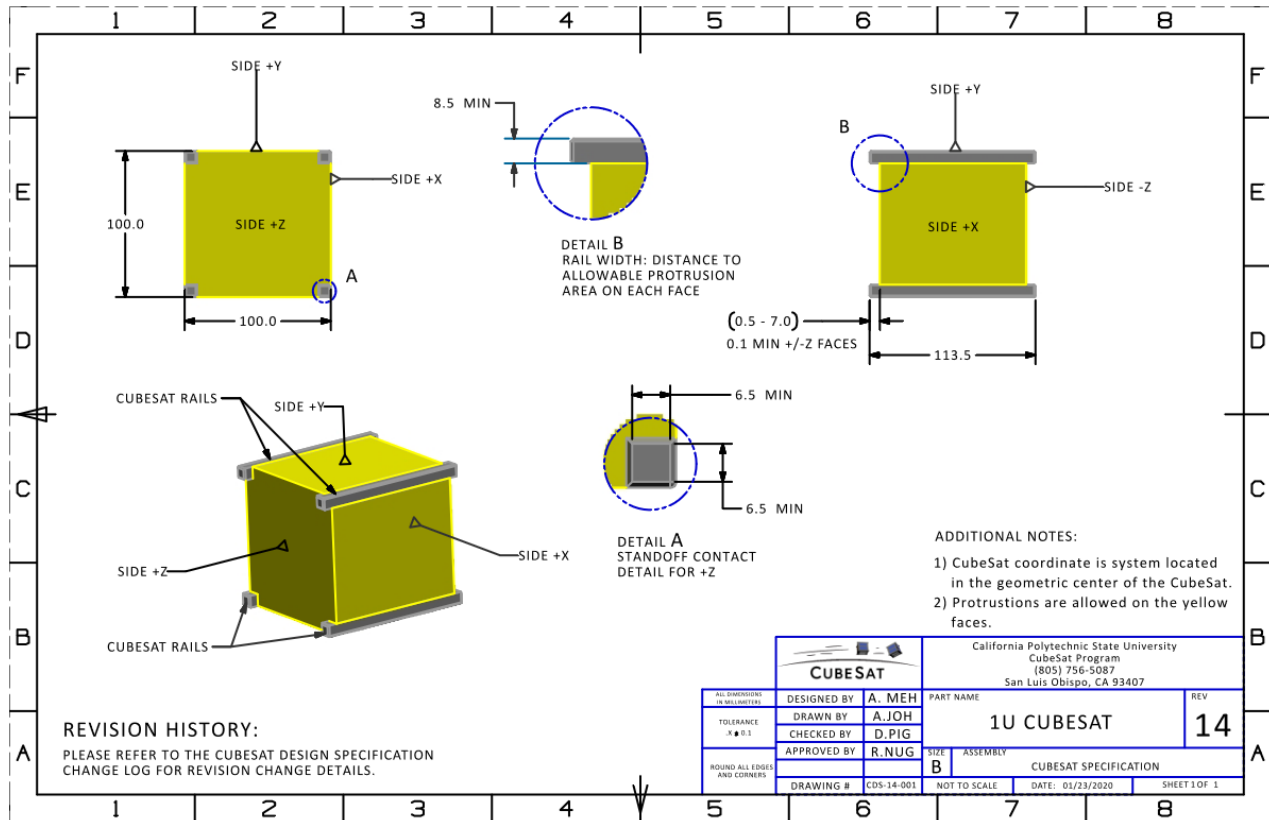


Figure 4.2: Technical drawing of a 1U CubeSat with details on the rail system [32].

The rationale behind requirement CVAS-FLR-09 is that the power consumption of the combined sensor should be a considerable improvement over the power consumption of popular combinations of attitude sensors. In case a mission has strict attitude requirements, then spacecraft often require two star trackers for high accuracy pointing and four to six Sun sensors to achieve full-sky coverage. Depending on the power consumption of specific star trackers and Sun sensors highlighted in Table 2.2 and Table 2.3, the total power consumption varies between 420 and 1500 [mW]. From the combined sensor's design concept, ideally only three CVASs are required to provide the same capabilities, while only consuming half of the power. This large decrement in power consumption helps to offset the projected loss of accuracy that originates from making a smaller sensor. Following these steps, the power consumption target for a single CVAS is 70 [mW]. It is important to understand that the power consumption of a sensor consists of both a camera and a computer processing the images. In case a satellite uses a central computing system, then the power consumption of the camera alone can be 70 [mW]. Otherwise, the sensor has a build-in computer chip that performs the analysis.

The final requirements, CVAS-FLR-10 and CVAS-FLR-11 describe the update rate of the combined versatile attitude sensor. The Sun sensor mode will be activated when the spacecraft is tumbling, which has been defined as uncontrolled slewing above  $0.2^\circ/s$ . The update rate of the Sun sensor mode should be high enough so that the accuracy of the sensor is better than the change in attitude. An update rate of at least 10 [Hz] will make sure that the sensor can provide accurate attitude information when rotating close to  $10^\circ/s$ . The star tracker mode will do the same but for speeds up to  $0.2^\circ/s$ . Here, 2 [Hz] shall be sufficient for stable pointing.

### 4.2.2. Prototype

**Table 4.2:** Requirement list for the prototype combined versatile attitude sensor.

Requirement code	Description
CVAS-PROTO-01	The prototype combined versatile attitude sensor shall be able to determine the position vector of the Sun.
CVAS-PROTO-02	The prototype combined versatile attitude sensor shall be able to identify star patterns.
CVAS-PROTO-03	The prototype combined versatile attitude sensor shall be able to switch between Sun sensor and star tracker mode.
CVAS-PROTO-04	The prototype combined versatile attitude sensor shall provide 5.0 degree accuracy during slew manoeuvres above 0.2 degree/s.
CVAS-PROTO-05	The prototype combined versatile attitude sensor shall provide 2.0 degree accuracy when stable pointing and during slew manoeuvres below 0.2 degree/s.
CVAS-PROTO-06	The prototype combined versatile attitude sensor shall have a Sun sensor accuracy of at least 5.0 degree with 1-sigma confidence.
CVAS-PROTO-07	The prototype combined versatile attitude sensor shall have a star tracker accuracy of at least 2.0 degree with 1-sigma confidence.
CVAS-PROTO-08	The prototype combined versatile attitude sensor shall have an update rate of at least 5 Hz in slew manoeuvres above 0.2 degree/s.
CVAS-PROTO-09	The prototype combined versatile attitude sensor shall have an update rate of at least 1 Hz in stable pointing and slew manoeuvres below 0.2 degree/s.
CVAS-PROTO-10	The prototype combined versatile attitude sensor shall be compatible with either Arduino, Raspberry Pi or PC.

The goal of the prototype is to show a proof-of-concept of a combined sensor that comes close to the target performance established in subsection 4.2.1. The prototype will be designed with limited financial resources, manufacturing techniques and testing facilities, so it will struggle to achieve the same performance and technical budgets as the flight-ready design. Therefore, the requirements are relaxed. An overview of the requirements is given in Table 4.2. The requirement codes are of the form *CVAS-PROTO-XX*, where *PROTO* indicates that this is a requirement specific to the combined sensor prototype.

Requirements *CVAS-PROTO-01*, *CVAS-PROTO-02* and *CVAS-PROTO-03* remain unchanged from the flight-ready sensor design as these define the key functions of the sensor. However, the accuracy requirements *CVAS-PROTO-04* and *CVAS-PROTO-05* are lowered by a factor of 5 and a factor 10 respectively. Instead of 1.0°, the Sun sensor mode must now be at least 5.0° accurate, while the star tracker mode must be at least 2.0° accurate instead of 0.2°. Creating a prototype in a limited amount of time without proper development of post-processing tools will lead to an un-optimized design. In addition, with the likelihood of inaccuracies in the test setup and the sensor being sensitive to temperature, it is expected that the prototype cannot achieve the target performance as defined in requirements *CVAS-FLR-04* and *CVAS-FLR-05*. The new accuracy targets should be obtainable within the span of this thesis and they should demonstrate that the concept can compete with other ADCS systems once the design is more refined.

Next, the size and power requirements *CVAS-FLR-08* and *CVAS-FLR-09* were dropped. Again, the resources available for this project are limited, so the layout of the sensor and power consumption will not be optimised. An off-the-shelves sensor will be used, but this restricts the mechanical design of the combined sensor since it cannot be easily redesigned. Hence, the size of the prototype sensor will likely not meet the original size requirement. Once more resources are available, the combined sensor can be designed around a dedicated CMOS chip and the design can be made to meet the target size. In addition, a dedicated CMOS chip and efficient post-processing algorithms can bring the power consumption down. Improvements in PCB technology and a dedicated computer chip will also help to reduce the power consumption. Thus, the two requirements were dropped as they are non-critical for the prototype design, considering the available resources. Still, the prototype should show that the flight-ready sensor has the potential to meet the requirements in the future. Therefore, the two requirements will be used as guidelines to the prototype design.

For the same reason, the requirements *CVAS-PROTO-08* and *CVAS-PROTO-09* were reduced by half from 10 [Hz] to 5 [Hz] and from 2 [Hz] to 1 [Hz] respectively. The prototype should be capable of having an update rate of 5 [Hz] in Sun sensor mode and 1 [Hz] for the star tracker mode. Once the hardware and software has been refined, then the update rate can be increased. Finally, *CVAS-PROTO-10* states that the sensor shall be compatible with either Arduino, Raspberry Pi or PC, which allows for easy prototyping. These platforms have been chosen since there exist many cameras for them and proper documentation on hardware and software for these platforms is readily available. The future, flight-ready design is allowed to be based on different hardware and software.

## 4.3. CMOS sensor selection

The requirements established in section 4.2 have set the framework for the design of the combined versatile attitude sensor. The next step is to find a suitable optical module that can be bought off-the-shelves. There exists a wide variety of sensors that have different resolutions, FOV, power consumption and colour settings. A trade off between several candidate sensors will be performed in order to select the one best suited for the combined sensor.

First, subsection 4.3.1 will explain new requirements which the optical module and its active pixel sensor specifically should meet. Then, a trade off is performed in subsection 4.3.2, from which an COTS sensor is selected.

### 4.3.1. Optical module requirements

The flight-ready sensor requirements that were generated in the previous section were used to base the optical module requirements on. These differ from the overall sensor requirements as these focus on the performance and capabilities of the photosensitive element specifically. The list of requirements can be seen in Table 4.3. The code format is *CVAS-OM-XX*, where *OM* highlights that this is a requirements for the COTS Optical Module.

**Table 4.3:** Requirement list for the commercial-off-the-shelves optical module.

Requirement code	Description
CVAS-OM-01	The optical module shall have an active pixel sensor based on CMOS technology.
CVAS-OM-02	The optical module shall be able to operate in the visible light spectrum.
CVAS-OM-03	The optical module shall cover not more than 0.1 degree per pixel.
CVAS-OM-04	The optical module shall have a minimum update rate of 10 Hz.
CVAS-OM-05	The optical module shall have an active pixel sensor with a maximum power consumption of 70 mW.
CVAS-OM-06	The optical module shall have an active pixel sensor that fits in a space with the dimensions 20x20x10 mm.

First, requirement *CVAS-OM-01* states that the sensor shall use CMOS technology. Although Charge Coupled Devices (CCDs) offer low-noise images, CMOS sensors excel in low power consumption and low prices [33]. Also, CMOS technology is improving rapidly, so innovations could improve sensors in the upcoming years. Then, the sensor shall be able to operate in the visible light spectrum, according to *CVAS-OM-02*. The rationale behind this is that stars are most easily detected in the visible light spectrum, since their infrared emissions are negligible so far from Earth.

The next requirements are focused on the accuracy and update rate of the sensor. The sensor should pick up starlight and distinguish two stars from each other. From requirement *CVAS-FLR-05* it follows that the sensor needs to be  $0.2^\circ$  accurate. However, following the Nyquist limit the sensor needs to be twice as accurate as the target accuracy, so  $0.1^\circ$  will be the aim. This is noted in requirement *CVAS-OM-03*. The accuracy per pixel of a COTS optical module can be found by dividing the sensor's FOV by the number of pixels. Regarding

the update rate, the sensor should have a minimum update rate of 10 [Hz], as stated in *CVAS-OM-04*. This also follows directly from the requirements generated in section 4.2.

Although the size and power requirements were dropped for the prototype combined sensor, the optical module does have these requirements in place. The active pixel sensor within the optical module shall not consume more than 70 [mW], according to *CVAS-OM-05*. This is based on requirement *CVAS-FLR-09*. The power consumption of COTS sensor modules could be lower than what is highlighted on their data sheet by selecting a lower update rate and resolution. This way, even sensors that do not meet this requirement initially can still be selected for this thesis. The size requirement *CVAS-OM-06* states that the active pixel sensor specifically can have maximum dimensions of 20x20x10 [mm]. The PCB and housing surrounding this sensor element are not taken into account, as these can be replaced with a design created in the phases after this study.

### 4.3.2. Sensor trade off

An investigation on COTS optical modules was performed in order to find a suitable sensor for the study. The sensors needed to be compatible with Arduino, Raspberry Pi or PC and their specifications should comply with the requirements generated in Table 4.3. Then, a trade off was performed where each sensor was graded on a score from 1 to 5 on five weighted criteria. Here, a score of 1 meant the sensor did not comply with the requirements at all, while a score of 5 meant the sensor complied and did so with a large margin. Moreover, each criterion was weighted on a scale of 1 to 5, with the latter indicating that the criterion is of the highest importance to the sensor design. The outcome of this trade off will be presented in this section.

#### 4.3.2.1 Criteria and rationale

The first criterion is the accuracy of the sensor. This was given a weight of 3 in order to highlight the importance of the sensor being accurate enough to capture stars. The COTS should not cover more than  $0.1^\circ$  per pixel, according to *CVAS-OM-03*. Sensors that are more accurate than this are beneficial, as it means that potentially a lower resolution setting can be used, which reduces power consumption and computational power.

The second criterion is the applicability of the sensor to this specific design problem. Essentially, this criterion encapsulates a combination of platform compatibility, chroma, module size and lens diameter, which are all important considerations in the selection process. Sensors that are compatible with a wide variety of PCBs score high. Also sensors that are monochromatic score high, since these are more sensitive to starlight than colour sensors. A smaller module size makes placement of the sensor more versatile and a smaller lens diameter reduces the risk of burning-in the sensor. In addition, a smaller lens diameter makes the sensor less susceptible to stray light entering the lens, which reduces the need for a long baffle. These design aspects together have received a weight of 5 to highlight their importance.

The power consumption of the sensor was determined to be the second most important criterion after applicability. It was given a weight of 4 since the power consumption needs to be low in order for the combined sensor to be competitive with other sensors on the market. The requirement is very strict, with a maximum power consumption of 70 [mW] allowed. Most sensors fail to meet this power requirement, but through lowering the frame rate and resolution the sensor's power consumption can be decreased. Therefore, the scores for each sensor were based on a combination of standard power consumption and the ability to lower this consumption through selecting different operational modes.

Finally, the update rate is a criterion that follows from *CVAS-OM-04*. The minimum update rate of 10 [Hz] is required for the Sun sensor mode to operate while the spacecraft is tumbling. The criterion has only been given a weight of 1, since having a high accuracy and low power consumption are far more important to the combined sensor design. Still, a sensor with a high update rate gives more leeway for the combined sensor design, like lowering the power consumption. Therefore, sensors with an update rate between 10-29 [Hz] have been given a score of 3, those with 30-59 [Hz] a 4 and a 5 from 60 [Hz] onwards.

### 4.3.2.2 Trade off results

A total of nine COTS optical modules were selected for the trade off. These modules range from low resolution 0.3MP cameras to advanced 12MP cameras. The specifications of the optical modules can be found in Tables 4.4 and 4.5. Here, the modules are listed in order of resolution, from low to high.

An identifier is positioned after the FOV value to indicate whether that value is the diagonal (D) FOV or the horizontal (H) FOV. The power consumption listed is that of the active pixel sensor when under full load. This does not include processing power required by the eventual onboard computer. The update rate corresponds to the value mentioned in the sensor's data sheet when operating at its highest resolution. Often, the update rate can be increased when a lower resolution is selected. Finally, the accuracy is displayed in degree/pixel and is derived from dividing the FOV with the resolution.

The scoring of each module in the trade off can be seen below the specifications. The four criteria are displayed with each of them having a row with a height that represents their weight. For example, the accuracy has a weight of 3 and is therefore 3 times taller than the update rate, which has a weight of 1. In addition, each score was marked with a colour band ranging from red to white to green, which helps to make the scoring more visible. The total score of each optical module, which is a weighted average, can be seen in the final row of the tables.

Two clear winners emerged from the trade off. These are the HM0360 and the OV9281-A, which both scored 4.15 out of 5. Although their scores are similar, they differ in terms of performance and characteristics. The HM0360 is a small, low budget optical module with only a resolution of 640x480 pixels, whereas the OV9281-A is a higher resolution camera with an almost eight times more power consumption. In third place came the OV9281-B, which has similar performance as the OV9281-A, but features a detachable lens. Pictures of the three modules can be seen in Figure 4.3 (a) to (c).

**Table 4.4:** Specifications of commercial-off-the-shelf optical modules and their trade off results. (1/2)

Sensor	OV7675	HM0360	OV9281-A	OV9281-B	OV2640
Company	Arducam	Arducam	Arducam	Arducam	Arducam
Compatibility	Arduino	Raspberry Pi Pico	Raspberry Pi	Raspberry Pi	Arduino / Raspberry Pi
Resolution [pixels]	640x480	640x480	1280x800	1280x800	1600x1200
Chroma	Color	Color / Monochrome	Monochrome	Monochrome	Color
Detachable lens	No	No	No	Yes	Yes
FOV [deg]	63.9 (D)	64 (D)	89.5 (D)	89.5 (D)	60 (H)
Power consumption [mW]	98	20	156	156	140
Update rate [Hz]	15	60	120	120	15
Accuracy [deg/pixel]	0.0799	0.0800	0.0593	0.0593	0.0375
Trade off results					
Accuracy (3)	3	3	4	4	5
Applicability (5)	3	4	5	3	2
Power consumption (4)	3	5	3	3	3
Update rate (1)	3	5	5	5	3
Total	3.00	4.15	4.15	3.38	3.08

**Table 4.5:** Specifications of commercial-off-the-shelf optical modules and their trade off results. (2/2)

Sensor	IMX462	OV5647	OV5642	IMX708
Company	Arducam	Arducam	Arducam	Arducam
Compatibility	Raspberry Pi	Raspberry Pi	Raspberry Pi	Raspberry Pi
Resolution [pixels]	1920x1080	2592x1944	2592x1944	4608x2592
Chroma	Color	Color	Color	Color
Detachable lens	Yes	No	Yes	No
FOV [deg]	141 (H)	54 (H)	60 (H)	66 (H)
Power consumption [mW]	2120-850	500	340	1360
Update rate [Hz]	30	15	15	10
Accuracy [deg/pixel]	0.0734	0.0208	0.0231	0.0143
Trade off results				
Accuracy (3)	4	5	5	5
Applicability (5)	2	4	2	3
Power consumption (4)	1	1	2	1
Update rate (1)	4	3	3	3
Total	2.31	3.23	2.77	2.85

The HM0360 optical module has an excellent power consumption and small size. Its default update rate easily meets the requirements as well. In terms of applicability to the thesis, the sensor has a small lens diameter and can be monochrome. However, the sensor is only compatible with the Raspberry Pi Pico, which has less functionality and processing power than general Raspberry Pi boards. This could hamper the prototype development as this will be done through the Raspberry Pi OS running on the board. Therefore, the optical module scored a 4 out of 5 for applicability. Furthermore, the sensor has a rather low resolution, which leads to the lowest accuracy of the entire selection of models. Luckily, it still meets the requirement. The final score of the HM0360 is a 4.15 out of 5.

The OV9281-A is compatible with all Raspberry Pi boards, has a small size and lens diameter and is monochrome. Thus, in terms of applicability to this thesis, the sensor scores a 5 out of 5. Regarding its accuracy, the optical module has a resolution of 1MP, which makes it significantly more accurate than the HM0360. The update rate is among the highest of all sensors at 120 [Hz], which far exceeds the requirement. This has implications for the power consumption, which will be lower than its average consumption when a slower update rate is selected. Therefore, the ability to still meet the power requirement exists and hence the module was given a score of 3 out of 5 on this criterion.

The optical module in third place is the OV9281-B, which shares the same active pixel sensor as the OV9281-A. The B-variant differs from the other variant due to the fact that it has a detachable lens with an M12 mount. Lenses that are compatible with this mount and sensor can be fitted onto the module in order to adjust its field-of-view. Initially, it was thought that having this option would be beneficial to the design process of the combined versatile attitude sensor, as then an optimum FOV can be selected. However, these lenses significantly increase the size of the lens, which makes the module prone to stray light entering the sensor and a larger chance of damaging the sensor through burn-in. This would require a large baffle to block out the stray light, but that also makes the entire sensor module too large to fit in the space between the wall and the internals of a CubeSat. Although, this was not a priority of the prototype. Still, based on these facts this optical module only scored 3 out of 5 for applicability, which brought its total score to 3.38.

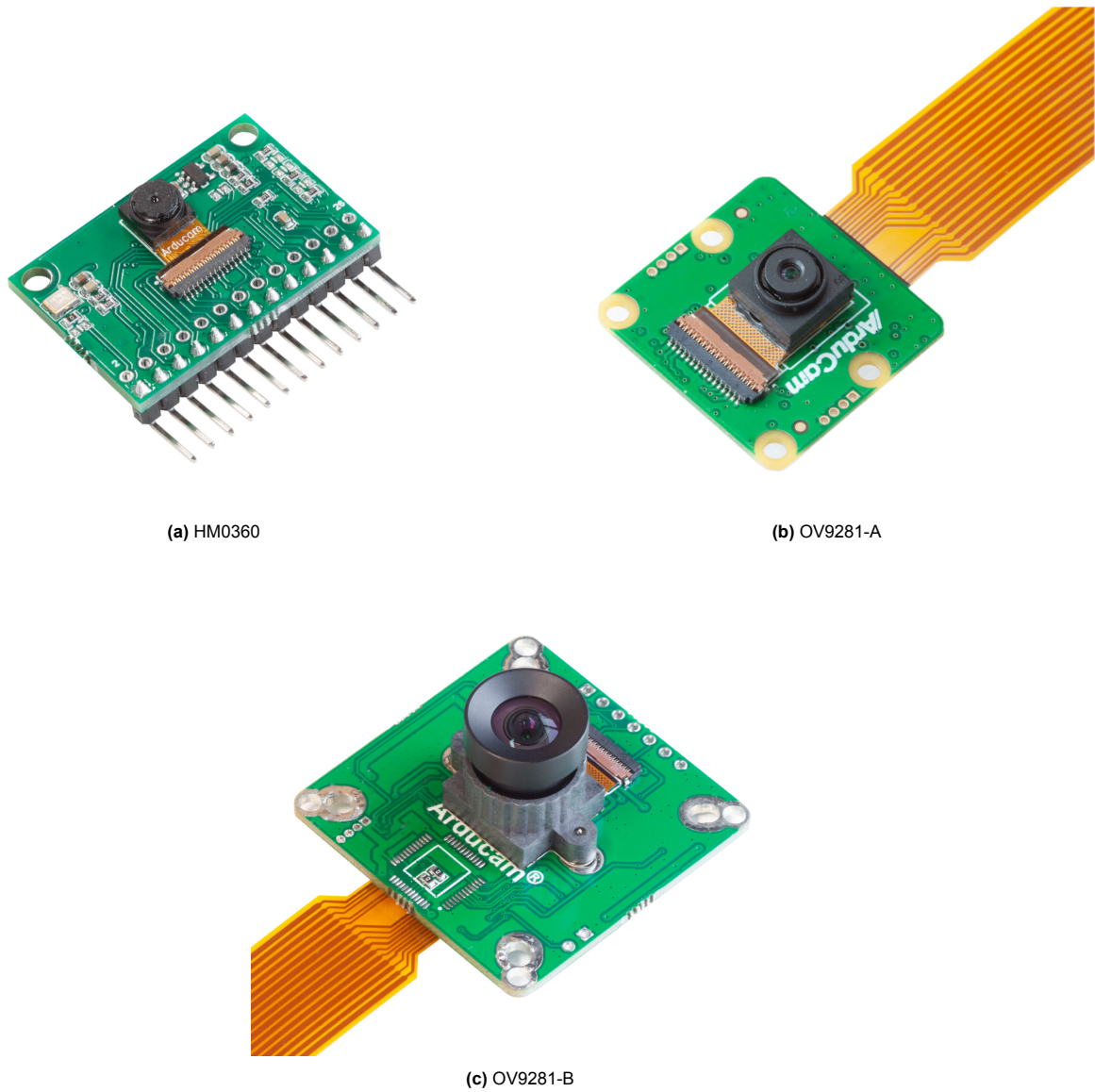


**Figure 4.3:** The three best scoring optical modules from the trade off.

Eventually, the OV9281-A was chosen as it is the sensor that is most applicable to the combined sensor design problem and it offers better accuracy than the HM0360. The power consumption needs to be brought down considerably, but the module offers enough leeway to achieve this. It is also a newer module and provides better compatibility with boards like Raspberry Pi than the HM0360.

## 4.4. Preliminary design

With the OV9281-A selected, the design for the combined versatile optical sensor could begin. The hardware of the optical module cannot be easily changed, but its performance can already be estimated. This will give a good indication of how well the module will perform as a star tracker and Sun sensor, which sensor settings to select and of any modifications that might need to be created, such as a baffle to reduce the impact of stray light.

#### 4.4.1. OV9281-A detailed specifications

Table 4.4 already showed basic specifications of the OV9281-A. More detailed specifications of the sensor module are provided in Table 4.6. Here, information is provided regarding the sensor size, pixels and optical properties such as focal length, which give a more complete overview of the design of the sensor. The sensor can operate in three different resolutions modes, which are included in the table as well. The maximum update rates corresponding to each resolution setting are separated by a "/". Electrical properties and dimensions have also been highlighted.

**Table 4.6:** Detailed specifications of the OV9281-A optical module [34].

General specifications	OV9281-A
Sensor format	1/4"
Chroma	Monochrome
Resolution [pixels]	1280x800 / 1280x720 / 640x480
Update rate [Hz]	120 / 144 / 240
FOV (D/H/V)	89.5° / 75.9° / 47.4°
Accuracy [°/pixel]	0.0593
Focal length [mm]	2.35
F.No	2
Aperture diameter [mm]	1.175
Diffraction limit [°]	0.0238
Electrical properties	
Power consumption [mW]	156
S/N ratio [dB]	38
Dynamic range [dB]	68
Output voltage HIGH [V]	1.62
Output voltage LOW [V]	0.18
Sensitivity [mV/μW.cm <sup>-2</sup> .sec]	13000 @ 850nm
Dimensions	
Image area [mm]	3.896x2.453
Pixel size [μm]	3x3
PCB size [mm]	25x24
Camera size [mm]	8.73x8.52x5.25

The accuracy was found by dividing the diagonal FOV by the number of pixels on the diagonal of the sensor. All resolution settings meet the accuracy requirement of 0.1 [°/pixel], but cropping is applied if the resolution is lowered. The effects of cropping will be explained in subsection 4.4.4. Still, lower resolution settings can be used in the Sun sensor mode, which has lower accuracy requirements. The diffraction limit was found through formula 4.1, where  $D$  is the diameter of the aperture and  $\lambda$  was chosen to be 400 [nm], which is the border between UV light and visible light. A diffraction limit of 0.0238° means that two stars that are closer than this limit cannot be resolved by the camera. Hence, they will end up as a single point on the image.

$$\theta = 1.22 \frac{\lambda}{D} \quad (4.1)$$

The image area is 3.896x2.453 [mm], which results in an aspect ratio of  $\approx 1.6$ . The size of the PCB 25x24 [mm], but the camera itself is only 8x8x5 [mm]. Therefore, this prototype sensor meets requirement CVAS-FLR-08, which states that the sensor can have a maximum size of 20x20x10 [mm]. This means that a height of 5 [mm] is available that can be used to add a longer baffle to the current design. The implications of such a design change will be discussed in subsection 4.4.3.

#### 4.4.2. Star visibility

The electrical properties of the sensor module can be used to determine the total number of stars that are visible to the sensor once in orbit. The dynamic range, sensitivity and output voltage can be converted to

a minimum detectable light intensity, which can be converted to a minimum star magnitude. The number of stars with a magnitude stronger than this can be approximated using an empirical formula. Estimating the number of visible stars is important to know the applicability of the sensor, as having insufficient visible stars means the sensor might struggle to image enough stars for attitude determination.

The sensor's dynamic range can be converted to a ratio between its minimum detectable voltage output and the maximum voltage output. This is done in Equation 4.2. Then, this ratio can be used to determine the minimum detectable voltage output, since the maximum voltage output is known and equal to 1.62 [V]. The result of Equation 4.3 can be divided by the sensor's sensitivity to find the minimum detectable light intensity, which is done in Equation 4.4.

$$\frac{U_{max}}{U_{min}} = 10^{\left(\frac{\text{Dynamic Range}}{20}\right)} = 10^{\left(\frac{68}{20}\right)} \approx 2512 [-] \quad (4.2)$$

$$U_{min} = U_{OH} \frac{U_{min}}{U_{max}} = \frac{1.62}{2512} = 0.645 [mV] \quad (4.3)$$

$$E_{min} = \frac{U_{min}}{\text{Sensitivity}} = \frac{0.645}{13000} \frac{1}{100} = 4.961 \cdot 10^{-10} [W/m^2] \quad (4.4)$$

The minimum detectable light intensity of  $4.961 \cdot 10^{-10} [W/m^2]$  (watts per square meter) is the faintest light that the sensor can observe. Stars need to be brighter than this in order to reach a measurable flux on a pixel in the sensor's images. The minimum intensity can directly be converted to an apparent star magnitude using Equation 4.5. This is a scale for a star's apparent visual magnitude and it is based on the magnitude of Vega, the brightest star in the constellation of Lyra [35]. The larger the apparent visual magnitude number, the fainter the star. It was computed that the sensor is able to see stars that have a magnitude of at least 4.696. Finally, the number of stars visible to the sensor can be determined through a 3rd-degree linear least-squares fit, which is presented in Equation 4.6. This leads to an approximate 1134 stars that will be visible to CVAS, which is lower than currently commercially available star trackers. In addition, noise, such as stray light, could make it difficult to resolve the faintest stars against the background. Therefore, in practice the number of usable stars is likely lower.

Most COTS star trackers are able to detect stars with a minimum magnitude between 6 and 7.5, which are around 5000 to 25000 stars in total [24]. An overview of the number of stars with an certain apparent visual magnitude (V) and their corresponding luminosity (E) is detailed in Table 4.7. COTS star sensors have strong accuracy requirements and focus on preventing the impact of stray light by limiting their FOV. Because of this, they see a smaller portion of space. But, they compensate for this by being more sensitive to light in order to pick up fainter stars for attitude determination.

$$V_{min} = -2.5 \cdot \log_{10} \left( \frac{E_{min}}{3.75 \cdot 10^{-8}} \right) = 4.696 [-] \quad (4.5)$$

$$N_{stars} = 10^{\left(0.754 + 0.4896 \cdot V_{min} + 0.001159 \cdot V_{min}^2 - 0.000235 \cdot V_{min}^3\right)} \approx 1134 \text{ stars} \quad (4.6)$$

Meanwhile, CVAS is only able to see the brightest stars in space, but its wide FOV allows the sensor to still see enough stars in a single frame. A single optical module produces an image that covers close to 14% of the night sky, which means that on average 158 stars are visible. For comparison, a COTS star sensor with a  $15^\circ \times 15^\circ$  that can observe 20000 stars only sees around 1% of the sky at a time, which brings the average stars in frame to 200 stars. Thus, the CVAS should be able to observe enough stars for attitude determination.

**Table 4.7:** The number of stars and their luminosity for different apparent magnitudes [35].

V	# of Stars	E [W/m <sup>2</sup> ]
0	4	3.75E-08
1	15	1.49E-08
2	48	5.94E-09
3	171	2.37E-09
4	513	9.42E-10
5	1602	3.75E-10
6	4800	1.49E-10
7	14000	5.94E-11
8	42000	2.37E-11
9	121000	9.42E-12
10	340000	3.75E-12

### 4.4.3. Impact of baffle on stray light

Sunlight and light reflected from Earth can enter the sensor even when these come from outside the sensor's field-of-view. Stray light can enter the lens and illuminate pixels on the APS due to refraction in the lens. This makes it more difficult for the sensor to image and identify faint stars, which in turn lowers the overall performance of the sensor. A simple method to limit stray light is to install a baffle to the COTS optical module. This section will explain the impact of a baffle on reducing the amount of stray light entering the combined sensor.

To better understand the interaction between stray light and the sensor module, a 3D model of the module was created. This model can be seen in Figure 4.4 and it was based on direct measurements of the optical module and parameters in its data sheet. A cross-section of this model is presented in Figure 4.5. Here, the module's diagonal FOV is indicated by the angle  $\theta$ , while the stray light is able to hit the lens with a maximum angle of  $\zeta$ . The OV9281-A already has a small baffle installed right in front of the lens. This is a baffle with a 45° half-angle and is 0.4 [mm] in height. Since the sensor has a diagonal FOV of 89.5°, the baffle is positioned just outside the imaging frame and does not interfere with measurements.

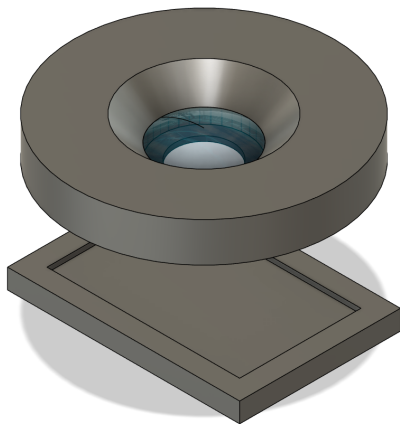


**Figure 4.4:** A 3D model of the OV9281's lens, active pixel sensor and outer structure.

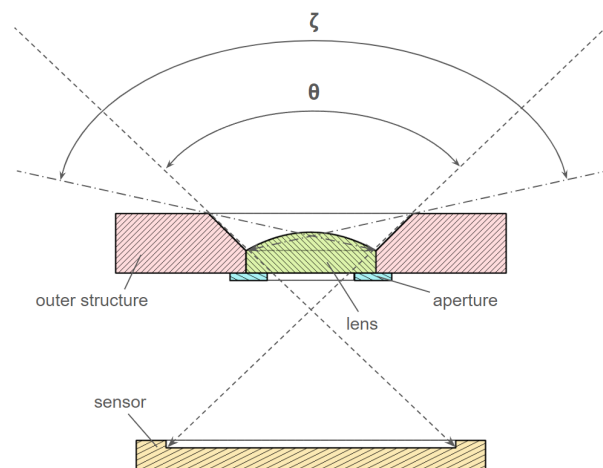


**Figure 4.5:** Cross-section of the OV9281, including the angles for FOV ( $\theta$ ) and stray light ( $\zeta$ ).

Angle  $\zeta$  follows from the lines between one end of the lens to the tip of the baffle at on the opposite side. These lines can be seen in Figure 4.5. The larger this angle, the more stray light is able to enter the sensor and able to interfere with the images. Ideally,  $\zeta$  should be as close to  $\theta$  as possible, but this would bring the baffle length beyond the 10 [mm] maximum height allocated to the sensor. Therefore, it was calculated what the impact of several baffle lengths will be on the maximum stray light angle. For this, the interaction between

stray light, lens and baffle was simplified to a set of geometry as defined in Figure 4.6.

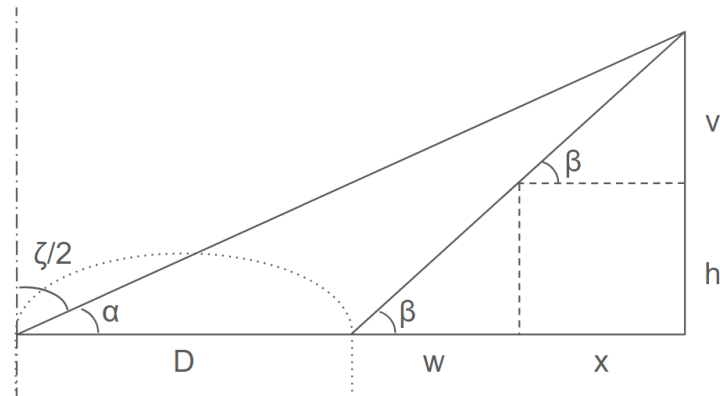


**Figure 4.6:** Schematic view of an extended baffle with an height  $v$  and a width  $x$ . The lens of the optical module is given with the curved dotted lines.

In this geometry, the diameter of the lens has been labeled  $D$ , while the width and height of the original baffle are labeled  $w$  and  $h$  respectively. The baffle can be extended by a height  $v$ , while the angle of the baffle,  $\beta$ , remains fixed. Then, the width of the extended baffle can be calculated using Equation 4.7. Subsequently, the angle  $\alpha$  can be calculated using basic geometry, as presented in Equation 4.8. Finally, Equation 4.9 can be used to find the maximum stray light angle for a particular baffle configuration.

$$x = \frac{v}{\tan(\beta)} \quad (4.7)$$

$$\alpha = \tan^{-1} \left( \frac{v + h}{D + w + x} \right) \quad (4.8)$$

$$\zeta = 180^\circ - 2\alpha \quad (4.9)$$

These equations were performed for several different baffle lengths. The results can be seen in Figure 4.7. Initially, the standard configuration with no extended baffle will have a maximum stray light angle of  $159^\circ$ . This far exceeds the sensor's FOV of  $89.5^\circ$  and therefore it is likely that stray light will affect the images negatively. Extending the baffle by only 1 [mm] already reduces  $\zeta$  to  $132^\circ$ , which is a significant improvement for only a minor adjustment to the design of the sensor. Increasing the baffle to 4.75 [mm] would make the sensor overall 10 [mm], which is the limit according to requirement *CVAS-FLR-08*, and it would lower  $\zeta$  down to  $106^\circ$ . This upper limit has been indicated in the figure with the black dotted line. The graph also shows that increasing the baffle length further yields diminishing returns. Still, it can be concluded that lengthening the baffle by only several [mm] can already reduce the amount of stray light entering the sensor significantly. Therefore, chapter 5 will further explore the design of an extended baffle.

#### 4.4.4. Power reduction measures

The power consumption of the combined sensor needs to be reduced from 156 [mW] to 70 [mW] in order to make the sensor competitive. It was investigated which camera settings could reduce the power consumption, like the resolution and the update rate. This section will present the predicted effects of those power reduction measures, followed by the results of a power consumption test, which was performed in the latter stages of the thesis.

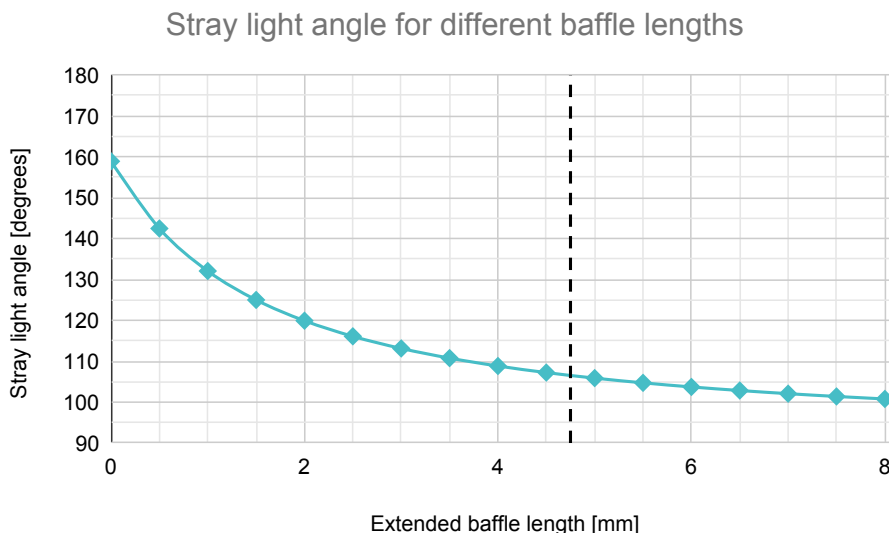


**Figure 4.7:** Impact of different baffle lengths on stray light angle. The dotted line is the maximum allowed baffle length.

#### 4.4.4.1 Resolution modes

First, the impact of lowering the resolution of the sensor was considered. A lower resolution should cause fewer pixels to be active, which could potentially reduce power consumption. The sensor will perform cropping when a resolution lower than 1280x800 [pixels] is selected. With cropping, a number of pixels on the sensor are deactivated, which causes the image to be smaller. The pixel density is maintained, so there is no loss in accuracy. However, the FOV is reduced, which is a major drawback.

Unfortunately, the official data sheet of the optical module does not feature numbers on the power consumption of each resolution mode, but an attempt was made to estimate the effect. An assumption was made that the power consumption would decrease linearly with the number of active pixels. The results of this approximation can be seen in Table 4.8. However, this does not take into account other processes, such as overheads, that the module needs to perform while sampling. Therefore, the power consumption is likely to be higher than predicted.

**Table 4.8:** Approximated power consumption of different sensor resolution modes.

Resolution mode	1280x800	1280x720	640x480	640x400
# of pixels [Mp]	1.024	0.922	0.307	0.256
Power consumption [mW]	156	140	47	39

The OV9281-A offers a fourth resolution mode that is 640x400 [pixels] and uses 4:1 sub-sampling. Here, no cropping takes place and the original FOV is maintained. The sensor combines the output of 2x2 pixels and returns their average value. This could reduce the computational load on the sensor and could be a good candidate for the Sun sensor mode, which does not require the same accuracy levels as the star tracker mode. Unfortunately, it is unknown how big of an effect this sub-sampling has on the power consumption. For the sake of completeness, a predicted power consumption following the linear pixel relationship has been included in Table 4.8. A power consumption test was performed to find the actual power consumption of different resolution settings, which can be read in subsection 4.4.4.3.

#### 4.4.4.2 Update rate

The standard update rate of the OV9281-A is 120 [Hz] at a resolution of 1280x800 [pixels]. Since the flight-ready sensor only needs to provide 10 frames per second and the prototype 5 frames in the Sun sensor mode,

there is the potential to lower the power consumption substantially. According to the official data sheet, the reduction in power consumption can be approximated to follow Equation 4.10, where  $N$  is the number of frames the sensor streams and  $M$  is the number of frames the sensor idles [34]. Both types of frames have the same length.

$$P_{reduced} = \frac{N}{N + M} P_{standard} \quad (4.10)$$

In the standard configuration, the sensor is streaming frames 120 times per second and there are no idling frames. But when the number of streaming frames is reduced to 10 frames per second, then 110 frames per second are used for idling. This brings  $N/(N + M)$  down to 0.0833, which is a power reduction ratio of 12, and results in an approximated power consumption of 13 [mW]. Similarly, the star tracker mode requires an update rate of 2 [Hz], which gives a power reduction ratio of 60 and a predicted power consumption of 2.6 [mW]. This does not seem realistic as the sensor still consumes power for background processes. The eventual power consumption is likely to lay several times higher. Also, it is important to understand that this assumes that the exposure time of a single frame has not been changed and is sufficiently long for each sensor mode.

In the Sun sensor mode a short exposure time is possible, due to the vast amount of light entering the lens. If required, the exposure time can be shortened or lengthened as there is enough margin in the power budget. The opposite is true for the star tracker mode. The star tracker requires a long exposure time in order to see the stars properly. The maximum exposure time for each mode was derived in the following way.

It was believed that the frame duration and number of frames should be chosen in such a way that a power consumption below 70 [mW] can be achieved. Since the standard power consumption of the sensor is 156 [mW], a target power reduction factor would be  $156/70 = 2.229$ . Since for the Sun sensor mode  $N = 10$ , the number of idling frames becomes, after rounding up to the nearest whole number,  $M = 13$ . Therefore, each second there are 23 frames in total, 13 of which are frames for idling. Each frame lasts approximately  $1/23 = 0.044$  [s], which is also the maximum exposure time for the Sun sensor mode. The total power reduction is a factor 2.3, which results in a power consumption of  $156/2.3 \approx 68$  [mW]. The same steps can be applied to the star tracker mode. Here,  $N = 2$  and after utilizing Equation 4.10 and rounding up, it is found that  $M = 3$ . That equates to 5 total frames per second and a single frame length and maximum exposure time of 0.200 [s]. The power reduction in the star tracker mode would then be a factor of 2.5, leading to a power consumption of  $156/2.5 \approx 62$  [mW]. A full overview of the predicted power consumption and exposure time of different sensor modes and update rates can be seen in Table 4.9.

**Table 4.9:** The predicted effects of a reduced update rate on power consumption for different sensor modes.

Sensor modes	N [Hz]	M [Hz]	Power reduction ratio [-]	Power consumption [mW]	Exposure time [s]
Sun sensor 10 [Hz]	10	110	12	13	0.0083
Star tracker 2 [Hz]	2	118	60	3	0.0083
Sun sensor max exposure	10	13	2.3	68	0.0435
Star tracker max exposure	2	3	2.5	62	0.2000

#### 4.4.4.3 Power consumption test

During the testing phase of the thesis, voltage and current meters were connected to the sensor in order to measure its power consumption. Testing was done using two resolution modes and for different frame rates. These settings were already defined for the Sun sensor and star tracker modes as initial testing had already been performed. In addition, different settings for analogue gain and exposure times were tested. More information on analogue gain and other camera settings can be found in section 5.2.

The power consumption was measured for resolution settings 1280x800 and 640x400 pixels. Next to that, the frame rate was varied with the settings (1,2,5,10,20,30) [Hz] and the capture methods 'video' and 'still' were selected. The results of this test can be seen in Figure 4.8. There appeared to be no significant difference between capture methods and only a small difference in resolution settings. Different analogue gain settings

and exposure settings also had an effect of less than 0.1 [mW] on the power consumption at frame rates below 5 [Hz], far lower than what was believed. This meant that the exposure times are not limited by the power consumption limit, but by the time required for the algorithm to solve the images. This finding is especially important for the performance of the star tracker.

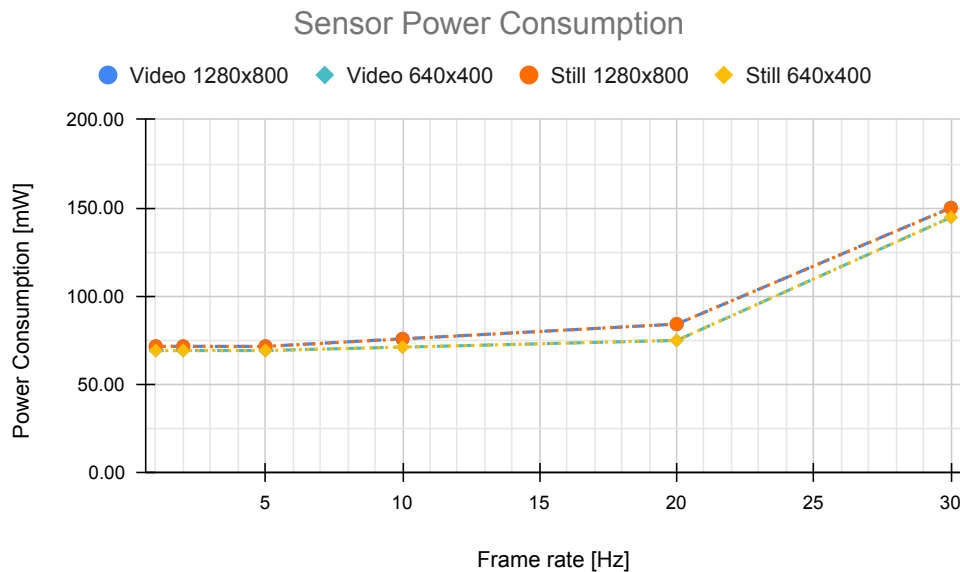


**Figure 4.8:** Power consumption of sensor against frame rate and different capture settings.

Most importantly, there appears to be a steep drop-off in power consumption between a frame rate from 30 to 20 [Hz]. Below 20 [Hz], the power consumption does not decrease as much and a minimum power consumption is being reached. The most likely reason is that this minimum power reflects the background processes or overheads of the sensor, which are a requirement for the sensor to function. It is estimated that these processes limit the minimum power consumption to around 69 [mW], which is just below the requirement of 70 mW. Testing showed that the sensor can operate in Sun sensor mode (640x400 pixels, 5 [Hz]) at 69.3 [mW] and 71.3 [mW] for 10 [Hz]. The star tracker mode consumes 71.7 [mW] up to 5 [Hz], but the star tracker will function at a maximum of 2 [Hz] regardless. Between the two resolutions, there is a maximum of 11% reduction in power when choosing the lower 640x400 resolution, compared to 1280x800.

From these observations, it can be concluded that the power consumption of the combined sensor is primarily determined by the frame rate and fractionally by the resolution setting. Since the targeted frame rates for this sensor are below 10 [Hz], the sensor approaches its minimum power consumption of roughly 69 [mW]. Settings like the analogue gain and exposure time do not appear to have a significant effect. Therefore, these can be tuned to what is most optimal for the respective sensor mode, without increasing the power consumption.

# Detailed Prototype Design

The preliminary design chapter investigated the required performance of the combined versatile attitude sensor, which COTS sensor to select and which operational modes are ideal. This chapter will build on that knowledge by defining in detail the design of the prototype sensor. Operational modes will be selected and a design for a stray-light-reducing baffle will be given. Furthermore, the algorithms required to analyse the stars and the Sun will be explained in detail.

The chapter begins with the design of the baffle in section 5.1. Then, the sensor operational modes are presented in section 5.2, which are chosen to offer sufficient accuracy while consuming limited power. Thereafter, section 5.3 explains the star tracker algorithm. Finally, the Sun sensor algorithm is presented in section 5.4.

## 5.1. Baffle design

The findings in subsection 4.4.3 showed that the impact of stray light can be significantly reduced by installing a baffle onto the sensor module. Figure 4.7 presented the estimated stray light angle for a given baffle length. The original sensor module design has a small baffle that has a stray light angle of  $159^\circ$ , while an extended baffle can reduce that to  $106^\circ$  while meeting the sensor requirements, which is significantly closer to the sensor's FOV of  $89.5^\circ$ . This section will present a baffle design fit for the combined versatile attitude sensor.

The baffle angle is fixed at 45 degree half-angle and its height can be at maximum 4.75 [mm] due to requirement *CVAS-FLR-08*. In order to maintain clearance in the design and because of diminishing returns, it was decided to extend the baffle by 4.00 [mm]. Theoretically, this would reduce the stray light angle to  $109^\circ$ . The 3D model, which can be seen in Figure 4.4, was used to create a baffle design that could be placed onto the sensor module. An initial design was designed to slide over the entire sensor module and hold itself in place with friction. This design is displayed in Figure 5.1. The total dimensions are 11x11x9.25 [mm] with a 4.00 [mm] cone.

The complex geometry of this design required the baffle to be 3D printed. Unfortunately, 3D printing is a coarse manufacturing technique that leads to imperfections on the surface of the baffle. These are visible in Figure 5.2, where the baffle has been placed over the OV9281 sensor module. The imperfections are most noticeable on the top plane and inside the cone. Although they could interfere with the imaging quality of the sensor module, the baffle is positioned slightly out of the field-of-view of the sensor. This margin could prevent the imperfections from causing negative effects, but the exact implications need to be identified through testing. Moreover, because the 3D printer prints in layers, the baffle gets a 'staircase' texture on the inside. The material in this staircase is smooth and seems to reflect light easily, which is not ideal for an effective baffle. However, the zig-zag layout of the staircase could help to reduce internal reflections compared to a fully flat surface. Future studies and design should look into better manufacturing techniques, but for a prototype the current design suffices.



**Figure 5.1:** 3D model of the 4 [mm] baffle created for the OV9281 sensor module.

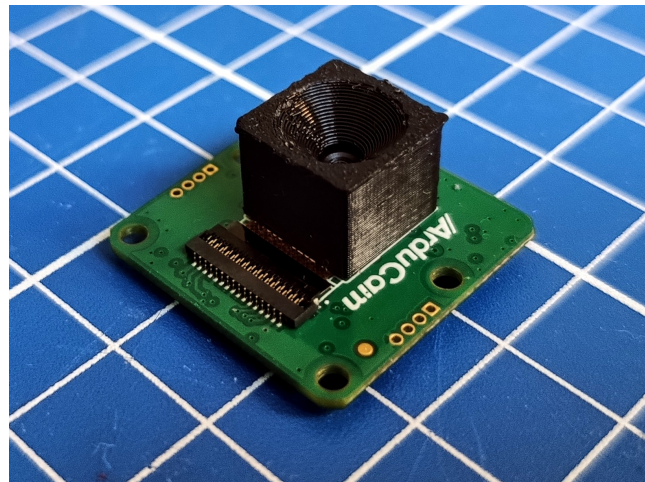


**Figure 5.2:** The baffle placed over the OV9281 sensor module. Imperfections are visible on the top edge and inside the cone.

## 5.2. Sensor operational modes

In subsection 4.4.4 the impact of different resolution and update rates on the sensor's power consumption was explored. A test showed that with the desired resolution and frame rate settings the power consumption is around 70 [mW], which is similar to requirement *CVAS-FLR-09*. This is only the power consumption of the sensor and does not take into account the micro controller that will analyse the images, which is beyond the scope of this thesis. This section will use the information gathered in subsection 4.4.4 to define the settings of each sensor mode for the prototype combined sensor.

The prototype star tracker will operate on a resolution of 1280x800 pixels in order to achieve the highest accuracy. It does this on a frame rate of 1 [Hz], but the flight-ready design will operate on 2 [Hz]. This should be taken into account when defining the maximum exposure time of the sensor mode. The exposure time of the prototype cannot be higher than that of the flight-ready sensor, as a difference between the two would make for an uneven comparison of star visibility. Therefore, the maximum exposure time will be set to 0.500 [s], so that two frames can be created each second. Testing showed that the exposure time had a minimal effect on the power consumption of the sensor and thus this can be changed freely. The micro controller, which will not be designed in this thesis, should be able to analyse an image in parallel with the sensor imaging the next frame. Naturally, the shorter the exposure time, the more time available for the controller to analyse the images, which is beneficial.

The prototype Sun sensor has lower accuracy requirements and can therefore operate at a resolution of 640x400 pixels. Although this saves some power compared to the star tracker, the Sun sensor mode will operate at an update rate of 5 [Hz], which slightly raises the power consumption again. The exposure time will have to be tuned using the tests in chapter 6, but its range will be around 0.01 [s] or less.

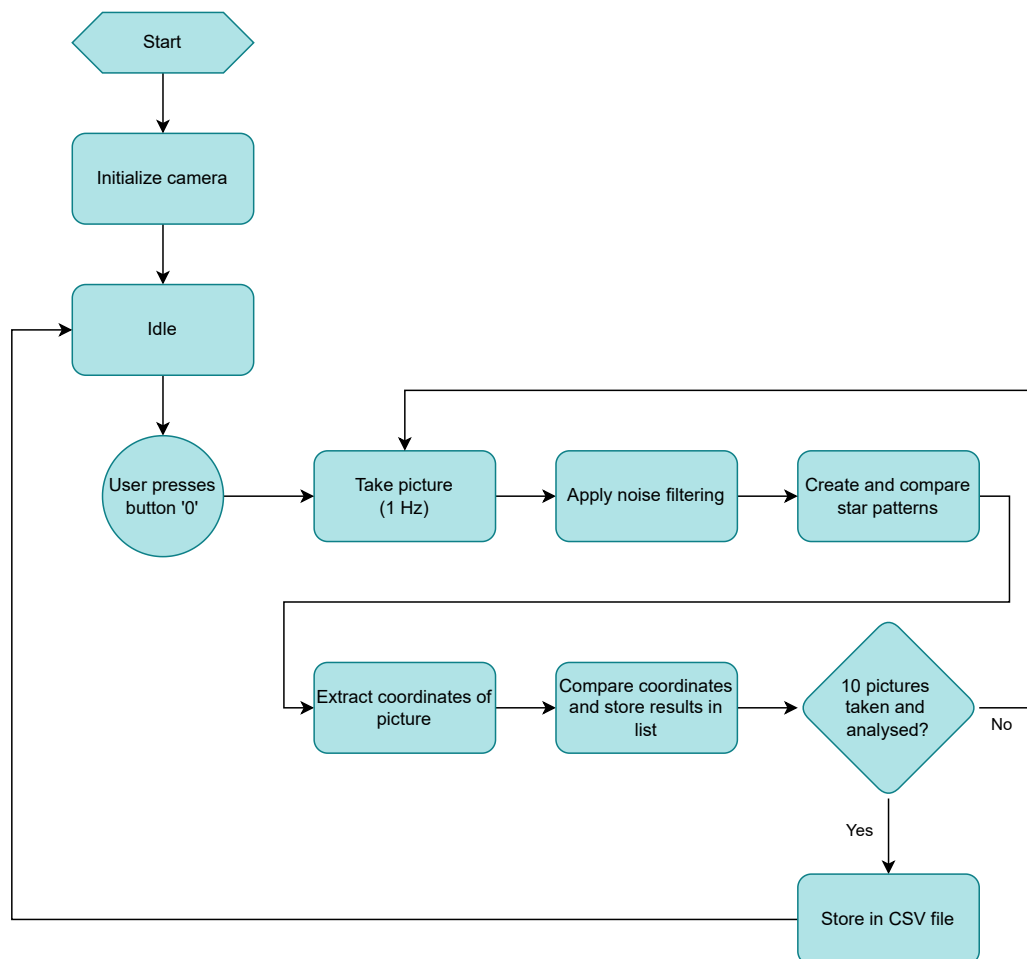
In addition to these settings, settings for automatic brightness, contrast and white-balance modes were disabled. This helped to ensure that every picture taken with the sensor was done with the same settings. Preliminary tests with both sensor modes showed that with the automatic settings enabled, the brightness levels changed according to the light level. This resulted in stars not appearing on night sky images and Sun spots changing size between measurements. Another important settings is the analogue gain, which amplifies the difference between dark pixels and white pixels on an image, which improves the visibility of stars. However, higher gains also increase noise levels, which highlights the importance of good noise filtering. Initial testing showed that for values lower than 8.0 the stars were too faint for the algorithm to detect them, whereas for values higher than 10.0 the noise levels started to interfere with stars in the image. In order to identify the most optimal setting, analogue gains ranging from 8.0-12.0 were tested during the star tracker functionality test in subsection 6.2.1. For the Sun sensor test, the gain was kept at a default value of 1.0, since those images are very bright. An overview of the settings for both sensor modes has been given in Table 5.1.

**Table 5.1:** Settings and predicted power consumption of combined sensor prototype modes.

Sensor mode	Update rate [Hz]	Exposure time [s]	Analogue gain [-]	Other settings	Predicted power consumption [mW]
Sun sensor	5	0.0001-0.0100	1.0	Automatic brightness, white-balance and contrast disabled	69
Star tracker	1	0.200-0.500	8.0-12.0	Automatic brightness, white-balance and contrast disabled	71

### 5.3. Star tracker algorithm

A custom Python 3 script was created to operate the star sensor mode during testing. Since the OV9281 camera module is natively compatible with the Raspberry Pi platform, the script can utilise the Picamera2 library. This library enables the user to control camera modules using Python scripts. With these scripts, a free-to-use star finder program called Astrometry.net can be used, which analyses the images and finds the images' coordinates. Figure 5.3 shows a schematic layout of the star tracker activity flow. A link to the full star tracker code can be found in Appendix C.

**Figure 5.3:** Schematic view of the prototype star tracker mode activity flow used in testing.

First, the camera is configured with the correct settings for the Sun sensor mode, as detailed in section 5.2. Once this has been completed, a small preview window shows the user that the camera is operational. From

this moment, the sensor is in idle and waits for the user to start the measurements using by pressing the button '0' on the keyboard.

Then, the script tells the sensor to take a picture once a second or, in case resolving the pictures takes longer than a second, to make a picture at the earliest opportunity. Thereafter, noise filtering is applied to the images. This filtering consists of removing the average of 10 dark frames from the image, which is a common method to reduce noise. The downside of this method is that faint stars could also be removed from the image.

After removing the noise, a picture is analysed by the Astrometry.net code. This code was created by Lang et al. (2010) and consists of four steps. The first step is to identify stars in the image. Then, the algorithm splits the image up into several sectors and creates a geometric hash code between the four brightest stars in each sector. In this case, the geometric hash code is the coordinates of the two middle stars in a local reference frame. An example hash code of four stars is presented in Figure 5.4, where the coordinates of stars C and D form the code. This step is repeated for the next four brightest stars, until all stars have been turned into hash codes. The result is an entire image covered in geometric hash codes, as can be seen in Figure 5.5. The third step is to compare the hash codes to a database and to search for a matching index. This gives a hypothesized location, orientation and scale of the stars in the image. The final step is to perform a verification step. Here, the algorithm assumes that a certain hash code is in the correct location and predicts the location of other stars from it. The computer continues this step until a hypothesis is found that yields correct alignment with the stars in the picture [36].

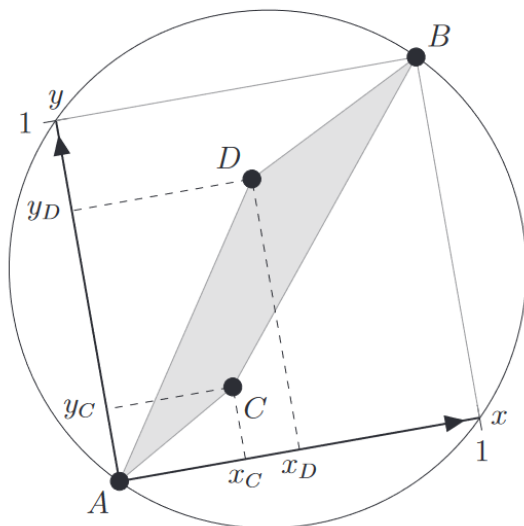


**Figure 5.4:** An example geometric hash code from stars A, B, C and D. The coordinates of these stars form the has code  $(x_C, y_C, x_D, y_D)$  [36].

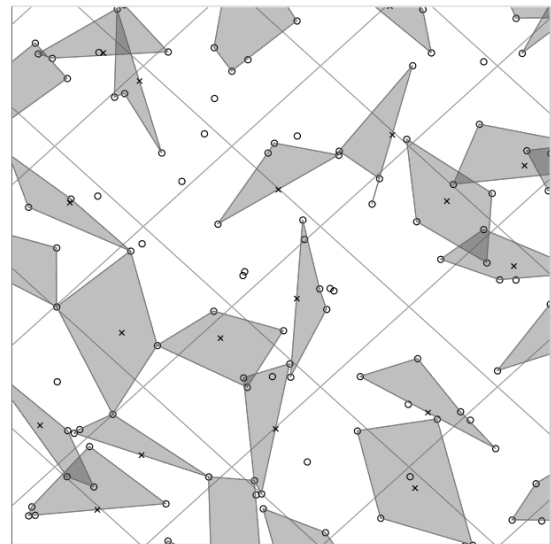


**Figure 5.5:** A grid of hash codes applied to an image. These can be compared to a database to find the location of the image in the night sky [36].

The developer of Astrometry.net claims that with a clear image and sufficient processing power, the algorithm should be able to resolve an image within 10 seconds. Faster computer systems and updates to the algorithm have allowed for images to be resolved within a second. The algorithm has been thoroughly tested and yields a >99.9% success rate with no false positives [36]. Therefore, the code should be suitable for use in the prototype combined sensor, although the code might be too robust for this application and a simpler algorithm might yield similar results, while reducing CPU load. An algorithm that is specifically optimized for the flight-ready combined sensor would be preferred, as the Astrometry.net code is computationally expensive and therefore draws more power and memory.

Furthermore, users of Astrometry.net have found that the algorithm struggles to compute large FOV images. To solve this, images can be downsampled, but this comes at the cost of accuracy. Initial outdoor testing with the star tracker showed that the algorithm had no trouble with wide FOV images of almost  $90^\circ$  and any distortions caused by the sensor's optics. Downsampling was not required for the sensor to function as intended, so the speed and accuracy of the sensor is not further compromised. Then, it was unknown

whether the algorithm would continue to work if it sees only roughly 1100 stars in total. This is the case for the prototype combined sensor, which is less sensitive to starlight than typical star trackers. In order to understand these issues, eight images with similar FOV and star magnitudes to what the combined sensor would see, were processed by the algorithm. These images were created using Stellarium. All images were successfully processed by the algorithm, although a default downsampling ratio of 2 was used, since the algorithm appeared to be struggling with wide field images from Stellarium. The most likely cause for this is that Stellarium tries to display a spherical image onto a flat surface, which introduces excessive distortions. The mean error was determined to be  $\pm 0.03^\circ$  for right ascension and  $\pm 0.02^\circ$  for declination. This error is two orders of magnitude lower than the target accuracy of the combined sensor prototype and therefore this algorithm is sufficiently accurate for this thesis. Subsequent preliminary outdoor tests revealed that as little as 30 stars is enough for the algorithm to find the coordinates of a star image.

Once the coordinates of the image have been identified, the ADCS computer of a satellite would use this to derive the attitude of the spacecraft. For this prototype and experiments, the coordinates are instead stored in a list. At the end of the experiment, these are exported through a CSV file, which is post-processed to find the root mean square error and 1-sigma standard deviation. This way, the results of the experiments can be compared against the known right ascension and declination of the original image. The difference between the two is the accuracy of the sensor.

## 5.4. Sun sensor algorithm

Similarly to the star tracker algorithm, Python 3 was used for the Sun sensor mode during testing. Instead of utilizing Astrometry.net, the Sun sensor code used an algorithm with the OpenCV library for Python, which can analyse images and derive the center of the Sun spot. A schematic overview of the activity flow can be seen in Figure 5.6. A link to the full Sun sensor code can be found in Appendix C.

First, the camera is configured in the same manner as explained in section 5.3. Now, the settings for the Sun sensor mode are selected instead. After the preview window has been loaded, the sensor waits for a user input before starting the measurements.

Here, the sensor takes a picture at a speed of 5 [Hz] and starts processing and analysing it immediately. A raw test image taken during the development of the algorithm can be seen in Figure 5.7. Then, a Gaussian filter is applied using the OpenCV library in order to smoothen the image. This will filter out unwanted noise that could lead to the algorithm picking up pixels away from the Sun spot. The radius of the Gaussian filter is important, as it determines how many pixels are averaged with each other. This radius should be tuned before the start of the experiments. An example of the Gaussian filter and radius applied to a test image can be seen in Figure 5.8. The white circle is centred on the brightest spot in the image and has a radius equal to the radius of the Gaussian filter. The small black circle indicates the center of the image.

The Sun spot coordinates are found by using the OpenCV function *minMaxLoc()*. This finds the region of an image with the brightest pixels and returns the screen coordinates. These can be related to the azimuth and elevation angle of the Sun. The azimuth  $\theta$  can be calculated by taking the inverse tangent of the distance of the Sun spot to the center of the active pixel sensor,  $l$  divided by the focal length,  $F$ , as can be seen in Equation 5.1 [17]. The same equation holds for the elevation  $\phi$ .  $l_h$ , the horizontal distance of the Sun spot to the center, can be calculated using Equation 5.2.

$$\theta = \tan^{-1} \left( \frac{l}{F} \right) \quad (5.1)$$

$$l_h = \left( X_{coord} \text{ brightest pixel} - \frac{\text{Horizontal resolution}}{2} \right) \cdot \frac{\text{APS width}}{\text{Horizontal resolution}} \quad (5.2)$$

With a focal length of 2.35 [mm] and an active pixel sensor of 3.896x2.453 [mm], the maximum Sun angles are  $\pm 39.6^\circ$  and  $\pm 27.6^\circ$  for azimuth and elevation respectively. This leads to a maximum FOV of  $79.2^\circ$  and

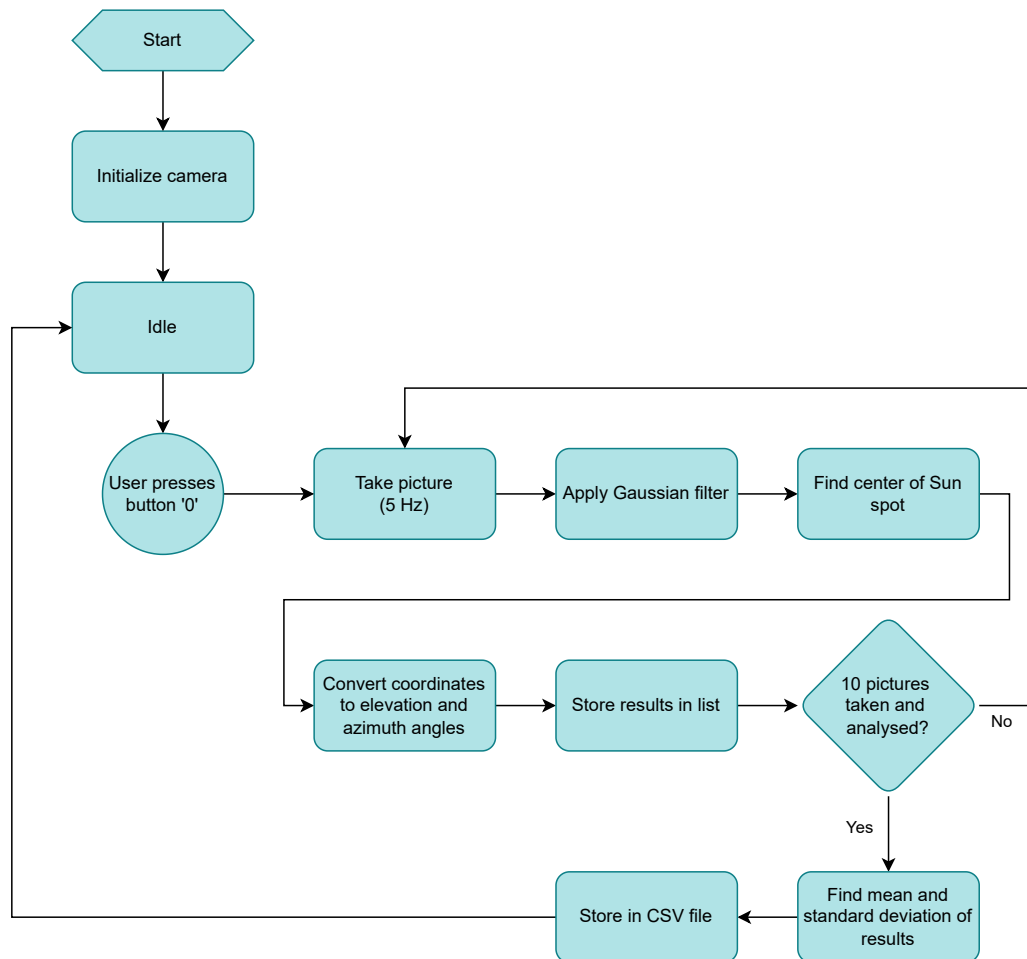


**Figure 5.6:** Schematic view of the prototype Sun sensor mode activity flow used in testing.

$55.2^\circ$  in horizontal and vertical direction. The Sun angles that are calculated using Equation 5.1 are stored in a list, while the sensor continues to take images until 10 images have been taken and processed in total. This is only done during testing so that the results can be compared against the actual Sun angles.

Once 10 images have been taken, the testing round ends and the root mean squared error and standard deviation are calculated. The mean was taken to account for potential errors in the imaging of the Sun and the post-processing. The standard deviation was calculated to understand the variance in the data. These results are stored in a CSV file, which will be used to define the accuracy of the sensor. Once this has been completed, the sensor returns to the idle state until the next testing round is started by the user.

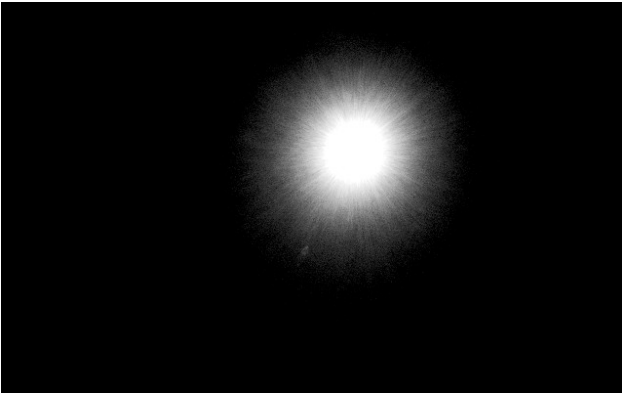


**Figure 5.7:** A raw test image to investigate and tune the algorithm of the Sun sensor mode.

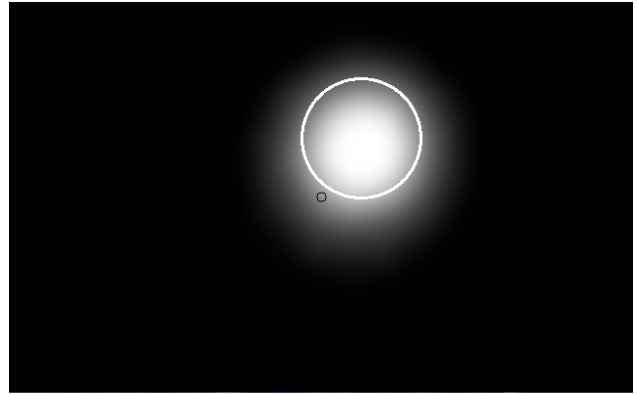


**Figure 5.8:** A processed test image through a Gaussian filter. The white circle is positioned on the coordinates of the brightest pixel.

# Testing

The combined versatile attitude sensor will be tested on its functionality and performance in both Sun sensor mode and star tracker mode. The testing will be split up into separate tests for each mode. The functionality tests have the aim to verify that the sensor modes work as intended, whereas the performance test will focus on determining the accuracy of the sensors. In addition, the power consumption of the sensor will be measured. A separate test was planned to determine the effectiveness of the baffle design, but this test could not be performed due to time constraints.

This chapter will begin with an overview of the experimental setups for each sensor mode, as explained in section 6.1. The results of the tests are presented in section 6.2. Links to the specific sections regarding a test can be found in Table 6.1. The test plans can be viewed in Appendix B, including the test plan for the baffle effectiveness test that was not performed.

**Table 6.1:** Overview of the tests performed and their locations in this document.

Test name	Test plan	Results
Star tracker functionality test	subsection 6.1.1.1	subsection 6.2.1
Star tracker performance test	subsection 6.1.1.2	subsection 6.2.2
Sun sensor functionality test	subsection 6.1.2.1	subsection 6.2.3
Sun sensor performance test	subsection 6.1.2.2	subsection 6.2.4
Baffle effectiveness test	subsection 6.1.3	Not performed

## 6.1. Experimental setup

Each test of the combined versatile attitude sensor requires a different experimental setup. Several test plans were created that explain the experimental setup and methodology for each test. They provide a description of the tests, list their primary and secondary goals, give a list of items necessary to perform the tests and will provide a list of testing tasks to carry out. The test plans were written so that the tests are replicable. Detailed explanations of the experimental setup for the star tracker sensor mode can be seen in subsection 6.1.1, while those for the Sun sensor are detailed in subsection 6.1.2. An overview of the baffle effectiveness test is described in subsection 6.1.3.

### 6.1.1. Star tracker tests

The star tracker mode will be tested twice. The first test is to test the functionality of the sensor mode, which ensures that the sensor is able to use images of the stars for attitude determination. The second test will analyse the performance and power consumption of the sensor. Both test plans are described in the following sections.

### 6.1.1.1 Functionality test

The functionality test plan of the star tracker mode can be seen at the end of this subsection. The functionality test has the primary goal to verify that the sensor module is able to derive the right ascension and declination of a star image. Its secondary goal is to verify that the algorithm used in this process is sufficiently fast. These goals cover requirements *CVAS-PROTO-02* and *CVAS-PROTO-09*. The sensor will be placed on a flat table with an unobstructed view to the night sky. The sensor will take images of the stars and will try to process them using a star pattern algorithm.

One testing method is to perform the test in a dark room with a monitor displaying images of the night sky. The monitor would have its settings adjusted so that the light level of the stars on display matched the brightness level of actual stars. This controlled environment would allow for testing independent of weather or time of day and controlled tests that could be compared against each other. However, it turned out that monitors cannot come close to displaying the brightness levels of faint magnitude 5 stars. Also, a monitor creates distortion on the images, since it tries to display a 'spherical' night sky with a flat surface. Star tracker companies correct this using a special lens, but this was not feasible or available for this thesis. In addition, companies that were contacted during the thesis stated that a so called 'star simulator' is used mostly to investigate the robustness of the star tracker algorithm and is not a representable environment for testing the accuracy of the sensor. Therefore, it was decided to visit a local observatory and test the sensor outside at night.

The local observatory was the Sterrenwacht Copernicus, in Overveen, the Netherlands. It is situated on the outskirts of Haarlem in the dunes. Here, lights are forbidden at night and the trees surrounding the site shield it from stray light of buildings close-by. On a clear night, stars up to magnitude 4-4.5 should be visible. The testing took place on a concrete patch next to their observatory.

Testing is carried out in several steps. The sensor is placed directly towards zenith. Each measurement run, the sensor takes 10 images of the sky and analyses these. Should the sensor image enough stars, then the algorithm should be able to return the coordinates of the image, which should be similar to the actual zenith coordinates at the time of the picture. During the functionality test, it is measured if the algorithm could keep up with an update rate of 1 [Hz] and whether the sensor is able to resolve the images.

The number of images required was found through a statistical model. Since the outcome of the functionality test is a *True* or *False*, Equation 6.1 can be used, where  $p$  is 0.5. A confidence level of 65% was selected ( $Z=1$ ), as this test is merely to proof the maturity of the sensor. For a test error of 5%, 96 measurements are required. However, this would take a considerable amount of time, so the number of tests was reduced to 50. This would yield a test error of 7%.

$$n = \frac{Z^2 \cdot p \cdot (1 - p)}{E^2} \quad (6.1)$$

The testing can be deemed a success when 40 out of 50 images are correctly identified and the sensor operates at a speed of at least 1 [Hz]. When 80% of the images can be solved, the prototype can be considered mature enough to continue to performance testing. The final design of the sensor should be capable of finding the spacecraft's attitude closer to 99% of the time, but an 80% success rate already shows that the concept can function as intended. It should be noted that stars are more easily photographed in space due to better lighting conditions and absence of an atmosphere. And the settings for the sensor will not be optimal yet after initial testing. Furthermore, the prototype sensor has an algorithm that has not been optimized for the combined sensor yet, so identifying stars and solving star patterns is less precise. With these points in mind, the success rate of the final sensor design will likely be higher.

<i>Star Tracker Functionality Test Plan</i>	
<b>Test Description</b>	A functional test will be performed on the star tracker mode of the combined versatile attitude sensor in order to verify that the sensor is able to find the right ascension and declination of an image of the stars. The sensor will take images of the night sky, tries to identify the star patterns and outputs the region in space where these stars originate from. If the sensor is properly configured, it should find the coordinates within a second.
<b>Testing Goals</b>	
Primary Goals	- Verify that the sensor module is able to find the right ascension and declination of a star image
Secondary Goals	- Verify that the sensor module algorithm is sufficiently fast
<b>Testing Equipment</b>	
Sensor module	The sensor module that images the stars
Raspberry Pi	A computer unit that controls the sensor module and performs analysis on the images
Laptop	A laptop that powers the Raspberry Pi and keeps track of testing data
Flat table	A flat table to position the sensor on, so that it points up towards the sky
Dark environment	The sensor should have an unobstructed view to the night sky on a clear night. For this experiment, a local observatory was used where light pollution is limited
<b>Test Setup</b>	
Layout  1. Sensor module 2. Raspberry Pi 3. Laptop 4. Night sky	<p>The diagram illustrates the experimental setup. A laptop (labeled 3) is connected via a cable to a Raspberry Pi (labeled 2). The Raspberry Pi is connected to a sensor module (labeled 1) which is placed on a flat surface (table). The sensor module is tilted upwards at an angle of 89.5 degrees. The sensor's field of view is directed towards the night sky (labeled 4), which contains a constellation of stars.</p>
	The sensor is placed flat on the table, pointing towards the night sky The Raspberry Pi controls the sensor and analyses the images taken The experiment should be carried out on a clear night, with no clouds in sight.
<b>Testing Steps</b>	
	<ol style="list-style-type: none"> <li>1 Configure the test setup</li> <li>2 Take dark frame for noise reduction</li> <li>3 Take an image of the night sky</li> <li>4 Let the sensor process the image</li> <li>5 Store the estimated coordinates of the image</li> <li>6 Continue to the next image</li> <li>7 Repeat steps 3-6 until 50 images have been taken and analysed</li> <li>8 Repeat the test for different sensor configurations</li> </ol>
<b>Testing Criteria</b>	
	The test has been successfully performed when:
	1 The sensor was able to resolve 40 out of 50 star images successfully
	2 The sensor was able to operate at a speed of at least 1 Hz

## 6.1.1.2 Performance test

The test plan for testing the star tracker mode can be seen in Appendix B. The primary goal is to determine its accuracy and the secondary goal is to measure the power consumption of the combined sensor. The test setup is similar to that of the functionality test, but it will be placed on a platform with adjustable feet, so that the sensor pointing can be done accurately. This platform is shown in Figure 6.1. Any misalignments here carry over into the error of the sensor, so it is important to setup the platform using a spirit level. It is determined that the maximum error here is  $0.03^\circ$ , which is based on the accuracy listed by the manufacturer of the spirit level, 0.5 [mm] error per meter. The algorithm showed an error of  $0.05^\circ$ , as mentioned in section 5.3. An extra error of  $0.1^\circ$  is estimated for other variables. These errors are taken into account when analysing the results from the performance test. Once an image is taken, an algorithm will analyse the stars in the picture and will output the coordinates of the image. The difference between the estimated position of the stars and their actual position is the accuracy of the sensor.

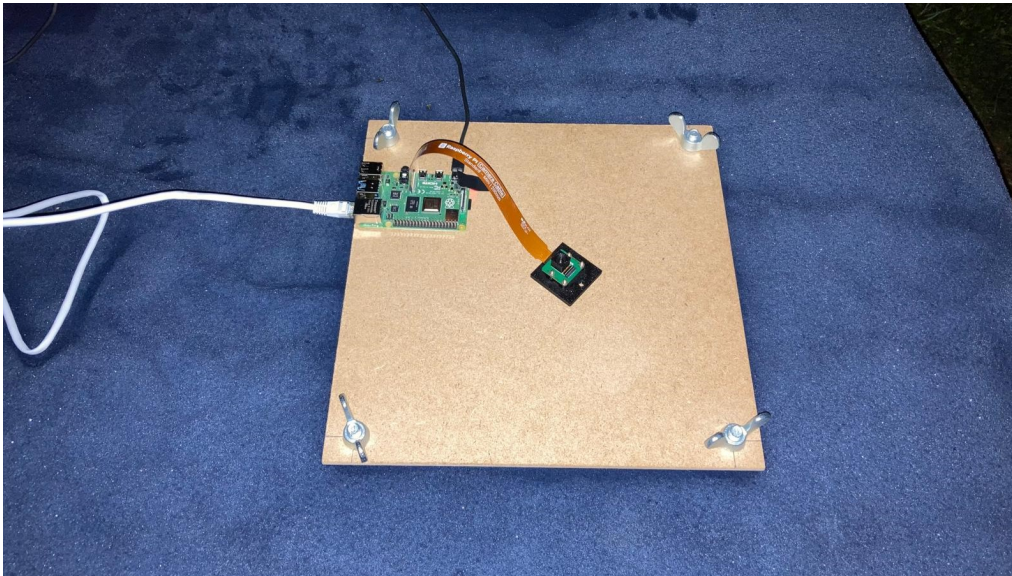


**Figure 6.1:** The sensor module is placed on a platform that can be levelled, so that it points accurately towards zenith.

A statistical method was used to calculate the sample size required for the accuracy determination test. The margin of error  $E$  was set at  $0.02^\circ$ , which is two orders of magnitude more accurate than the target requirement of  $2.0^\circ$  and comparable to the accuracy of currently available COTS star trackers. From the previous paragraph, it was concluded that the expected standard deviation  $\sigma$  is  $0.18^\circ$ . Then, it was decided that this experiment should be performed with a 95% confidence level so that this experiment is 2-sigma reliable. Using Equation 6.2, at least 300 measurements are required to achieve this.

$$n = \left( \frac{Z \cdot \sigma}{E} \right)^2 \quad (6.2)$$

However, not every measurement will be analysed, as the sensor does not have a perfect success rate. It is expected the sensor will have a success rate of at least 80%, which means 240 images will be successfully solved. This brings the margin of error to  $0.023^\circ$ . To account for inaccuracies in this method and for simplicity, this margin of error will be set to  $0.025^\circ$  for the rest of this research. Even more measurements would improve the testing margin of error, but due to time constraints the target has been set at 300 measurements. Details on how the sensor will analyse the pictures is given in section 5.3. During the test, a voltage and current meter will be installed on the power supply lines of the sensor in order to measure the power consumption.

Testing takes place in several steps. First, the test setup will be configured, calibrated and levelled. The exact GPS coordinates of the test setup and time of day of each measurement must be noted down accurately, so that the exact zenith coordinates can be determined. Then, the sensor begins a sequence of taking 10

images and processes them immediately. While the sensor is capturing the images, the power consumption is recorded. Once the images are captured and processed, the mean and the standard deviation of the 10 images are calculated. Then, there should be a pause of a minimum of 4 minutes, which allows for the night sky to shift a whole degree and will make the next measurement set contain different star patterns. This is continued until a total of 30 measurement sets have been completed, for a total of 300 images taken. The sensor returns spherical coordinates of the estimated position of the images, which are compared to the known position of zenith.

The sensor passes the test if its 1-sigma accuracy is better than 2.0 degrees, which is derived from *CVAS-PROTO-07*. In addition, the power consumption of the sensor needs to be below 70 [mW], as specified in *CVAS-FLR-09*. However, this is a requirement specific to the flight-ready sensor and not to the prototype.

## 6.1.2. Sun sensor test plan

Similarly to the star tracker, the Sun sensor will be tested on functionality and performance. The functionality test has the aim to determine whether the combined versatile attitude sensor is able to determine the direction of the Sun vector, while operating sufficiently fast. The performance test will focus on determining the accuracy and power consumption of the sensor. The following sections will explain the methodology for these tests, while the test plans can be viewed in Appendix B.

### 6.1.2.1 Functionality test

The primary goal of this test is to verify that the sensor module is able to determine the direction of the Sun vector while in the Sun sensor mode. This serves as a verification test for requirement *CVAS-PROTO-01*. Its secondary goal is to verify that the Sun sensor mode is able to operate at at least 5 [Hz], which is in line with *CVAS-PROTO-08*. To achieve this, the combined sensor is placed on a rotating platform in front of a light source that simulates the Sun. This light is projected onto the sensor, from which the sensor can calculate the direction of the Sun vector. The test setup can be seen in Figure 6.2.

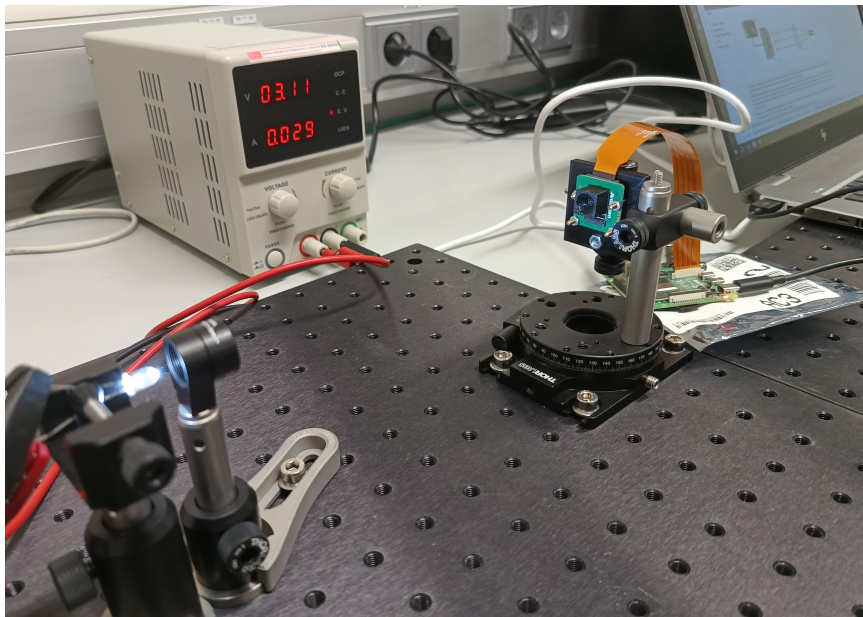
Like the star tracker tests, the Sun sensor test should take place in a dark room, so that the only light source is the lamp. This lamp should approximate sunlight by operating on wavelengths similar to the Sun. Its light intensity should match that of the Sun when 1 AU away from the Sun, which is roughly 1361 [ $W/m^2$ ]. In addition, the lamp should have an angular diameter of  $0.5^\circ$ , which is comparable to the size of the Sun seen from Earth. More information on the process of finding a suitable light source can be found in subsection 6.1.2.3.

In case light reflects from the sensor and lights up the dark room, extra padding could be positioned in the room to block this out. This ensures that the quality of the experiment is preserved. The sensor itself is placed on rotating platform that can be easily and accurately turned horizontally into different angles. Also attached to the sensor is a mechanism to turn the sensor vertically. With such a system, the sensor can be tested for different incidence angles, which allows the entire FOV of the sensor to be investigated.

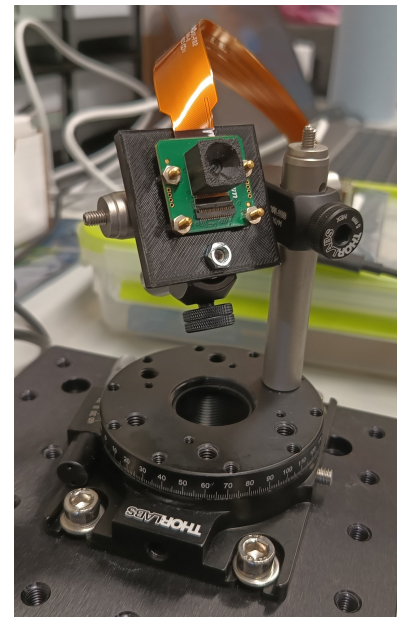
The test takes place in the following steps. First, the setup is calibrated with a default  $0^\circ$  incidence angle. Then, the sensor is positioned in a new angle and the sensor tries to calculate the direction of the Sun vector. This is repeated until 5 angles have been analysed. The sensor has passed the test if it correctly found the Sun vector in 40 out of 50 measurements and did so at an update rate of 5 [Hz]. The method for selecting a sample size of 50 measurements is similar to the one presented in subsection 6.1.1.1.

### 6.1.2.2 Performance test

The performance test of the Sun sensor mode has the primary goal to determine the accuracy of the sensor, while it determines the power consumption as a secondary goal. The test setup does not differ from the functionality test, except for the placement of voltage and current probes onto the sensor, and for the distance between the sensor and the light source. The voltage and current probes help to monitor the power consumption during the test.



(a) Test setup for the Sun sensor functionality test. The LED is positioned just in front of a lens, who combines the light towards the sensor.



(b) Sensor module installed onto a rotating platform.

**Figure 6.2:** Overview of test setup elements for the Sun sensor tests.

The test consists of taking images with different Sun incidence angles. Measurements will be taken for azimuth angles ranging from  $-35$  to  $+35$  degrees, while elevation angles range from  $-20$  to  $+20$  degrees. These measurements are spread out across the entire FOV of the sensor. The rotating platform can be used to quickly change the incidence angle for each image, so that the entire FOV of the sensor is covered during the test. After each measurement set, the power consumption should be noted down.

Initial calibration tests showed that the sensor had a standard deviation of  $0.06^\circ$  or lower. For this test, the accuracy needs to be estimated with at least a precision of  $0.1^\circ$  and a confidence level of 95%. Using Equation 6.2, a total of 2 measurements should be enough. However, this number was increased to 10, since taking measurements can be done in quick succession. This makes the performance test have a precision of up to  $0.05^\circ$  instead, or  $0.1^\circ$  with a 99.7% confidence level.

For this test there are two criteria for success. The first is that the sensor needs to be able to identify the Sun vector with a 1-sigma accuracy of  $5.0^\circ$ . This would make it compliant with *CVAS-PROTO-06*. The second criteria is that the power consumption should not exceed 70 [mW], which is in line with *CVAS-FLR-09*.

### 6.1.2.3 Light source selection

A light source should be found that emits light similar to that of the Sun. Commercially available light sources are often not strong enough to provide the  $1361 [W/m^2]$  intensity at an angular diameter of  $0.5^\circ$ . The larger a light source, the further away it needs to be placed from the sensor in order to achieve the target angular diameter, which severely decreases its intensity. Therefore, the simplest method would be to find a small light source and place the sensor close to it. Several options were investigated.

A bright LED torch was considered that could vary its beam angle to  $20^\circ$ . However, the torch had a diameter of 11 [mm], which required the torch to be placed at 1.260 [m] from the sensor. At that distance, the 1.375 [W] torch would only yield an intensity of  $8.4 [W/m^2]$ . A smaller 5 [mm] LED was found with an output power of 0.120 [W] and a beam angle of  $15^\circ$ , which at the time of writing was one of the most powerful narrow-angle LEDs available. Due to its smaller size, it only has to be placed 0.573 [m] from the sensor, but its intensity was only  $6.3 [W/m^2]$ . Powerful lasers were considered, as these proved to be capable of providing the right intensity and angular diameter. However, lasers only output light at a specific wavelength, so there would be

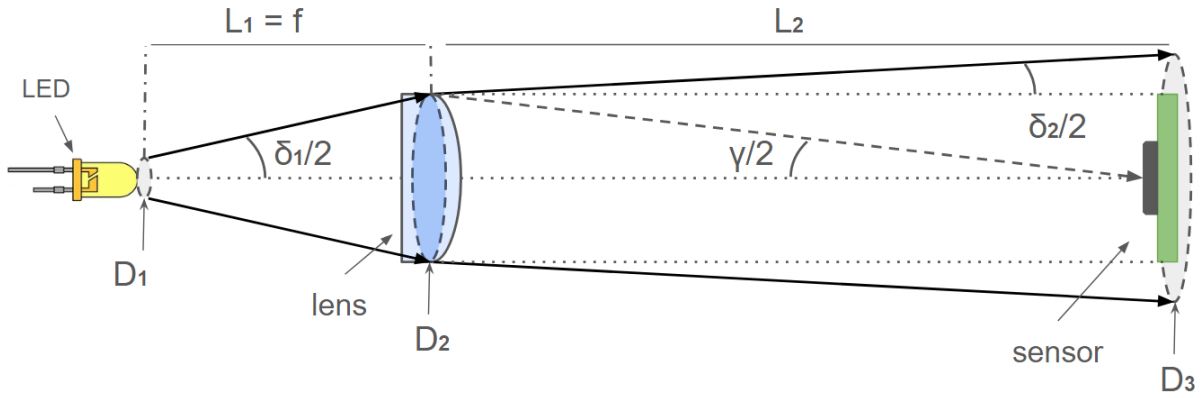


Figure 6.3: Schematic overview of LED light collimated through a lens.

a larger discrepancy between the spectrum of the Sun and the test setup. Furthermore, the lasers required special training and facilities in order to operate them. Therefore, lasers were not selected.

Subsequently, the use of lenses to collimate light to the sensor was considered. Collimating light from the 5 [mm] LED would result in smaller intensity losses, as the light spreads out less over time. A schematic overview of the setup is shown in Figure 6.3. A plano-convex lens is placed in front of the LED such that the LED sits in the focal point of the lens. This ensures good collimation of the light. The intensity and angular diameter of the light in this setup were approximated with the equations that follow. First, the intensity of light at the LED was calculated using the properties of the LED.

$$I_1 = \frac{P_{LED}}{A_1} \quad (6.3)$$

Then, the diameter of the light spot on the lens was calculated using the beam angle,  $\delta_1$  and the distance to the lens,  $L$ , from which the flux at the lens could be determined. Since the light is being collimated,  $L_1$  is equal to the focal length  $f$  of the lens.

$$D_2 = D_1 + 2 \cdot L_1 \cdot \tan\left(\frac{\delta_1}{2}\right) \quad (6.4)$$

$$I_{lens} = \frac{P_{LED}}{A_2} = \frac{P_{LED}}{\frac{\pi D_2^2}{4}} \quad (6.5)$$

Here, the lens has the goal to collimate the light towards the sensor. It was assumed that the beam angle is reduced from  $15^\circ$  to  $0.5^\circ$ . This was taken as a reference value and is not related to the incidence angle that is being targeted. Instead, this divergence angle is deemed feasible with the available setup and budget. The possibility for an even lower incidence angle also exists, which would increase the light intensity on the sensor further. Using the reference divergence angle of  $0.5^\circ$ , the diameter of the light spot on the sensor can be calculated using Equation 6.4, from which the flux on the sensor follows using Equation 6.5. Here, a length  $L$  from the lens to the sensor can be chosen as a design parameter. It should be noted that in these calculations, no additional losses from interaction with air particles was considered, and therefore the actual intensity levels will be slightly lower. The incidence angle of light,  $\gamma$  can be calculated through Equation 6.6. Since the lens magnifies the LED relative to the sensor, the apparent size of the LED on the lens has been used.

$$\gamma = 2 \cdot \text{atan}\left(\frac{D_2}{2L}\right) \quad (6.6)$$

This incidence angle  $\gamma$  can be used to determine the accuracy error induced by the light to the sensor. The number of pixels covered by the incidence angle can be calculated using the focal length and pixel size of the sensor, which are 2.35 [mm] and 3.0 [ $\mu\text{m}$ ] respectively. Equation 6.7 shows the error expressed in number of pixels. Then, this can be converted to an induced error angle using the resolution in degree/pixel for the sensor, which was 0.0593 [ $^\circ/\text{pixel}$ ] for a 640x400 resolution setting. It should be kept in mind that a 2x2 binning mode is used in this setting, so the pixel size and accuracy per pixel are doubled.

$$\text{Induced error [pixels]} = f \cdot \frac{\tan(\gamma)}{\text{pixel size}} = 2.35 \cdot \frac{\tan(\gamma)}{2 \cdot 0.003} \quad (6.7)$$

$$\text{Induced error [}^\circ\text{]} = \text{Induced error [pixels]} \cdot 2 \cdot 0.0593 \text{ [}^\circ/\text{pixel]} \quad (6.8)$$

Doing these calculations for the 0.12 [W] LED and a plano-convex lens with a focal length of 14.9 [mm], it was found that there does not exist an LED and lens configuration where both the intensity and incidence angle at the sensor are as desired. An overview of the results can be seen in Table 6.2. However, the setup can be altered such that either the intensity level or the incidence angle is correct. In case of the former, a flux of around 1361 [ $\text{W}/\text{m}^2$ ] could be achieved by placing the sensor at a distance of 0.191 [m] from the lens, which would give an incidence angle of 2.68 $^\circ$ . In case of the latter, the sensor would be placed at a distance of 1.023 [m] from the lens, which would give a flux of only 479 [ $\text{W}/\text{m}^2$ ]. With this in mind, it was decided to use the setup with the 0.5 $^\circ$  incidence angle for the accuracy tests, as here the incidence angle creates an induced error of only 0.41 $^\circ$ , which is an order of magnitude lower than the target 5.0 $^\circ$  accuracy for the prototype Sun sensor. It is also the incidence angle that is expected when in orbit. Therefore, its impact on the accuracy testing is acceptable. The higher intensity setup will be used in the functionality test, as it represents the intensity of the Sun in space around Earth.

**Table 6.2:** Intensity and incidence angle calculations for two different light source setups.

Properties	Correct intensity	Correct incidence angle	Units
LED Diameter	0.005	0.005	m
Beam angle	15	15	degrees
Power	0.12	0.12	W
Flux at LED	6,112	6,112	$\text{W}/\text{m}^2$
Focal point lens	0.0149	0.0149	m
Flux at lens	1,919	1,919	$\text{W}/\text{m}^2$
Divergence angle	0.5	0.5	degrees
Distance to lens	0.191	1.023	m
Flux at sensor	1,361	479	$\text{W}/\text{m}^2$
Incidence angle	2.68	0.50	degrees
Induced error	2.17	0.41	degrees

### 6.1.3. Baffle effectiveness test plan

The newly design baffle was planned to be tested on its effectiveness to keep stray light away from the sensor's lens. A more effective baffle allows the sensor to take pictures of the stars with less noise and with more stars visible. The test would have been performed with almost the same test setup as the star tracker tests, but with an additional light source that emulates stray light from the Sun.

The sensor will be placed in front of a monitor again, but now a single star image is displayed throughout the entire test. The light source, which is the bright LED torch mentioned in subsection 6.1.2.3, is placed 1 [m] to the side of the sensor, so that a stray light angle of 180 $^\circ$  is created. The star tracker analyses the image as usual and after every measurement the lamp is placed 5 degrees closer to the front of the sensor. This is repeated until the lamp is in the field-of-view of the sensor and a stray light angle of 60 $^\circ$  is reached. As the test progresses, the images taken by the sensor should gradually become more bright as stray light enters

the sensor, which makes the stars more difficult to identify. The test is repeated for a sensor with and without baffle.

The test is successful when the accuracy of the sensor has been derived from measurements with stray light angles from inside and outside its FOV. The image quality between the tests with and without baffle can be compared to determine the effectiveness of the baffle.

## 6.2. Results

The tests were performed and their results can be seen in the sections below. The results are compared to the testing criteria of test, so that it can be verified if a test was successful or not. The results of the star tracker functionality test and performance test are detailed in subsection 6.2.1 and subsection 6.2.2. For the Sun sensor tests, these can be seen in subsection 6.2.3 and subsection 6.2.4.

### 6.2.1. Star tracker functionality test

The first part of the star tracker testing consisted of tuning the sensor settings such that stars were clearly visible in the images. This constituted of adjusting the exposure time and analogue-gain values and of creating dark images for noise reduction. During the tests, it was recorded how many images were correctly solved and how much time it took to solve. The camera settings selected in this test can be found in Table 5.1. An extra long exposure time of 1.000 [s] was also tested in order to observe how the sensor would operate with settings that exceed the requirements. The results are presented in Table 6.3 and visualised in Figure 6.4 and Figure 6.5.

**Table 6.3:** Results of the star tracker functionality test using different exposure and analogue gain settings.

Exposure Time [s]	Analogue Gain	# solved	Fraction solved [-]	Average solving time [s]
0.200	8.0	-	-	-
0.200	10.0	-	-	-
0.200	12.0	-	-	-
0.300	8.0	17	0.34	5.522
0.300	10.0	27	0.54	4.658
0.300	12.0	38	0.76	4.327
0.400	8.0	29	0.58	6.989
0.400	10.0	38	0.76	4.634
0.400	12.0	44	0.88	4.290
0.500	8.0	25	0.50	4.647
0.500	10.0	40	0.80	4.562
0.500	12.0	45	0.90	4.267
1.000	8.0	16	0.32	4.389
1.000	10.0	41	0.82	4.478
1.000	12.0	48	0.96	4.301

#### 6.2.1.1 Success rate

An exposure time of 0.200 [s] was too short to create consistently clear images of the night sky. The algorithm struggled too often with these images, since the faint stars could not be distinguished from the background noise. Despite noise reduction algorithms, only a handful of images were successfully solved. After 10 unsuccessful images with solving times above 30 [s], it was decided to stop testing with that exposure setting and to continue to longer exposure times. From 0.300 [s] the stars became visible enough to be solved by the algorithm. With an analogue gain (AG) of 8.0, around a third of the images were solved at an average solving

time of 5.5 [s]. Increasing the analogue gain yielded significant improvements in the success rate, as the fraction solved increased by 20 percent-points by increasing the analogue gain from 8.0 to 10.0. Increasing further to 12.0 gave similar results. Initially, it was thought that higher analogue gains would introduce too much noise to the images, but basic filtering techniques were enough to prevent this from happening.

At exposure times of 0.400 [s] the sensor first met the 80% success requirement using an analogue gain of 12.0. With these settings, the sensor had an 0.88 success rate, but lower gain values did not meet the requirement. Increasing the exposure time further to 0.500 [s] saw both the AG10 and AG12 settings pass the test, but a decrease in success rate on the AG8. Upon investigating the images taken by the sensor, it appeared that the gain setting was too low for the stars to clearly stand out from the background noise. This caused the star tracker algorithm to mistake noise pixels for stars, which made identifying star patterns harder. On the other hand, increasing the exposure times to 1.000 [s] only saw a limited improvement in success rate for the two highest gain settings, as seen in Figure 6.4. Still, the AG12 setting was able to solve 96% of the images taken, which shows that this prototype is able achieve availability rates that are sufficient for space applications.

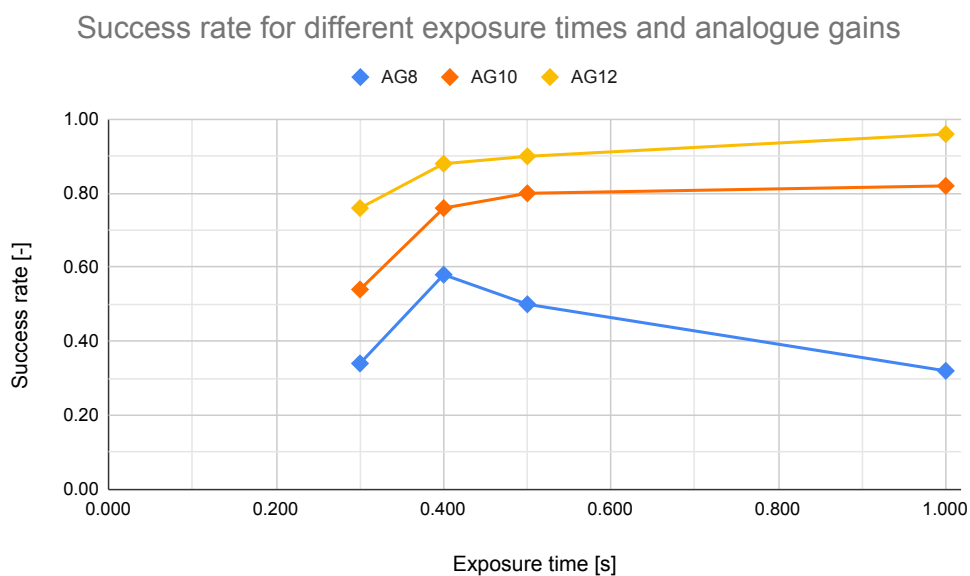


**Figure 6.4:** Sun sensor success rate for different analogue gain and exposure time settings.

### 6.2.1.2 Solving times

In terms of average solving times, the algorithm was able to solve the images between 4.0-5.0 [s]. The solving times for each setting are displayed in Figure 6.5. Higher analogue gains improved the solving times slightly, with AG12 being roughly 0.3 [s] quicker than AG10. With the lowest analogue gain value the sensor struggled to solve the images. At an exposure time of 0.400 [s], the solving times were almost 7.0 [s], compared to 4.6 [s] and 4.3 [s] for AG10 and AG12 respectively. This could be explained by the aforementioned noise pixels being picked up as stars. When that happens, the algorithm has more 'stars' to process, which increases processing times. And all these noise pixels will not yield correct star patterns, so the algorithm has to run more verification tests. Still, it has been mentioned before that the solving times are not fully representative of the final processing capabilities of the sensor, since the hardware and software will definitely change in future designs.

### 6.2.1.3 Star visibility

Considering the results of the functionality test and the exposure time limit of 0.500 [s], it was decided to select the settings with an exposure time of 0.500 [s] and analogue gain of 12.0. With these settings, the sensor

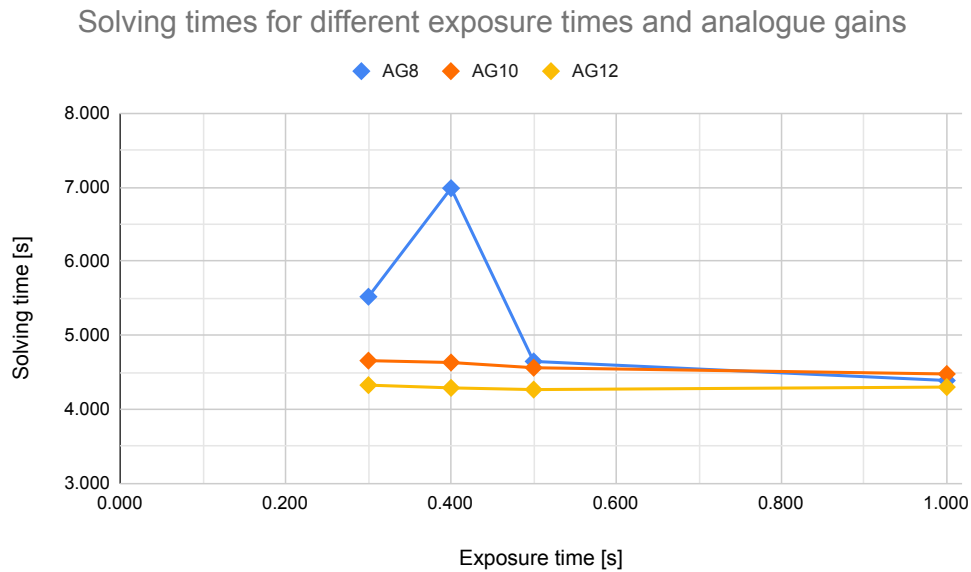


**Figure 6.5:** Sun sensor solving times for different analogue gain and exposure time settings.

should have a 90% success rate and average solving time of 4.267 [s]. Figure 6.6 shows an post-processed image taken with these settings that was successful solved by the algorithm. The brightness, contrast and sharpness of this image was altered, so that the stars are better visible for the reader of this document. This step is not performed on the sensor itself. Figure 6.7 shows a zoomed-in portion of the same image, but with stars and constellations annotated.

A few bright stars with a magnitude of 3.0 or better can be seen that make up parts of Cassiopeia, Andromeda and Perseus. In the middle of the image is a faint triangle visible, of which the top-most star is a called *3 Persei - HIP 9222*. This is a magnitude 5.70 star, which indicates that the sensor might able to image stars that are fainter than the in subsection 4.4.2 anticipated 4.70 magnitude. This would be good news for the number of stars that can be used for attitude determination. However, this star was positioned in the centre of the sensor's FOV and directly overhead in the night sky, which could have helped with its detection. The edges of the sensor's FOV contain fewer stars than the centre, so in practice not all 5.70 magnitude stars or similar will be detectable.

There also exist pixels in Figure 6.6 that cannot be linked to an existing star. These pixels are likely caused by noise pixels close together and appearing as a single star. Better filtering algorithms or different sensor settings could resolve this. Still, the star tracker algorithm runs several checks on its patterns to verify that the patterns identified are correct. This allows imperfect pictures to be resolved, but it adds computational load.

#### 6.2.1.4 Test conclusions

The star tracker functionality test has shown that there exist several sensor modes where the success rate exceeds 80%, but the sensor cannot operate at 1 [Hz] in the current configuration. Therefore, the test is a partial success, although alterations to the processing hardware and star tracker algorithm could improve the computational speeds in future designs. With this in mind, an exposure time of 0.500 [s] and analogue gain of 12.0 were chosen and subsequently used in the performance test, as these settings yielded the highest solving success rate within the constraints of the design.



**Figure 6.6:** De-noised and post-processed image of the stars with 0.500 [s] exposure time and analogue gain of 12.0. The Cassiopeia constellation is visible just right of the centre.

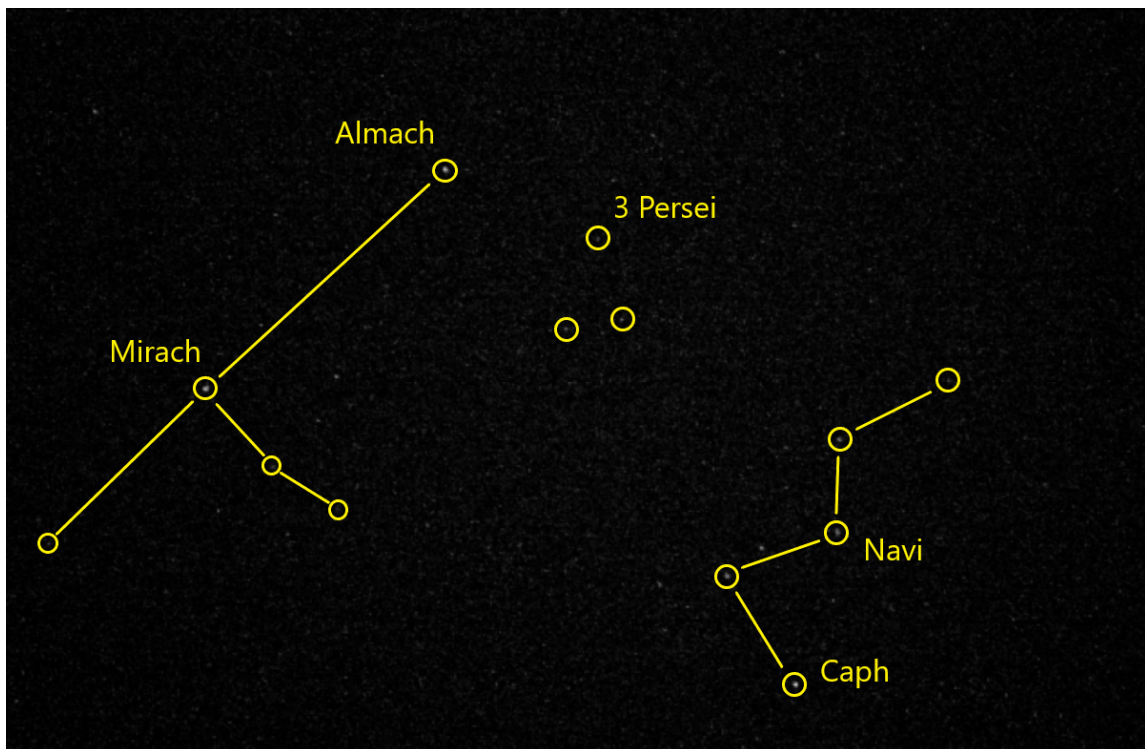


**Figure 6.7:** Zoomed-in image of the 3 Persei - HIP 9222 star and its surrounding stars and constellations. Cassiopeia and part of Andromeda have been drawn out, together with the names of their brightest stars.

## 6.2.2. Star tracker performance test

The second part of the star tracker testing focused on determining the accuracy and power consumption of the sensor. This test was performed on with a clear night sky at the observatory. The goal was to take 30 measurement sets of 10 images, but only a 27 sets could be carried out due to a low laptop battery. The final sets of measurements were taken later that night, but bad lighting conditions severely worsened the image quality. The average error in right ascension, declination and angular error are presented in Table 6.4, as well as the standard deviation and success rate of these measurements. The performance of the star tracker during the testing night can be seen in Figure 6.8. A 45-minute break took place halfway through the measurements, which explains the lack of measurements around 22:00 hours.

**Table 6.4:** Accuracy results of the star tracker performance test. The error values contain both the mean error and the 1-sigma standard deviation.

RA error [deg]	Dec error [deg]	Angular error [deg]	Images solved [-]	Success rate [-]
0.937 +- 0.096	2.573 +- 0.053	2.641 +- 0.051	266	0.985

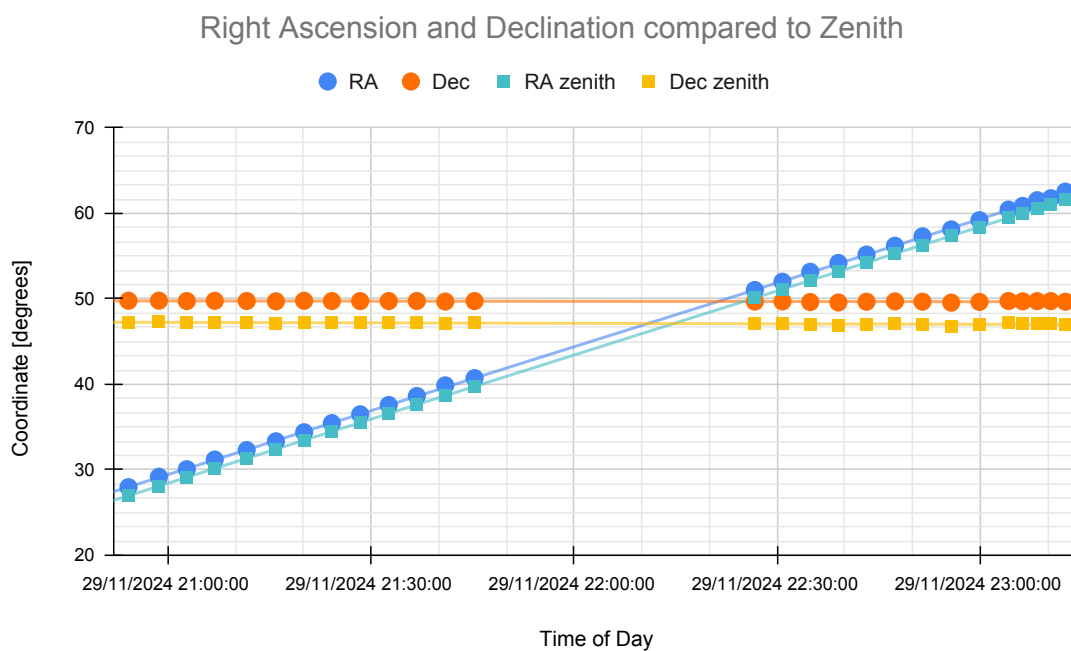


**Figure 6.8:** The right ascension and declination found by the star tracker mode, compared to the actual position of Zenith at that time of day.

### 6.2.2.1 Accuracy

Of the 270 images taken, a total of 266 images were correctly solved. This leads to a 98.5% success rate for these sensor settings, which is even higher than the results of the functionality test. Despite not taking 300 images, the sensor solved more than the 240 images that was aimed for. The four images that were unsuccessfully solved, were spread throughout the measurements and did not happen during the same set of measurements. One cause for these images being unsuccessful could be a noise pattern interfering with the stars in an unfavourable way, which caused the algorithm to misidentify some stars.

In terms of accuracy, the sensor appears to have a distinct bias in angular error of  $2.641^\circ$ , as observed from the angular error in Table 6.4. This bias is also visible in Figure 6.8, which shows a consistent bias in right ascension of  $0.937^\circ$  and a bias of  $2.573^\circ$  in declination. Despite this bias, the sensor has a 1-sigma standard deviation in angular error of only  $0.051^\circ$  with a margin of error of  $0.025^\circ$ , which is almost 40 times more

accurate than requirement *CVAS-PROTO-07* and 4 times more accurate than *CVAS-FLR-07*. The sensor exceeds its expectations regarding accuracy significantly.

The bias could be caused by misalignment of the sensor and lens on the PCB. Upon inspection, the sensor appears to be tilted in reference to its PCB, which went unnoticed before the tests. The PCB itself was bolted into a 3D printed bracket and placed onto a levelled bed. The accuracy here is limited by the accuracy of the spirit level, which is  $0.03^\circ$ . The star tracker algorithm has been tested thoroughly and did not show this bias when using images from Stellarium. After the performance tests were completed, more images were taken of the night sky, but with the sensor rotated  $90^\circ$ . This flipped the biases in right ascension and declination, but still an angular error of  $2.6^\circ$  was observed. Therefore, the bias is most likely caused by the misalignment of the sensor in reference to the PCB and not by software errors.

### 6.2.2.2 Power consumption

The power consumption of the sensor was measured using accurate voltage and current meters. With the exposure time and analogue gain of 0.500 [s] and 12.0 respectively, a voltage of 3.287 [V] and current of 21.92 [mA] were observed. This brings the power consumption in the star tracker mode to 72.05 [mW]. This is slightly above the design requirement of 70 [mW] and therefore it fails the test. Again, this is just the power consumption of the sensor itself as the computational power is excluded.

### 6.2.2.3 Test conclusions

On-earth performance testing of the star tracker showed that the star tracker is much more accurate than anticipated, but consumes a fraction too much power. When the  $2.6^\circ$  bias, which is likely caused by a misaligned sensor on the PCB, is removed, the sensor shows an accuracy of  $0.051^\circ$  with a margin of error  $0.025^\circ$ . The power consumption was measured to be 72.05 [mW], which results in a partial success of the star tracker performance test.

## 6.2.3. Sun sensor functionality test

The functionality test of the Sun sensor mode had the goal of determining whether the sensor can operate as a Sun sensor and whether it can do so with sufficient speed. After the experiment was set up, it was clear that the divergence angle of  $0.5^\circ$  could not be reached. Upon inspection, a divergence angle of  $6.7^\circ$  was found, which lowered the intensity to  $156 [W/m^2]$  instead. This could be solved by positioning the sensor closer to the lens, but this would make the light source take up most of the FOV of the sensor. Since this would make the test less representative, it was decided to continue with the original lens-to-sensor distance. The results of the functionality test are shown in Table 6.5.

**Table 6.5:** Results of the Sun sensor functionality test.

Azimuth [deg]	Elevation [deg]	Azimuth found [deg]	Elevation found [deg]	Azimuth Error [deg]	Elevation Error [deg]	Angular Error [deg]
10	0	10.669	0.15	0.669	0.15	0.686
20	0	21.323	0.598	1.323	0.598	1.452
0	10	-0.297	10.198	-0.297	0.198	0.353
0	20	-0.891	22.997	-0.891	2.997	3.110
-20	-20	-21.66	-24.72	-1.66	-4.72	4.963

### 6.2.3.1 Success rate and solving times

During the test, all images were successfully resolved and the coordinates of the Sun spot were found. This was done at an average solving time of 0.039 [s], which is faster than the 0.200 [s] that was required for this test. Similar to the star tracker tests, the sensor PCB and microcontroller will likely change, so the solving

times are different compared to the final sensor design. Still, there is a significant amount of margin to also increase the update rate to 10 [Hz], which is the target update rate for the flight-ready sensor.

### 6.2.3.2 Sun spot deformations

When comparing the Sun spots of large incidence angles to Sun spots in the centre of the sensor's FOV, the spots are more oval-shaped near the edges, instead of a circle. This can be observed in Figure 6.9, which was an image taken with an azimuth and elevation angle of  $(-20^\circ, -20^\circ)$ . This is in line with what was found in Antonello et al., who observed that this is caused by the effect of the cosine of the incidence angle at low elevations [12]. The oval-shape provides a challenge for the Sun spot algorithm and it could introduce errors in the attitude determination, as the algorithm struggles to find the center of the Sun spot. Luckily, these effects should remain constant and predictable, but it still causes inaccuracies at the edges of the Sun sensor's FOV.

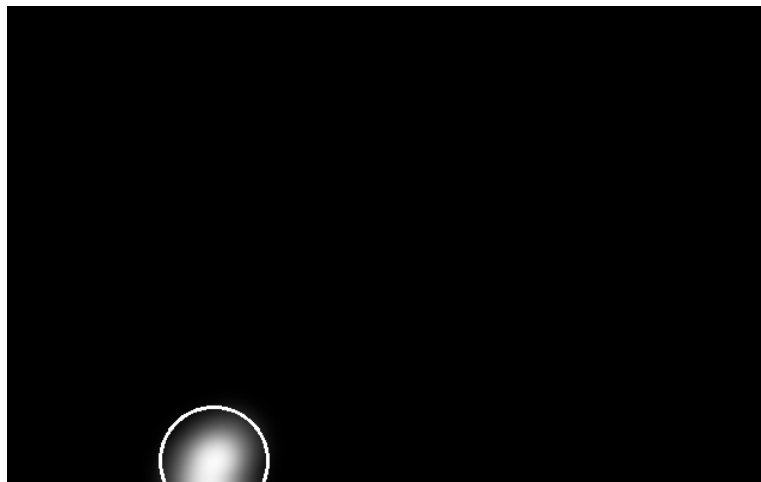


**Figure 6.9:** An oval-shaped Sun-spot is present at large azimuth and elevation angles.

Since the light hitting the sensor is very intense, scattering of the light inside the lens can be visible. This appears as flares and spikes on the images, which negatively affects the accuracy of the sensor. Gaussian filters reduce these effects somewhat, but they can still result in a shift of the Sun spot location. When this was observed, the exposure settings of the sensor mode were lowered. This caused less light to appear in an image and it significantly reduced the Sun spot deformations.

### 6.2.3.3 Test conclusions

The Sun sensor mode successfully passed the functionality test. It showed that it could find the Sun sensor in more than 80% of the images, as 100% of the images were solved. The sensor was sufficiently fast for operation at 5 [Hz] and with a comfortable margin.

### 6.2.4. Sun sensor performance test

The aim of the Sun sensor performance test was to determine the accuracy and power consumption of the combined sensor in the Sun sensor mode. A total of 77 sets of 10 images were taken spread across the FOV of the sensor. The angular error of each measurement was calculated and used to find the mean angular error at a specific point in the sensor's FOV. This way, a map of the angular error for different azimuth and elevation angles can be made, which gives a visual representation of the sensor's accuracy. This map can be seen in Figure 6.10.

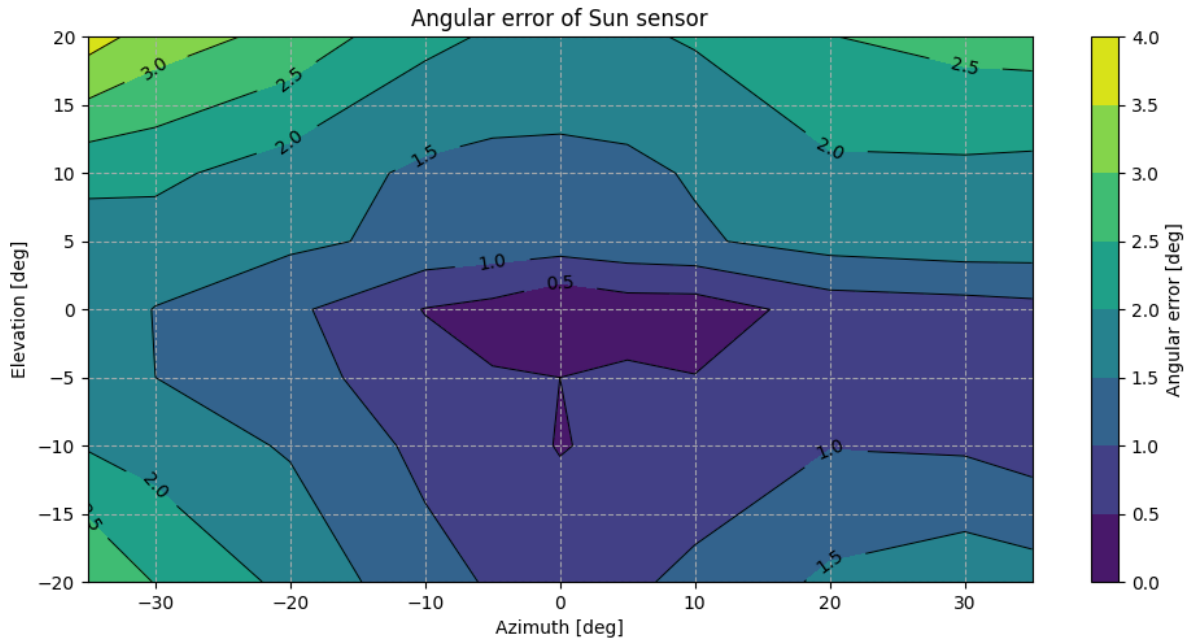


**Figure 6.10:** Angular error of the Sun sensor in relation to azimuth and elevation angles.

#### 6.2.4.1 Accuracy

From the figure it can be observed that the sensor is most accurate in its centre and loses accuracy when the Sun spot is near the edges. Within  $\pm 5^\circ$  from the centre, the sensor is as accurate as  $0.5^\circ$  or better with a margin of error of  $0.05^\circ$ . Most of the FOV has an angular error below  $5^\circ$ , but at azimuths larger than  $\pm 20^\circ$  and elevations higher than  $\pm 15^\circ$  angular errors of more than  $3.0^\circ$  are observed. It should be noted that the FOV of the sensor is slightly wider than what can be seen in Figure 6.10, so the angular error at the very edge of the FOV is marginally larger than what is visible here.

The map is not perfectly symmetric, as there appears to be a difference in accuracy for positive and negative elevation angles and positive azimuth angles have a better accuracy. These are likely caused by errors in the experimental setup. Selecting the azimuth angles could be done with an accuracy of  $\pm 5$  [arcmin] ( $0.083^\circ$ ) using an accurate rotating stage from ThorLabs. However, such a stage was not available for setting up the elevation angle. Therefore, the accuracy in the experimental setup is predicted to be  $\pm 0.5^\circ$ . It could also be that due to imperfections in the lens and CMOS surface the accuracy pattern of the sensor is not fully symmetric.

#### 6.2.4.2 Power consumption

During the accuracy test, the voltage and current drawn by the sensor was measured. With an exposure time of 0.400 [ms] and resolution of 640x400 [pixels], the voltage and current were on average 3.287 [V] and 21.10 [mA] respectively. This results in a power consumption of 69.36 [mW] for the sensor module itself, which is just below the requirement of 70 [mW].

#### 6.2.4.3 Test conclusions

Since the accuracy of the sensor is dependent on the position of the Sun sensor, a definitive accuracy for the entire sensor cannot be given. However, it can be concluded that the Sun sensor mode meets the target 1-sigma accuracy of  $5.0^\circ$ , as it showed an accuracy between  $0.5^\circ$  and  $3.0^\circ$  throughout its FOV, with a  $0.05^\circ$  margin of error. During the test, a power consumption of 69.36 [mW] was observed. Therefore, the Sun sensor mode has successfully passed the performance test.

# Discussion

In the previous chapter, the combined versatile attitude sensor was tested for functionality and performance. The sensor passed most of the tests and where it failed the margins were close. The accuracy of the sensor meets the requirements in both sensor modes with a comfortable margin. In this chapter, the results of the tests will be discussed in further detail. The methodology will be critically analysed for mistakes or inaccuracies that had an effect on the test results. It will also be investigated what has not been done in this thesis and what might be worth pursuing in the future.

This chapter is build up in the following way. First, the results of research are discussed in section 7.1. Then, the test setups and experimental procedures are reflected upon in section 7.2. Finally, section 7.3 investigates which parts of the design have not been tested yet and must be addressed in future research.

## 7.1. Discussion of results

The functionality tests performed on both the star tracker and Sun sensor mode prove that the sensor can operate in both modes using the same hardware. The star tracker mode had a solving success rate of at least 90% when using an exposure time of 0.500 [s] and analogue gain of 12.0. Meanwhile, the Sun sensor mode had a success rate of more than 99%. The design of the combined sensor is mechanically passive, which means it only has to switch software modes in order to change between star tracker and Sun sensor operations. Therefore, requirements *CVAS-PROTO-01*, *CVAS-PROTO-02* and *CVAS-PROTO-03* were fulfilled. And since the prototype was based on a COTS CMOS optical module that is compatible with Raspberry Pi, so was *CVAS-PROTO-10*. Improvements to the sensor software configurations and processing algorithms can improve the success rates even further.

The functionality tests also gave an insight into the update rate and computational load of the different sensor modes. Requirements *CVAS-PROTO-08* and *CVAS-PROTO-09* state that the star tracker mode should operate at a minimum of 1 [Hz] and the Sun sensor mode at 5 [Hz]. Testing showed that this is true for the Sun sensor mode, whose algorithm is relatively simplistic and can be solved in 0.04 [s]. On the contrary, the star tracker did not meet this requirement, as in section 6.2.1.2 it was found that with the current hardware layout, the mode has an average solving time between 4.0 and 5.0 [s]. It should be noted that the test setup is not fully representative for the solving times of the flight-ready sensor, as the computational load and hardware layout of future designs is likely to change. The flight-ready sensor will either feature a dedicated microcontroller or make use of an external computer in order to analyse its images. Computer hardware is becoming more powerful each year, so the computational times can be reduced with new hardware. In addition, the algorithms used for analysing the images have room for improvement. For instance, the Astrometry.net algorithm is too robust for this prototype and outputs a number of figures and equations that are unnecessary for this thesis. It also has a large catalogue of stars that are not visible to this sensor. A dedicated star tracker algorithm that only uses stars visible to the sensor can greatly reduce the computational costs. Improving the star tracker algorithm should be a priority in future designs.

The performance tests were carried out in order to determine the accuracy and power consumption of the sensor. The target accuracy of the sensor modes was set at  $2.0^\circ$  for the star tracker and  $5.0^\circ$  for the Sun sensor. The performance tests were able to determine the 1-sigma accuracy for the star tracker at  $0.051^\circ$  with

a margin of error of  $0.025^\circ$ . For the Sun sensor, this was estimated at better than  $3.0^\circ$  with a margin of error of  $0.1^\circ$  respectively. Thus, requirements *CVAS-PROTO-06* and *CVAS-PROTO-07* are met. For the star tracker mode, a bias of  $2.6^\circ$  was observed, which is likely caused by a misalignment of the sensor's optical module with its PCB. There could also be a mismatch between the coordinate system used by the star tracker and the system for determining the zenith coordinates. This problem should be addressed in future experiments so that the bias can be removed from the flight-ready sensor. Moreover, requirements *CVAS-PROTO-04* and *CVAS-PROTO-05* have not been fully fulfilled. While the accuracy of the sensor modes is good enough, the performance of the sensor has not been tested during slew manoeuvres or tumbling. If the satellite rotates, then the Sun spots and stars can become deformed, which will lower the accuracy or prevent the sensor from operating. This is especially important for the star tracker mode, as this mode has a long exposure time and therefore sees more deformations. In all experiments performed during this thesis, the sensors were fixed in place. Future research should include slew manoeuvre testing using a rotating test setup in order to confirm that the prototype meets these requirements.

The size and power requirements of the flight-ready sensor, *CVAS-FLR-08* and *CVAS-FLR-09*, were dropped for the prototype sensor. The reason for this has been explained in subsection 4.2.2, but the tests results do give an indication of what needs to be changed for the flight-ready design. The CMOS surface and lens combination fits inside the volume allowed by *CVAS-FLR-08* and there is space left for an extended baffle. The PCB does not fit, but this can be changed in future designs. In terms of power consumption, the OV9281 CMOS sensor consumes between 69 and 72 [mW], depending on the update rate of the sensor. Higher update rates lead to a further increase in power consumption. The minimum power consumption of the sensor appears to be limited to 69 [mW] due to overhead processes, so the power consumption of the OV9281 cannot be lowered further. The power consumptions stated here exclude the power consumed by the microcontroller that processes the images. For most COTS attitude sensors that the combined sensor should compete with, image processing is done on a specific microcontroller. The power consumption listed in their data sheets often includes both the power of the sensor and their microcontroller. It will not be possible to bring the power consumption of the combined sensor, including microcontroller, below 70 [mW] without selecting a less power-intensive CMOS sensor and without benefitting from improvements in microcontroller technology. However, there might be a possibility for using a satellite's central processing unit, provided that this processing unit is powerful enough and the analysis does not prohibit the computer from performing critical tasks.

Taking these results into account when comparing the performance and capabilities of the prototype sensor to a combination of individual attitude sensors, a number of conclusions can be made. It is possible to combine a star tracker and Sun sensor into a single sensor using the same hardware. This sensor can operate in both sunlight and eclipse conditions and while tumbling. The combined design is a compromise, as the accuracy of the sensor is generally lower than the individual attitude sensors listed in Table 2.3 and Table 2.2. The accuracy of the star tracker is comparable to the CubeSpace CubeStar, which has a 3-sigma accuracy of  $0.02^\circ$ , while the Sun sensor accuracy can only be compared to simple Sun sensors, such as the NanoSense FSS from GomSpace. That sensor has a 3-sigma accuracy of  $2.0^\circ$ , while most fine Sun sensors have an accuracy that is an order of magnitude better. The advantage of the combined sensor is that fewer sensors need to be installed to achieve 3-axis attitude determination. At only  $25 \times 24 \times 10$  [mm], the size of the prototype is almost 2.6 times smaller than the Arcsec Twinkle, which is the smallest COTS star tracker currently available. While the latest Sun sensors for CubeSats are still 5 times smaller than the combined sensor, only 3 combined sensors are required on a satellite, compared to the reference combination 2 star trackers and 4 Sun sensors. Thus, it can be concluded that the combined sensor takes up half the volume compared to typical attitude sensor configurations, while offering stable pointing accuracy that lies between star trackers and Sun sensors. Still, it is unsure whether its power consumption is also low enough for CubeSats, as no dedicated microcontroller has been designed yet. The power consumption of the CMOS module narrowly exceeds the requirements already and a microcontroller will only add to the power consumption. A different CMOS module might need to be selected for future designs in order to lower the power consumption, or a central computing unit on a satellite should analyse the images. Test results in section 6.2.1.2 also showed that the computational load of the star tracker algorithm needs to be decreased severely, as the update rate of 1 [Hz] cannot be achieved. To conclude this section, the combined sensor offers performance between that of a star tracker and Sun sensor and can operate eclipse and sunlight, while taking up less volume on the spacecraft. But, future designs should focus on decreasing the power consumption and computational load.

## 7.2. Discussion of methodology

Most of the experiments were successfully performed. Generally, the experiments helped to quantify the performance of a 2-in-1 star tracker and Sun sensor compared to currently available COTS. While the tests were sufficient for this thesis, a number of improvements can be made for future experiments and research.

### 7.2.1. Star tracker tests

The star tracker test was performed at a local observatory just outside the city of Haarlem, The Netherlands. This is an area where light pollution is prominent. In addition, the presence of an atmosphere also decreased the quality of the test conditions. The test conditions also differed from day-to-day, making comparisons of data from one night to the other difficult. Despite these unideal testing conditions, the sensor was able to see the stars clearly enough for attitude determination. Still, further development of the sensor can benefit from better testing conditions that are closer to those in space. A new location should be found with less light pollution, less atmosphere and better weather.

Then, the star tracker functionality test only considered three analogue gain settings and no optimum has been found. It was believed that increasing the analogue gain beyond 12.0 would increase the noise levels substantially, making solving too difficult. This theory was never tested and the data shows that gains higher than 12.0 could make an impact on the success rate of the sensor at medium-long (0.3-0.4 [s]) exposure times. Subsequent tests should include larger analogue gains in order to find the optimum setting.

Moreover, the star tracker performance test estimated the accuracy of the sensor using 266 measurements. This gave an estimated margin of error of  $0.025^\circ$ , but this is half of predicted accuracy of the sensor. While it was unexpected that the star tracker would be as accurate as  $0.051^\circ$ , more tests should be performed in order to accurately estimate the sensor's accuracy. For example, a margin of error of  $0.005^\circ$  and 2-sigma confidence would require just under 5000 measurements. This number of measurements is advised when more time is available and when a flight-ready sensor is being developed.

### 7.2.2. Sun sensor tests

The light source that was used in the Sun sensor test does not fully represent the Sun in terms of intensity, size and spectrum. It proved to be difficult to find a suitable light source, as current technologies and COTS light sources do not have all three properties. Lasers have the right intensity and size, but only operate at one wavelength. A bright LED might have the right intensity and spectrum, but not the correct angular size. The limited time and budget of this thesis prevented the development of a specific light source that does represent the Sun truthfully. For future research, either a combination of individual tests using lasers and LEDs separately should be used, or another method that represents the Sun should be found.

During the Sun sensor performance test, it was difficult to accurately select the correct elevation angle. While the azimuth angles were selected using an accurate rotating stage, the elevation angle was configured using a set triangle. This reduced the accuracy in the test setup to  $0.5^\circ$  for elevation angles. This might have had a significant impact on the accuracy measurements and could have caused a small asymmetry in the results. This issue can be solved by obtaining specific experimental equipment with which the elevation angle can be set more accurately.

## 7.3. Unexplored areas

There are several areas of the design that have not been tested or addressed due to time constraints or lack of resources. These range from design decisions to specific experiments. Further research into the combined sensor should try to investigate these areas in order to better determine the feasibility of this design.

First, the noise reduction techniques used in the star tracker algorithm were simplistic. It consisted of dark frames averaged into a single frame and a bias frame to reduce hot pixels. These frames were combined and subtracted from the images taken by the sensor. While this reduced the noise levels to an extent where the algorithm was capable of extracting the coordinates from the images, a fair amount of noise was still visible. Inspection of the images saw numerous noise pixels being picked up as stars by the algorithm. The noise reduction also removed faint stars from the images, thereby reducing the number of stars useable for attitude determination. Better noise reduction techniques should be developed to further limit noise levels in the sensor's images, without removing faint stars.

Second, the Sun sensor has not been tested for albedo effects. Albedo tends to negatively affect the accuracy of Sun sensors significantly, as it can create a second Sun spot on the CMOS chip. As Sun sensors just output the position of the brightest pixel on their imaging surface, they are unaware of whether the spot originates from the Sun or from albedo. The impact of albedo on the combined sensor should be investigated and if required, mitigation strategies should be considered.

Third, the sensor has not been tested for the risk of burn-in when exposed to the Sun. The risk for burn-in was considered in the selection of the CMOS optical module by keeping the aperture as small as possible. However, due to the light source of the Sun sensor tests being not as intense as the Sun, burn-in could not be simulated. Future tests should retry this experiment to gain an understanding of the reliability of the sensor when in the hostile environment of space.

Next to the risks of albedo and burn-in, the effectiveness of the baffle to block stray light has not been tested. A test plan was created for this test, but a lack of time prevented the test from being carried out. Therefore, the impact of stray light on the performance of the sensor has not been measured yet.

Moreover, the Sun sensor showed decreasing accuracy for increasing incidence angles. Better testing equipment could show that this is a constant phenomenon based on the cosine of the incidence angle, as shown in previous Sun sensor designs in section 2.2. If this is indeed the case, then a correction could be applied to the Sun sensor algorithm in order to improve the accuracy near the edges of the sensor's FOV.

Finally, a thermal vacuum test was considered, but left out due to time constraints. As this is a COTS optical module, it is not designed for operation in the vacuum of space. The same holds for radiation effects. Observing what effect thermal vacuum has on the sensor can determine which areas of the physical design need to be changed. There also exists the possibility for a COTS optical module that has similar specifications and can handle thermal vacuum. However, in this thesis only modules compatible with Raspberry Pi and Arduino were considered, which limits the available options. Subsequent combined sensor designs can also use the same OV9281 CMOS chip, but design a new lens and hardware layout around it that is compatible with the environment of space.

# Conclusion

The aim of this thesis was to investigate how the performance and technical budgets of a combined star tracker and Sun sensor for small satellite form factors compares to a combination of individual star trackers and Sun sensors on a system level. Small satellites require a combination of several sensors to maintain 3-axis attitude determination, but with satellites becoming smaller and smaller, volume comes at a premium. Next to that, most attitude sensors can only operate in specific light and tumbling conditions. Therefore, making more versatile attitude sensors while maintaining performance is a critical development for the small satellite sector. The hypothesis was that a single COTS CMOS imaging module can function as both a star tracker and Sun sensor; compared with the currently employed combinations of sensors used in three-axis attitude determination, this new configuration could achieve similar target performance and smaller technical budgets on a system level.

Tests have shown that this combined sensor has an accuracy comparable to the smallest currently available COTS star trackers and to that of simple Sun sensors, while being more versatile in its placement and in its availability in different light conditions. Power consumption tests showed that the CMOS chip selected for the prototype design draws power close to the design requirements, but additional power will be required for solving the images and extracting the satellite's attitude. Should the sensor be redesigned, the option of manufacturing a dedicated low-power microcontroller for analysing the images should be considered. This controller would also help to improve the update rate of the sensor, especially in combination with a more refined star tracker algorithm. If this does not reduce the power consumption sufficiently, then the option of using a central computing unit on the satellite should be investigated. Similarly, the current size of the PCB of the prototype does not adhere to the design requirements, but a redesign might bring its size within limits. Therefore, it can be concluded that there is a possibility for creating a 2-in-1 star tracker and Sun sensor that has similar target performance and smaller technical budgets than typical combinations of attitude determination sensors, provided that dedicated hardware is designed.

Several improvements can be made to this thesis. Most notably, the accuracy of the star tracker should be determined using more tests with better lighting conditions. More performance can be extracted from the sensor by testing a wider variety of sensor settings and improving noise correction algorithms. For the Sun sensor tests, a better method of representing the Sun should be found and the accuracy of the test setup should be increased. Additional tests should be carried out that investigate the risk of burn-in when looking at the Sun and investigate the survivability of the sensor in the vacuum of space. The effect of stray light on the accuracy of the sensor should also be determined. In the future, developments in CMOS hardware might allow for the selection of a different CMOS chip that is better suited for a 2-in-1 star tracker and Sun sensor.

# References

- [1] NewSpace Systems. *NewSpace Systems - AQUILA-D02 Sun Sensor Datasheet*. URL: <https://satsearch.co/products/newspace-systems-nfss-411-fine-sun-sensor>.
- [2] Liang He et al. "Developments of attitude determination and control system of microsats: A survey". In: *Proceedings of the Institution of Mechanical Engineers, Part I: Journal of Systems and Control Engineering* 235.10 (Nov. 2021), pp. 1733–1750. ISSN: 0959-6518, 2041-3041. DOI: 10.1177/0959651819895173. URL: <http://journals.sagepub.com/doi/10.1177/0959651819895173> (visited on 04/22/2024).
- [3] *FlexCore: Low-Cost Attitude Determination and Control Enabling High-Performance Small Spacecraft*. URL: <https://digitalcommons.usu.edu/smallsat/2016/TS10AdvTech2/5/> (visited on 04/24/2024).
- [4] S. S. Arnold, R. Nuzzaci, and A. Gordon-Ross. "Energy budgeting for CubeSats with an integrated FPGA". In: *2012 IEEE Aerospace Conference*. 2012 IEEE Aerospace Conference. Big Sky, MT: IEEE, Mar. 2012, pp. 1–14. ISBN: 978-1-4577-0557-1 978-1-4577-0556-4 978-1-4577-0555-7. DOI: 10.1109/AERO.2012.6187240. URL: <http://ieeexplore.ieee.org/document/6187240/> (visited on 05/20/2024).
- [5] Kornél Kapás et al. "Attitude determination for nano-satellites – I. Spherical projections for large field of view infrasensors". In: *Experimental Astronomy* 51.2 (Apr. 2021), pp. 515–527. ISSN: 0922-6435, 1572-9508. DOI: 10.1007/s10686-021-09730-y. URL: <https://link.springer.com/10.1007/s10686-021-09730-y> (visited on 05/10/2024).
- [6] Josh O'Neill et al. "Development of a high-accuracy low-cost sun sensor for CubeSat application". In: *Aeronautics and Aerospace Open Access Journal* 4.3 (Sept. 29, 2020), pp. 142–146. ISSN: 25764500. DOI: 10.15406/aaobj.2020.04.00115. URL: <https://medcraveonline.com/AAOAJ/development-of-a-high-accuracy-low-cost-sun-sensor-for-cubesat-application.html> (visited on 04/23/2024).
- [7] Carl C. Liebe et al. "Three-axis sun sensor for attitude determination". In: *IEEE Aerospace and Electronic Systems Magazine* 31.6 (June 2016), pp. 6–11. ISSN: 0885-8985. DOI: 10.1109/MAES.2016.150024. URL: <http://ieeexplore.ieee.org/document/7501228/> (visited on 04/26/2024).
- [8] *Needronix Eagle Miniature CubeSat Sun Sensor*. URL: <https://needronix.eu/products/eagle#main-features> (visited on 04/26/2024).
- [9] Qi Zhang and Yulin Zhang. "Design and Verification of an Integrated Panoramic Sun Sensor atop a Small Spherical Satellite". In: *Sensors* 22.21 (Oct. 24, 2022), p. 8130. ISSN: 1424-8220. DOI: 10.3390/s22218130. URL: <https://www.mdpi.com/1424-8220/22/21/8130> (visited on 04/23/2024).
- [10] Angel Porras-Hermoso, Javier Cubas, and Santiago Pindado. "Use of spacecraft solar panels and Sun sensors for estimation of the Sun-pointing direction in the UPMSat-2 mission". In: *Measurement* 204 (Nov. 2022), p. 112061. ISSN: 02632241. DOI: 10.1016/j.measurement.2022.112061. URL: <https://linkinghub.elsevier.com/retrieve/pii/S026322412201257X> (visited on 04/23/2024).
- [11] Demet Cilden-Guler et al. "Attitude Estimation with Albedo Interference on Sun Sensor Measurements". In: *Journal of Spacecraft and Rockets* 58.1 (Jan. 2021), pp. 148–163. ISSN: 0022-4650, 1533-6794. DOI: 10.2514/1.A34814. URL: <https://arc.aiaa.org/doi/10.2514/1.A34814> (visited on 04/23/2024).
- [12] Andrea Antonello, Lorenzo Olivieri, and Alessandro Francesconi. "Development of a low-cost sun sensor for nanosatellites". In: *Acta Astronautica* 144 (Mar. 2018), pp. 429–436. ISSN: 00945765. DOI: 10.1016/j.actaastro.2018.01.003. URL: <https://linkinghub.elsevier.com/retrieve/pii/S0094576517301911> (visited on 04/26/2024).
- [13] NASA. *State-of-the-Art Small Spacecraft Technology*. Small Spacecraft Systems Virtual Institute, Feb. 2024, pp. 153–157. URL: <http://www.nasa.gov/smallsat-institute/sst-soa>.

- [14] Lizbeth Salgado-Conrado. "A review on sun position sensors used in solar applications". In: *Renewable and Sustainable Energy Reviews* 82 (Feb. 2018), pp. 2128–2146. ISSN: 13640321. DOI: 10.1016/j.rser.2017.08.040. URL: <https://linkinghub.elsevier.com/retrieve/pii/S1364032117311863> (visited on 05/13/2024).
- [15] Joost Romijn et al. "Microfabricated albedo insensitive sun position sensor system in silicon carbide with integrated 3D optics and CMOS electronics". In: *Sensors and Actuators A: Physical* 354 (May 2023), p. 114268. ISSN: 09244247. DOI: 10.1016/j.sna.2023.114268. URL: <https://linkinghub.elsevier.com/retrieve/pii/S0924424723001176> (visited on 05/01/2024).
- [16] Anatoly Pelemeshko et al. "High-precision CubeSat sun sensor coupled with infrared Earth horizon detector". In: *IOP Conference Series: Materials Science and Engineering* 734.1 (Jan. 1, 2020), p. 012012. ISSN: 1757-8981, 1757-899X. DOI: 10.1088/1757-899X/734/1/012012. URL: <https://iopscience.iop.org/article/10.1088/1757-899X/734/1/012012> (visited on 04/29/2024).
- [17] Ning Xie and Albert J. P. Theuwissen. "A Miniaturized Micro-Digital Sun Sensor by Means of Low-Power Low-Noise CMOS Imager". In: *IEEE Sensors Journal* 14.1 (Jan. 2014), pp. 96–103. ISSN: 1530-437X, 1558-1748. DOI: 10.1109/JSEN.2013.2280453. URL: <http://ieeexplore.ieee.org/document/6588567/> (visited on 05/14/2024).
- [18] Ruben Gomez-Merchan et al. "A Low-Latency, Low-Power CMOS Sun Sensor for Attitude Calculation Using Photovoltaic Regime and On-Chip Centroid Computation". In: *IEEE Transactions on Instrumentation and Measurement* 72 (2023), pp. 1–12. ISSN: 0018-9456, 1557-9662. DOI: 10.1109/TIM.2023.3268478. URL: <https://ieeexplore.ieee.org/document/10105288/> (visited on 05/14/2024).
- [19] Ron Noomen. "Flight and Orbital Mechanics, AE2-104, lecture hours 19+20: Eclipse, maneuvers". URL: [https://ocw.tudelft.nl/wp-content/uploads/AE2104-Orbital-Mechanics-Slides\\_10.pdf](https://ocw.tudelft.nl/wp-content/uploads/AE2104-Orbital-Mechanics-Slides_10.pdf) (visited on 05/06/2024).
- [20] János Takátsy et al. "Attitude determination for nano-satellites – II. Dead reckoning with a multiplicative extended Kalman filter". In: *Experimental Astronomy* 53.1 (Feb. 2022), pp. 209–223. ISSN: 0922-6435, 1572-9508. DOI: 10.1007/s10686-021-09818-5. URL: <https://link.springer.com/10.1007/s10686-021-09818-5> (visited on 05/10/2024).
- [21] *CubeSpace products*. URL: <https://satsearch.co/products/cubespace-gen2-cubesense-sun> (visited on 04/24/2024).
- [22] Jie Jiang et al. "Rapid Star Tracking Algorithm for Star Sensor". In: *IEEE Aerospace and Electronic Systems Magazine* 24.9 (Sept. 2009), pp. 23–33. ISSN: 0885-8985. DOI: 10.1109/MAES.2009.5282286. URL: <http://ieeexplore.ieee.org/document/5282286/> (visited on 04/25/2024).
- [23] Xinyuan Liu et al. "A Compressed and High-Accuracy Star Tracker with On-Orbit Deployable Baffle for Remote Sensing CubeSats". In: *Remote Sensing* 13.13 (June 26, 2021), p. 2503. ISSN: 2072-4292. DOI: 10.3390/rs13132503. URL: <https://www.mdpi.com/2072-4292/13/13/2503> (visited on 04/24/2024).
- [24] Mehdi Nasiri Sarvi et al. "Design and implementation of a star-tracker for LEO satellite". In: *Optik* 208 (Apr. 2020), p. 164343. ISSN: 00304026. DOI: 10.1016/j.ijleo.2020.164343. URL: <https://linkinghub.elsevier.com/retrieve/pii/S0030402620301777> (visited on 05/16/2024).
- [25] Liheng Ma et al. "Attitude-correlated frames approach for a star sensor to improve attitude accuracy under highly dynamic conditions". In: *Applied Optics* 54.25 (Sept. 1, 2015), p. 7559. ISSN: 0003-6935, 1539-4522. DOI: 10.1364/AO.54.007559. URL: <https://opg.optica.org/abstract.cfm?URI=ao-54-25-7559> (visited on 05/20/2024).
- [26] Fernando De Almeida Martins, Valdemir Carrara, and Roberto D'Amore. "Positionless Attitude Estimation With Integrated Star and Horizon Sensors". In: *IEEE Access* 12 (2024), pp. 2340–2348. ISSN: 2169-3536. DOI: 10.1109/ACCESS.2023.3348077. URL: <https://ieeexplore.ieee.org/document/10375389/> (visited on 04/24/2024).
- [27] Tam Nguyen, Kerri Cahoy, and Anne Marinan. "Attitude Determination for Small Satellites with Infrared Earth Horizon Sensors". In: *Journal of Spacecraft and Rockets* 55.6 (Nov. 2018), pp. 1466–1475. ISSN: 0022-4650, 1533-6794. DOI: 10.2514/1.A34010. URL: <https://arc.aiaa.org/doi/10.2514/1.A34010> (visited on 04/24/2024).

- [28] Stefano Carletta, Paolo Teofilatto, and M. Farissi. "A Magnetometer-Only Attitude Determination Strategy for Small Satellites: Design of the Algorithm and Hardware-in-the-Loop Testing". In: *Aerospace* 7.1 (Jan. 5, 2020), p. 3. ISSN: 2226-4310. DOI: 10.3390/aerospace7010003. URL: <https://www.mdpi.com/2226-4310/7/1/3> (visited on 04/22/2024).
- [29] Alvarez et al. "Design and On-Orbit Performance of the Attitude Determination and Passive Control System for the Quetzal-1 CubeSat". In: *Journal of Small Satellites* 12.2 (May 31, 2023), pp. 1231–1247. URL: <https://jossonline.com/current-issue-joss-vol-12-no-02-may-2023/> (visited on 04/25/2024).
- [30] Khaled Gaber, Mohamed B. El Mashade, and Ghada A. Abdel Aziz. "A Hardware Implementation of Flexible Attitude Determination and Control System for Two-Axis-Stabilized CubeSat". In: *Journal of Electrical Engineering & Technology* 15.2 (Mar. 2020), pp. 869–882. ISSN: 1975-0102, 2093-7423. DOI: 10.1007/s42835-020-00352-6. URL: <http://link.springer.com/10.1007/s42835-020-00352-6> (visited on 04/25/2024).
- [31] Sung-Hoon Mok et al. "Performance Comparison of Gyro-Based and Gyroless Attitude Estimation for CubeSats". In: *International Journal of Control, Automation and Systems* 18.5 (May 2020), pp. 1150–1160. ISSN: 1598-6446, 2005-4092. DOI: 10.1007/s12555-018-0878-z. URL: <http://link.springer.com/10.1007/s12555-018-0878-z> (visited on 04/25/2024).
- [32] Alicia Johnstone. *CubeSat Design Specification Rev. 14.1*. Feb. 2022. URL: [https://static1.squarespace.com/static/5418c831e4b0fa4ecac1bacd/t/62193b7fc9e72e0053f00910/1645820809779/CDS+REV14\\_1+2022-02-09.pdf](https://static1.squarespace.com/static/5418c831e4b0fa4ecac1bacd/t/62193b7fc9e72e0053f00910/1645820809779/CDS+REV14_1+2022-02-09.pdf) (visited on 06/14/2024).
- [33] Teledyne FLIR. *Key differences between CCD and CMOS imaging sensors*. Sept. 4, 2021. URL: <https://www.flir.eu/support-center/iis/machine-vision/knowledge-base/key-differences-between-ccd-and-cmos-imaging-sensors/> (visited on 07/01/2024).
- [34] OmniVision. *OV9281 Preliminary Specification Datasheet*. 2019.
- [35] National Solar Observatory Sacramento Peak. *Magnitude*. 2001. URL: <https://web.archive.org/web/20080206074842/http://www.nso.edu/PR/answerbook/magnitude.html> (visited on 07/22/2024).
- [36] Dustin Lang et al. "ASTROMETRY.NET: BLIND ASTROMETRIC CALIBRATION OF ARBITRARY ASTRONOMICAL IMAGES". In: *The Astronomical Journal* 139.5 (May 1, 2010), pp. 1782–1800. ISSN: 0004-6256, 1538-3881. DOI: 10.1088/0004-6256/139/5/1782. URL: <https://iopscience.iop.org/article/10.1088/0004-6256/139/5/1782> (visited on 08/14/2024).

# A

## Gantt chart

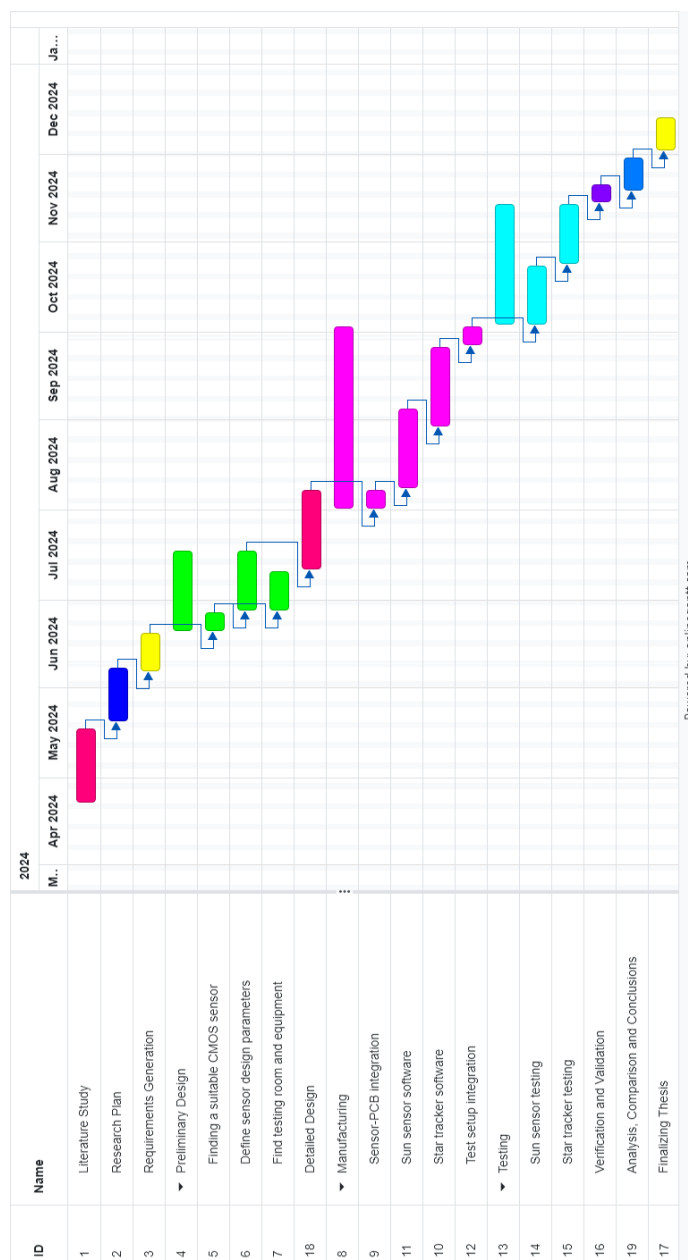


Figure A.1: Gantt chart of the planning of the thesis.

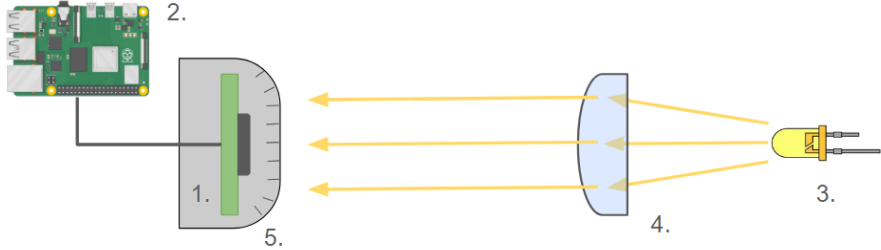
B

## Test plans

*Test plans are shown on the next pages.*

<i>Star Tracker Functionality Test Plan</i>	
<b>Test Description</b>	
	A functional test will be performed on the star tracker mode of the combined versatile attitude sensor in order to verify that the sensor is able to find the right ascension and declination of an image of the stars. The sensor will take images of the night sky, tries to identify the star patterns and outputs the region in space where these stars originate from. If the sensor is properly configured, it should find the coordinates within a second.
<b>Testing Goals</b>	
Primary Goals	- Verify that the sensor module is able to find the right ascension and declination of a star image
Secondary Goals	- Verify that the sensor module algorithm is sufficiently fast
<b>Testing Equipment</b>	
Sensor module	The sensor module that images the stars
Raspberry Pi	A computer unit that controls the sensor module and performs analysis on the images
Laptop	A laptop that powers the Raspberry Pi and keeps track of testing data
Flat table	A flat table to position the sensor on, so that it points up towards the sky
Dark environment	The sensor should have an unobstructed view to the night sky on a clear night. For this experiment, a local observatory was used where light pollution is limited
<b>Test Setup</b>	
Layout	
1. Sensor module 2. Raspberry Pi 3. Laptop 4. Night sky	<p>The diagram illustrates the experimental setup. On the left, a laptop (labeled 3) is connected via a cable to a Raspberry Pi (labeled 2). The Raspberry Pi is further connected to a sensor module (labeled 1) which is placed on a flat surface (table). The sensor module is tilted upwards at an angle of 89.5 degrees. The sensor's field of view is shown as a dashed cone pointing towards the night sky (labeled 4), which contains a constellation of stars.</p>
	The sensor is placed flat on the table, pointing towards the night sky The Raspberry Pi controls the sensor and analyses the images taken The experiment should be carried out on a clear night, with no clouds in sight.
<b>Testing Steps</b>	
	<ol style="list-style-type: none"> <li>1 Configure the test setup</li> <li>2 Take dark frame for noise reduction</li> <li>3 Take an image of the night sky</li> <li>4 Let the sensor process the image</li> <li>5 Store the estimated coordinates of the image</li> <li>6 Continue to the next image</li> <li>7 Repeat steps 3-6 until 50 images have been taken and analysed</li> <li>8 Repeat the test for different sensor configurations</li> </ol>
<b>Testing Criteria</b>	
	The test has been successfully performed when:
	1 The sensor was able to resolve 40 out of 50 star images successfully
	2 The sensor was able to operate at a speed of at least 1 Hz

<i>Star Tracker Performance Test Plan</i>	
<b>Test Description</b>	<p>The star tracker mode of the combined versatile attitude sensor will be tested for accuracy and power consumption. The sensor will take pictures of a clear night sky and will analyse them. The sensor identifies the star patterns and outputs the right ascension and declination coordinates where these stars originate from. This is compared to the known location of the stars, from which the accuracy of the star tracker can be derived.</p> <p>During the test, the voltage and current over the sensor is measured. This way, the power consumption of the sensor can be monitored.</p>
<b>Testing Goals</b>	
Primary Goals	- Determine accuracy of star tracker mode
Secondary Goals	- Determine power consumption of sensor module
<b>Testing Equipment</b>	
Sensor module	The sensor module that images the stars
Raspberry Pi	A computer unit that controls the sensor module and performs analysis on the images
Laptop	A laptop that powers the Raspberry Pi and is used to keep track of testing data
Leveling bed	A flat table whose height can be adjusted in all corners so that the surface is flat
Dark environment	The sensor should have an unobstructed view to the night sky on a clear night. For this experiment, a local observatory was used where light pollution is limited
Oscilloscope / Multimeter	An accurate measurement device used to monitor the voltage and current of the sensor, from which the power consumption can be calculated
<b>Test Setup</b>	
Layout	<p>1. Sensor module 2. Raspberry Pi 3. Laptop 4. Night sky 5. Leveling bed 6. Oscilloscope / Multimeter</p>
	<p>The sensor will be placed on a flat surface directly pointing towards zenith. Positioning the sensor to zenith needs to be done with high precision as installation errors propagate to the sensors final error. For example, an accurate spirit level can be used.</p> <p>At each measurement, the current time will be logged, as from this the right ascension and declination coordinates of zenith can be determined and compared to the measurements of the sensor itself.</p> <p>After each measurement, there should be a pause of at minimum 4 minutes in order to create distinctively different night sky images.</p> <p>Multimeters or oscilloscopes will be positioned on the power supply line of the sensor so that the power consumption can be measured.</p>
<b>Testing Steps</b>	
	<ol style="list-style-type: none"> <li>1 Configure the test setup</li> <li>2 Perform a calibration observation to ensure the test is setup up correctly</li> <li>3 Take a picture of the night sky</li> <li>4 Note down the current time of day</li> <li>5 Let the sensor process the image</li> <li>6 Note down the power consumption of the sensor</li> <li>7 Note down or store the estimated position of the image</li> <li>8 Repeat steps 3-7 until 10 measurements have been taken</li> <li>9 Wait at least 4 minutes before continuing with the experiment</li> <li>10 Repeat steps 3-9 until a total of 30 sets of 10 measurements have been taken</li> <li>11 Compare the coordinate estimations of the sensor with the actual coordinates of zenith at the time of measurement</li> </ol>
<b>Testing Criteria</b>	
	The test has been successfully performed when:
	1 The sensor was able to identify the elevation and azimuth of the star image with an 1-sigma accuracy better than 2.0 degrees
	2 The sensor's power consumption did not exceed 70 mW

<i>Sun Sensor Functionality Test Plan</i>	
<b>Test Description</b>	A functional test will be performed on the Sun sensor mode of the combined versatile attitude sensor in order to verify that the sensor is able to determine the angle of the Sun vector. The sensor module will be placed in front of a light source that simulates light from the Sun. A lens helps to collimate the light to the sensor, so that some of the light intensity is preserved. The sensor analyses the position of the Sun spot on its active pixel sensor, from which the angle of the Sun vector can be determined.
<b>Testing Goals</b>	
Primary Goals	- Verify that the sensor module is able to determine the direction of the Sun vector
Secondary Goals	- Verify that the sensor module algorithm is sufficiently fast
<b>Testing Equipment</b>	
Sensor module	The sensor module that images the Sun
Raspberry Pi	A computer unit that controls the sensor module and performs analysis on the images
Dark room	A darkened room to mimic a low-light environment
Light source	A lamp that creates light that represents the Sun
Lens	A lens that collimates the light from the light source
Rotating table	A table that can rotate into different angles so that the entire FOV of the sensor module can be tested
<b>Test Setup</b>	
Layout	 <p>1. Sensor module 2. Raspberry Pi 3. Lamp / Light source 4. Lens 5. Rotating table</p>
	<p>The sensor module will be placed onto a rotating table in front of a light source with collimated light. With the rotating table the sensor can be positioned in different angles so that the sensor's entire FOV can be tested.</p> <p>The light source projects its light onto the imaging surface of the sensor, from which it then calculates the angle of the Sun vector. The light source should have an angular diameter of 0.5 degrees relative to the sensor, which is comparable to that of the Sun on Earth. Furthermore, the light should have an intensity of or close to 1361 W/m<sup>2</sup> when it reaches the sensor, as this is the solar irradiance at 1 AU from the Sun.</p> <p>Getting such a light source has been proven to be difficult. Therefore, a combination of a lens and LED was used that does reach the correct light intensity, but has a larger angular diameter.</p> <p>The dark room might require the use of dark padding on its walls in order to absorb light reflected from the test setup. Else, this light might be picked up by the Sun sensor, which would lower the accuracy of the sensor</p>
<b>Testing Steps</b>	
	<ol style="list-style-type: none"> <li>1 Configure the test setup</li> <li>2 Perform a calibration observation to ensure the test is setup up correctly</li> <li>3 Position the sensor in the desired angle</li> <li>4 Let the sensor calculate the Sun vector in 10 images</li> <li>5 Note down or store the calculated Sun vectors</li> <li>6 Repeat steps 3-5 until 5 measurement sets have been taken with 5 different Sun angles</li> <li>7 Compare the calculated Sun vectors with the actual Sun vector</li> </ol>
<b>Testing Criteria</b>	
	The test has been successfully performed when:
	1 The sensor was able to identify a Sun angle in 40 out of 50 measurements
	2 The sensor was able to operate at a speed of at least 5 Hz

<i>Sun Sensor Performance Test Plan</i>	
<b>Test Description</b>	<p>The Sun sensor mode of the combined versatile attitude sensor will be tested for performance. In this test plan, a test is described that determines the accuracy and power consumption of the sensor. The sensor module will be placed in front of a light source that simulates light from the Sun, and the module can be placed in different angles to achieve testing coverage of its entire FOV. The sensor analyses the position of the Sun spot on its active pixel sensor, from which the angle of the Sun vector can be determined.</p> <p>During the test, the voltage and current over the sensor is measured. This way, the power consumption of the sensor can be monitored.</p>
<b>Testing Goals</b>	
Primary Goals	- Determine the accuracy of the Sun sensor mode
Secondary Goals	- Determine the power consumption of the sensor module in the Sun sensor mode
<b>Testing Equipment</b>	
Sensor module	The sensor module that images the Sun
Raspberry Pi	A computer unit that controls the sensor module and performs analysis on the images
Dark room	A darkened room to mimic a low-light environment
Light source	A lamp that creates light that represents the Sun
Lens	A lens that collimates the light from the light source
Rotating table	A table that can rotate into different angles so that the entire FOV of the sensor module can be tested
Oscilloscope / Multimeter	An accurate measurement device used to monitor the voltage and current of the sensor, from which the power consumption can be calculated
<b>Test Setup</b>	
Layout	
	<p>The sensor module will be placed onto a rotating table in front of a light source with collimated light. With the rotating table the sensor can be positioned in different angles so that the sensor's entire FOV can be tested.</p> <p>The light source projects its light onto the imaging surface of the sensor, from which it then calculates the angle of the Sun vector. The light source should have an angular diameter of 0.5 degrees relative to the sensor, which is comparable to that of the Sun on Earth. Furthermore, the light should have an intensity of or close to 1361 W/m<sup>2</sup> when it reaches the sensor, as this is the solar irradiance at 1 AU from the Sun.</p> <p>Getting such a light source has been proven to be difficult. Therefore, a combination of a lens and LED was used that has the correct angular diameter, but has a lower intensity than the target.</p> <p>The dark room might require the use of dark padding on its walls in order to absorb light reflected from the test setup. Else, this light might be picked up by the Sun sensor, which would lower the accuracy of the test.</p> <p>Multimeters or oscilloscopes will be positioned on the power supply line of the sensor so that the power consumption can be measured.</p>
<b>Testing Steps</b>	
	<ol style="list-style-type: none"> <li>1 Configure the test setup</li> <li>2 Perform a calibration observation to ensure the test is setup up correctly</li> <li>3 Position the sensor in the desired angle</li> <li>4 Let the sensor calculate the Sun vector</li> <li>5 Note down the power consumption of the sensor</li> <li>6 Note down or store the calculated Sun vector</li> <li>7 Repeat steps 3-6 until 77 measurement sets have been taken spread across the sensor's FOV</li> <li>8 Compare the calculated Sun vectors with the actual Sun vector</li> </ol>
<b>Testing Criteria</b>	
	The test has been successfully performed when:
	<ol style="list-style-type: none"> <li>1 The sensor was able to identify the Sun vector with an 1-sigma accuracy better than 5.0 degrees</li> <li>2 The sensor's power consumption did not exceed 70 mW</li> </ol>

<i>Baffle Effectiveness Test Plan</i>	
<b>Test Description</b>	The star tracker mode of the combined versatile attitude sensor will be tested on the effectiveness of the baffle in reducing stray light entering the sensor. The sensor module will be placed in an environment where light cannot easily scatter off objects and cause objects in view of the sensor to light up. An area outside with a clear view to the sky is preferred. A lamp is positioned 180 degrees from the sensor and shines parallel light onto the sensor. The lamp is then incrementally rotated into the FOV of the sensor, which will cause stray light to appear on the sensor's images. The test is performed with and without baffle so that the effectiveness of the baffle can be determined.
<b>Testing Goals</b>	
Primary Goals	- Determine the effectiveness of the extended baffle
Secondary Goals	-
<b>Testing Equipment</b>	
Sensor module	The sensor module that images the stars
Baffle	A baffle that should reduce stray light from entering the sensor
Raspberry Pi	A computer unit that controls the sensor module and performs analysis on the images
Laptop	A laptop that powers the Raspberry Pi
Scatter-free environment	The test should be performed in a place where light cannot scatter off the ground or sensor and cause additional stray light
Lamp	A lamp to mimic the effect of stray-light
<b>Test Setup</b>	
Layout  1. Sensor module 2. Raspberry Pi 3. Laptop 4. Lamp 5. Objects in image	
	<p>The sensor takes an image of the objects in view. The overall light levels of the image are calculated and compared with those from varying stray light angles.</p> <p>A lamp will shine parallel light onto the sensor, initially from an angle of 180 degrees.</p> <p>Higher light levels will indicate more stray light</p> <p>The global light level in the testing environment should be kept the same</p>
<b>Testing Steps</b>	<ol style="list-style-type: none"> <li>1 Configure the test setup. Position the baffle onto the sensor</li> <li>2 Perform a calibration observation to ensure the test is setup up correctly</li> <li>3 Position the lamp at 90 degrees to the side of the sensor</li> <li>4 Take an image and record the light level</li> <li>5 Position the lamp 5 degrees closer to the center of the sensor's FOV</li> <li>6 Repeat steps 4-5 until 30 degrees is reached</li> <li>7 Repeat steps 1-6 without the baffle</li> <li>8 Compare the pictures taken with and without baffle</li> </ol>
<b>Testing Criteria</b>	
	The test has been successfully performed when:
1	The sensor has been tested with stray light angles inside and outside its FOV

# C

## Sensor Code

The code that controls the Combined Versatile Attitude Sensor is fully written in Python. It can be accessed through a private GitHub repository, of which the link can be found below. A QR code has also been generated for easy access. All files can be found on the *master* branch. *StarTracker.py* and *SunSensor.py* contain the logic and code for controlling the sensor during tests. Please note that in order to successfully run the star tracker code, the Astrometry.net algorithm needs to be installed on a Linux machine. The algorithm can be downloaded through <https://astrometry.net/downloads/>.

**Link to GitHub:** [https://github.com/StijnHandgraaf/CVAS\\_software](https://github.com/StijnHandgraaf/CVAS_software)



Figure C.1: QR-code to GitHub repository.